

**CONTACT FORCE ANALYSIS UNDER FEMORAL HEAD MICRO-  
SEPARATION FOR CERAMIC-ON-CERAMIC HIP  
IMPLANTS: FINITE ELEMENT ANALYSIS AND  
EXPERIMENTAL VALIDATION**

by  
Deepika Kakarla

A thesis submitted to the faculty of  
The University of Utah  
in partial fulfillment of the requirements for the degree of

Master of Science

Department of Mechanical Engineering

The University of Utah

December 2011

Copyright © Lakshmi Navya Deepika Kakarla 2011

All Rights Reserved



## **ABSTRACT**

When a prosthetic hip fails to perform like an ideal ball-and-socket joint but instead permits small subluxation and edge loading between the joint members, the bearing surfaces are subjected to increased contact stresses and wear that could ultimately cause failure and require costly and painful revision of the prosthesis. The objectives of the present study were (1) to model and analyze one such adverse motion: rapid femoral head reduction; (2) to quantify the ensuing dynamic contact force and elevated contact stresses; and (3) to improve the relevance of hip joint wear tests by providing validated contact force values representing worst case conditions in ceramic-on-ceramic hip bearings. A dynamic model of head micro-separation occurring during normal human gait was examined via a combined approach of laboratory testing and finite element analysis (FEA). The testing validated the FEA (though with some explainable error) against measured values for normal velocity at a point on the femoral head and strain on the femur and femoral neck. Then, the FE model was used to analyze the contact forces and the stresses during the edge loading. This approach contradicted a key hypothesis of the study, specifically, that the duration of edge loading contact would be close to the period of vibrations in the femur. It was revealed that the peak contact stresses in this study are strongly influenced by the model's input conditions rather than the femur's natural vibration characteristics.

A synthetic femur implanted with a prosthetic femoral stem and a ceramic-on-ceramic hip bearing couple were the components of the model. The model was tested dynamically in the laboratory with three values of micro-separation, including severe edge loading conditions. Strain gages installed on the femur and the femoral neck recorded strains, and a laser Doppler vibrometer measured the velocity of the femoral head during reduction. The FE model used explicit time integration and a locally refined global mesh at the contact region. A submodel of the region in the vicinity of contact was refined and displacement BCs were inferred from the global model, which provided an economical higher-fidelity analysis of the contact stresses.

The results showed an increase in the peak femoral head velocity and the peak femoral strains during the reduction event as the micro-separation increased. In the validation of the FEA against experimentally measured values, large errors in velocity and relatively small errors in strain were observed. The submodel analysis showed much higher contact force and contact stress than the global model analysis, which was attributed to the boundary conditions (BCs) and the limitations of the software used. A better understanding of the cause of the errors in the approach undertaken demands an improvement in the submodeling procedure, which involves a more detailed analysis beyond the scope of this study. Also, the contradiction of the key hypothesis led to a need for more in-vivo data that would help further to accurately quantify the contact mechanics of COC hip joints.

Overall, this research provides much-needed physical foundations for setting contact forces for analysis of wear damage in in-vitro ceramic-on-ceramic hip implant wear studies.

## TABLE OF CONTENTS

ABSTRACT .....	III
LIST OF FIGURES .....	VIII
LIST OF TABLES .....	XIV
ACKNOWLEDGEMENT .....	XV
CHAPTER 1 .....	1
INTRODUCTION .....	1
1.1 Total Hip Arthroplasty .....	1
1.2 Implant Materials .....	1
1.3 Background .....	3
1.3.1 COC Implants – Squeaking – Stripe Wear .....	3
1.3.2 Micro-separation / Micro-lateralization .....	5
1.3.3 Contact Force between Implants .....	8
1.4 Motivation .....	9
1.5 Objectives .....	12
1.6 Specific and Novel Contributions .....	13
CHAPTER 2 .....	15
BIOMECHANICAL REDUCTION MODEL .....	15
2.1 Introduction .....	15
2.2 Components of the BMR Model .....	16
2.3 BMR Model Configuration .....	18
2.3.1 Standard Orientations .....	20
2.3.2 Feasible Setup Orientations .....	21

2.3.3 Final Configuration .....	21
2.4 Initial Conditions .....	22
2.5 Inputs and Boundary Conditions .....	23
2.6 Rigid Body Analysis of BMR Model .....	26
2.6.1 Equations of Motion .....	26
2.6.2 Effect of the Spring Force on the Contact Force .....	29
 CHAPTER 3 .....	 32
 ELEMENTARY ANALYSIS AND TESTING .....	 32
3.1 Introduction.....	32
3.2 Problem Statement .....	33
3.3 Methods.....	34
3.3.1 Laboratory testing .....	34
3.3.2 Axisymmetric Finite Element Modeling .....	38
3.3.3 3D Finite Element Analysis .....	39
3.4 Results: Comparison of Analytical, Experimental and Axisymmetric FEA .....	39
3.5 Conclusion .....	42
 CHAPTER 4 .....	 43
 LABORATORY TESTING OF BMR MODEL .....	 43
4.1 Introduction.....	43
4.2 The Femur Construct .....	43
4.3 Fixtures and Initial Alignment .....	45
4.4 Spring mechanism.....	49
4.5 Laser Vibrometer .....	51
4.6 Strain Gaging .....	53
4.7 Data Acquisition .....	53
4.8 Experimental Procedures .....	54
4.8.1 Input velocity .....	54
4.8.2 Reduction trials .....	55
 CHAPTER 5 .....	 58
 FINITE ELEMENT ANALYSIS OF BMR MODEL .....	 58
5.1 Introduction.....	58
5.2 Three Dimensional Solid Model and Mesh Generation .....	59
5.3 Material Properties .....	64
5.4 Loading and Boundary Conditions .....	67
5.5 Contact Modeling.....	69

5.6 Submodeling of BMR Model.....	69
5.6.1 Submodel Generation.....	70
5.6.2 Boundary Conditions .....	71
5.6.3 Submodeling Analysis Procedure .....	73
 CHAPTER 6 .....	 75
 RESULTS: TESTING AND ANALYSIS OF BMR MODEL.....	 75
6.1 Experimental Results .....	75
6.1.1 Velocity of the Femoral Head .....	75
6.1.2 Strain in the Femur and the Femoral Neck .....	76
6.2 Validation of the BMR Model .....	79
6.2.1 Velocity of the Femoral Head .....	79
6.2.2 Strain in the Femur and the Femoral Neck .....	81
6.3 Inferred Outputs from Global Model and Submodel Analyses .....	84
6.4 Contour Plots .....	88
 CHAPTER 7 .....	 93
 DISCUSSION.....	 93
7.1 Validation of the PSG in the FE Model .....	93
7.2 Behavior of the Femoral Cortex Material .....	94
7.3 Effect of Friction.....	95
7.3.1 Effect of Lubrication on the PSG.....	95
7.3.2 Effect of Friction on the Velocity of the Femoral Head .....	96
7.3.3 Effect of Friction on the Contact Force .....	97
7.4 Key Hypothesis .....	99
7.5 Submodeling Procedure – Future Scope .....	100
7.5.1 Contact Stiffness – Boundary Conditions .....	101
7.5.2 Successive Submodeling Approach to Improve Consistency and Convergence.....	102
 CHAPTER 8 .....	 105
 CONCLUSIONS AND FUTURE SCOPE.....	 105
8.1 Conclusions .....	105
8.2 Future Scope .....	106
REFERENCES .....	108

## LIST OF FIGURES

Figure 1: Schematic of THA [5] .....	2
Figure 2: Stripe wear (made visible by rubbing with graphite) on femoral head and acetabular liner from a retrieved COC hip [24] .....	5
Figure 3: a) Radiographic image of an in-vivo hip with a superimposed CAD model in the position of the bearing couple; b) Schematic showing micro-separation of 4.3 mm [27].....	6
Figure 4: Illustration of the BMR model .....	19
Figure 5: ISO 14242-1 standard – followed to orient the BMR model [1].....	20
Figure 6: Macro view of the BMR Model .....	22
Figure 8: The Polar Separation Gap (PSG).....	23
Figure 9: A/P axis of rotation in BMR model.....	24
Figure 10: Lateral force application to achieve a forced contact between the femoral head and the acetabular liner .....	25
Figure 11: The pelvic sub-assembly showing its components – acetabular liner, acetabular shell, and model pelvis (rigid polyurethane test block).....	26
Figure 12: Free body diagram of the BMR model (liner partly shown).....	28
Figure 13: Contact force vs. Spring force according to the rigid-body analysis; for reference, the data point on the plot shows the contact force for the spring force value used in the BMR test.....	31

Figure 14: Schematic of the impacted rods.....	33
Figure 15: Schematic of the two rod impact test .....	34
Figure 16: Rod 1 (shorter) and Rod 2 (longer) used in the impact test; a US quarter is shown for reference to set scale .....	35
Figure 17: Fixtures to hold Rod 1(top) and Rod 2 (bottom).....	37
Figure 18: a) Laser focused at the midpoint of Rod 2; b) Strain gage installed at the midpoint of Rod 2; second strain gage installed on the opposite side of the first one.....	38
Figure 19: Contact patch area on the round surface of Rod 1 during the impact, recorded .....	40
Figure 20: Axisymmetric fine mesh results of speed measured at the midpoint of Rod 2 overlaid with analytical and experimental data.....	41
Figure 21: Axisymmetric fine mesh results of strain measured at the midpoint of Rod 2 overlaid with analytical and experimental data.....	41
Figure 22: Experimental setup of the BMR model.....	47
Figure 23: Proximal end of the femur construct; assembly of synthetic femur and implants – femoral stem and femoral head; the femur’s greater trochanter was resected to provide a line of sight for the laser velocity measurement described in Section 4.5 .....	48
Figure 24: Distal end of the femur construct with a press-fit dowel pin between the condyles .....	48
Figure 25: a) Compression spring system connected to the femur by means of a b) hook .....	50

Figure 26: Components of the spring system (spring in green, load cell and rotation block) and laser focus point (red spot) from the vibrometer focused on the femoral head to measure the velocity .....	52
Figure 27: Strain gages installed on a) the femur and b) the femoral neck .....	52
Figure 28: Arrangement of gage blocks to measure the horizontal displacement of the femoral head.....	56
Figure 29: Mesh of the femur (left) and zoomed-in view (right) showing the tetrahedral mesh density.....	62
Figure 30: Mesh of the femoral stem (left) and zoomed-in view (right) showing the tetrahedral mesh density.....	62
Figure 31: Femoral stem and cancellous bone assembly (left) showing the penetration of the stem mesh into the cancellous mesh; (right) Section view of assembly of femoral stem, cancellous and cortical bones showing the inner core mesh density .....	63
Figure 32: Locally refined hexahedral meshes of a) femoral head, b) acetabular liner; c) Zoomed in views of the local refinement; d) Tetrahedral mesh of the acetabular shell and the test block .....	63
Figure 33: a) Section view of femoral head and acetabular liner meshes and the PSG; b) Detail view showing a locally refined mesh at the contact.....	64
Figure 34: Two strain gages installed on the femur’s medial diaphysis. One strain gage measured longitudinal strain and the other measured lateral strain .....	65

Figure 35: Longitudinal (Parallel) strain and Lateral (Transverse) strain vs. force using the original and the adjusted material properties; the strains obtained using adjusted material properties match with the experimentally obtained strains. .... 66

Figure 36: Illustration of the loading and the BCs in the FE version of the BMR model (shown in section view) ..... 68

Figure 37: a) Meshes of the submodel components, refined at the contact region; b) The BMR submodel; c) Illustration of the submodel generation along with its dimensional details. “Cut” labels indicate where the submodel’s geometry was partitioned from the global model’s geometry (Dimensions are in mm.)..... 72

Figure 38: a) Velocity response of the femoral head during the 2 mm PSG reduction event;..... 76

Figure 39: Measured strain response for 2 mm PSG in a) the femur, b) the femoral neck over a total span of 0.1s; Overlay of the strain response for the three PSGs in c) the femur and d) the femoral neck over a span of 12ms ..... 78

Figure 40: Comparison of velocity of the femoral head during the reduction event for 2 mm PSG using FEA and experiment a) for the total time span for which experimental data was collected and, b) focused view for 12 ms..... 81

Figure 41: Comparison of strain for 2 mm PSG from FEA and experiment in a) the femur, b) the femoral neck, both for the total time span for which the experimental data was recorded; focused views of the strain comparison for 12 ms for c) the femur and, d) the femoral neck..... 83

Figure 42: Comparison of the global model and the submodel contact force .....	85
Figure 43: Comparison of the global model and the submodel results of contact pressure for a) the femoral head and, b) the acetabular liner .....	86
Figure 44: Comparison of the global model and the submodel results of contact area for a) the femoral head and, b) the acetabular liner .....	87
Figure 45: Contact stress distribution during the reduction event at 6.9 ms for the liner (top) and, the head (bottom) from the global model analysis .....	89
Figure 46: Contact stress distribution during the reduction event at 6.9 ms for the liner (top) and, the head (bottom) from the submodel analysis .....	90
Figure 47: Stress distribution in the femoral sub-assembly (section view) at the time of maximum stress at the contact; displacements shown at 20 X magnitude .....	91
Figure 48: Contour plots of minimum principal strain on a point (where a strain gage was installed to measure the longitudinal strain) on the femur (top) and on the femoral stem (bottom).....	92
Figure 49: Time record of velocity of the femoral head for different CoF ( $\mu$ ).....	97
Figure 50: Contact force vs. Coefficient of Friction from rigid body analysis; the plot shows an infinite contact force for a particular friction value – this is when the femoral head does not reduce into the acetabular liner .....	98
Figure 51: Proposed first submodel partitioned at the femoral neck (from the femoral sub-assembly) and the acetabular liner (from the pelvic sub-assembly) .....	103
Figure 52: Femur – implants (femoral stem and head) assembly .....	113

Figure 53: Setup of the femur construct on the CMM, showing the datum planes ..... 115

Figure 54: Image of the femur's distal end showing the datum coordinate axes and the origin; Z-axis points perpendicular and outward to the granite base plate ..... 115

Figure 55: Image demonstrating the projection of a cylinder axis onto the XY plane ... 116

Figure 56: Image showing the small flat on the side of the femoral neck ..... 117

## LIST OF TABLES

Table 1: Available prosthetic hip material couples and their corresponding acronyms .....	2
Table 2: Description of the symbols used in the FBD of the BMR model .....	29
Table 3: Dimensional details of the rods .....	33
Table 4: Material properties of the rods .....	33
Table 5: Contact radius and area from the axisymmetric fine model in comparison to the analytical and experimental results .....	40
Table 6: RMS errors of speed and strain of the axisymmetric FE model (error analysis performed against the analytical solution) .....	42
Table 7: Material properties of the components of the BMR model .....	45

## **LIST OF ABBREVIATIONS**

A/P – Anterior/Posterior

BMR – Bio-Mechanical Reduction

CAD – Computer Aided Design

COC – Ceramic-on-Ceramic

FEA – Finite Element Analysis

ISO – International Organization for Standardization

M/L – Medial-Lateral

MOM – Metal-on-Metal

MOP – Metal-on-Polyethylene

NIH – National Instituted of Health

PSG – Polar Separation Gap

THA – Total Hip Replacement

## **ACKNOWLEDGEMENT**

First, I would like to thank my advisor, Dr. Rebecca Brannon for her guidance throughout this project. Her persevering support both as my advisor and as a fellow woman has boosted my confidence. I would like to thank Dr. Dan Adams and Dr. Ken Monson for being a part of my supervisory committee and for their valuable suggestions. I would like to specially thank my mentor Tony Sanders for letting me be a part of the ‘hip’ team and for his immense support and guidance throughout the life of the project. I would like to thank NIH for being the financial backbone for this research. I would like to thank Exponent, Inc. employees for their efforts in computational analysis.

I would like to thank my colleague Ira Tibbitts for his help whenever I needed it and, for investigating the calibration error and re-calibrating the drop tower apparatus. I would like to express my gratitude towards Jeff Kessler for allowing us to use the machines in the Structural Integrity Laboratory at the University of Utah, and to the Ortho Development Corporation and the machinists for their experienced and high precision machining and for making this project relatively economical. I also would like to thank my close friends and roommates for their moral support.

This section would be incomplete without mentioning the most important persons in my life – my parents and family members who confided in me and brought me up to this stage; Thank you Mom and Dad. Above all of us, I would like to thank the God Almighty for giving me the strength and courage to face all the challenges.

## **CHAPTER 1**

### **INTRODUCTION**

#### **1.1 Total Hip Arthroplasty**

Total hip arthroplasty (THA) is a surgical treatment that alleviates pain and disability by replacing a damaged, arthritic hip joint with a prosthetic ball-and-socket joint. The specific anatomical features that are surgically replaced are the femoral head and the acetabulum. A femoral stem implant is placed into a broached intramedullary canal in the femur's proximal metaphysis. A femoral head (the joint's ball member) is then assembled with the femoral stem implant. The acetabulum is replaced by a socket, typically assembled from two separate, nested hemispherical cups. The outer metal cup, termed the "shell," supports the inner cup, termed the "liner," which articulates with the head. The liner and the femoral head form the new bearing surfaces of the prosthetic hip joint as shown in Figure 1.

#### **1.2 Implant Materials**

Hip implant bearings are typically made of plastics, metals, or ceramics paired together in various combinations. The plastic material is usually a modified form of ultra-high molecular weight polyethylene (UHMWPE), enhanced by radiation cross-linking (XLPE) to improve wear resistance. Metal bearings are made of cobalt-chromium (Co-Cr) alloy, which is hard, wear resistant, and biocompatible in bulk form. The most widely used ceramic materials in hip bearings are aluminum oxide (alumina) and zirconia-

toughened-alumina (ZTA), and (less commonly) zirconium oxide (zirconia). The ceramics are the hardest and the most wear-resistant of the standard implant bearing materials [2-4]. The various hip implant bearing couples are categorized based on specific combinations of all these materials; generally, the categories consist of Hard-Polyethylene (PE) and Hard-Hard couples, as shown in Table 1.

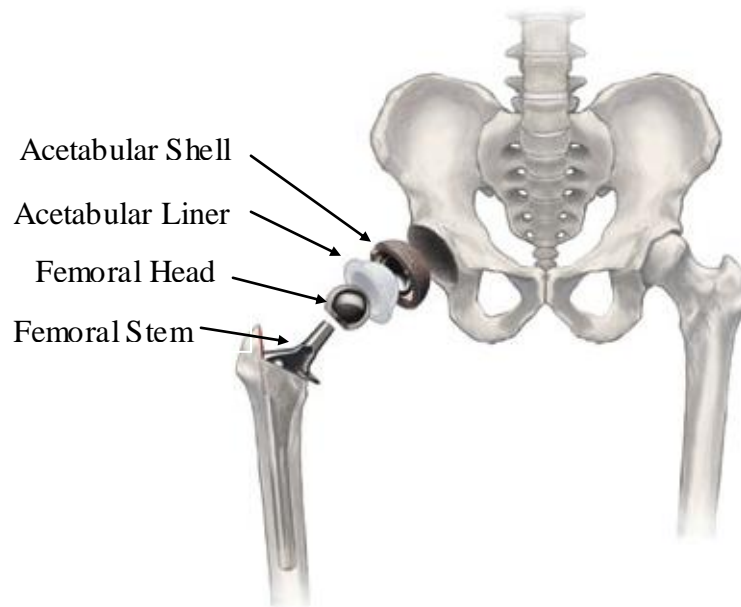


**Figure 1:** Schematic of THA [5]<sup>1</sup>

**Table 1:** Available prosthetic hip material couples and their corresponding acronyms

Head Material	Liner Material		
	Polyethylene	Metal	Ceramic
Metal	Metal-on-Polyethylene (MOP)	Metal-on-Metal (MOM)	-
Ceramic	Ceramic-on-Polyethylene (COP)	Ceramic-on-Metal (COM)	Ceramic-on-Ceramic (COC)

<sup>1</sup> "Hip New World" by Alan S. Brown, reprinted with permission, Engineering magazine, Vol. 128, No. 10, Copyright ASME 2006.

## 1.3 Background

### 1.3.1 COC Implants – Squeaking – Stripe Wear

The ceramic materials used in hip prosthesis bearings offer properties giving them superior performance in some ways, yet they also have drawbacks that have prevented COC couples from becoming the preferred hip bearing option. Their principal advantage is their extreme hardness. Alumina bearings, for example, have a hardness exceeding 1800 GPa [6] which compares to 500 GPa or less for CoCr [7], the hardest metal hip bearings. Their high hardness is one property making COC couples the lowest-wearing category of hip bearing. In hip simulator wear tests, COC bearings wore at a rate of  $<0.01 \text{ mm}^3/\text{Mcycles}$ , MOM bearings at a rate of  $0.1 \text{ mm}^3/\text{Mcycles}$ , and MOP bearings at a rate of  $13 \text{ mm}^3/\text{Mcycles}$  [8]. The drawback of high hardness is brittleness, and there have been numerous reports of COC hips exhibiting sudden catastrophic fracture [4, 9-11]. To combat such failures, ceramic implant manufacturers have improved the material's density and implemented overload proof testing of every unit [12]. Consequently, fracture failure rates have diminished to less than 0.01% according to one recent report [13]. Another as yet unresolved, shortcoming of COC hips is that they may become noisy after several months of in-vivo service; this problem is the subject of intense contemporary research.

There have been numerous recent clinical reports of various noises such as squeaking, clicking, or grating emanating from COC hips [14]. Among these noises, squeaking appears to be the most common and the chief source of patient complaints [14-16]. In a recent review of squeaking in COC hips, 10.7% out of 131 patients reported audible squeak during daily activities [17]. Another recent clinical report has shown that 10.6%

of the COC hips generated noise, out of which 2.6% were defined as squeaking [18]. Although squeaking has not been linked to painful or debilitating symptoms, the annoying noise leads to some affected patients to undergo a revision surgery in which, either or both of the bearings are replaced [17, 18].

According to Ranawat et al., squeaking is due to a combination of subluxation (a small-scale separation of the head from the liner, not great enough to result in complete dislocation), edge loading (contact between the head and the rim of the liner, in contrast with typical loading where the head contacts the liner's spherical inner surface), and subsequent stripe wear (a particular wear pattern of COC hips, further described below) [19]. According to Yang et al., the etiology of the squeaking problem is multifactorial, involving causes such as femoral head subluxation, femoral neck impingement on the acetabular liner, and secondary stripe wear [20]. Further research on the cause of squeaking shows that it could be a consequence of stripe wear [21] or else of particular design features of the implant system [14, 22]. Recently, metal transfer (caused by subluxation during which the femoral head slides onto the edge of a metallic shell), together with a disruption of fluid film lubrication, was reported as the sole repeatable cause of squeaking in a laboratory hip joint simulator [23]. However, ongoing (yet unpublished) research at the University of Utah shows that subluxation and squeaking are not limited to metal components, but can also occur in COC bearing couples.

Stripe wear is the term used to describe a particular distribution of wear seen on some retrieved COC bearing couples. Figure 2 illustrates a typical example of stripe wear on a femoral head; numerous clinical reports show that this type of wear, though typically shaped as thin and elongated, can manifest in a variety of shapes, sizes, and orientations

[21, 24, 25]. Some investigators have reported that stripe wear occurs due to edge loading between the COC bearing surfaces [25]. Theories describing the cause of stripe wear are further discussed in Section 1.3.2.

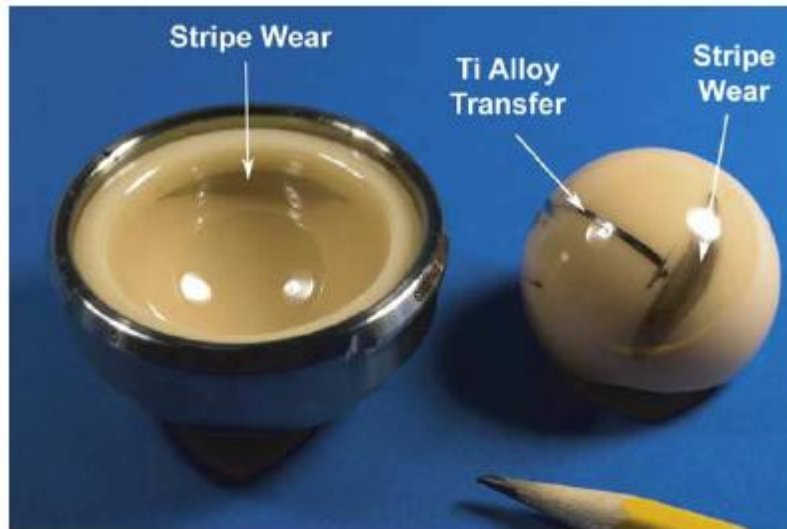


**Figure 2:** Stripe wear (made visible by rubbing with graphite) on femoral head and acetabular liner from a retrieved COC hip [24]

### 1.3.2 Micro-separation / Micro-lateralization

The typical human gait cycle may be subtly altered by THA in a way that could lead to the problems of COC stripe wear and squeaking. A walking gait cycle consists of two alternating phases for each leg: (1) stance phase, during which the leg supports the body via foot-ground contact, and (2) swing phase, during which the leg is swung forward to bear the next footfall. Researchers have imaged artificial hip joints in-vivo using fluoroscopic video examination of patients (

Figure 3) performing a variety of common activities including walking [26-28]. They have detected that, in many activities, the prosthetic femoral head may temporarily sublux from the acetabular liner by a small distance, on the scale of fractions of a

millimeter to a few millimeters. The occurrence of such separation during the swing phase of gait is explained as an effect of soft-tissue laxity and changes to the dimensions of the hip joint – both secondary to hip replacement surgery – as well as the non-load-bearing state of the leg during swing phase. Upon heel strike at the beginning of stance phase, the subluxed head is forcibly relocated into the prosthetic cup; this motion is termed as “reduction” of the femoral head.

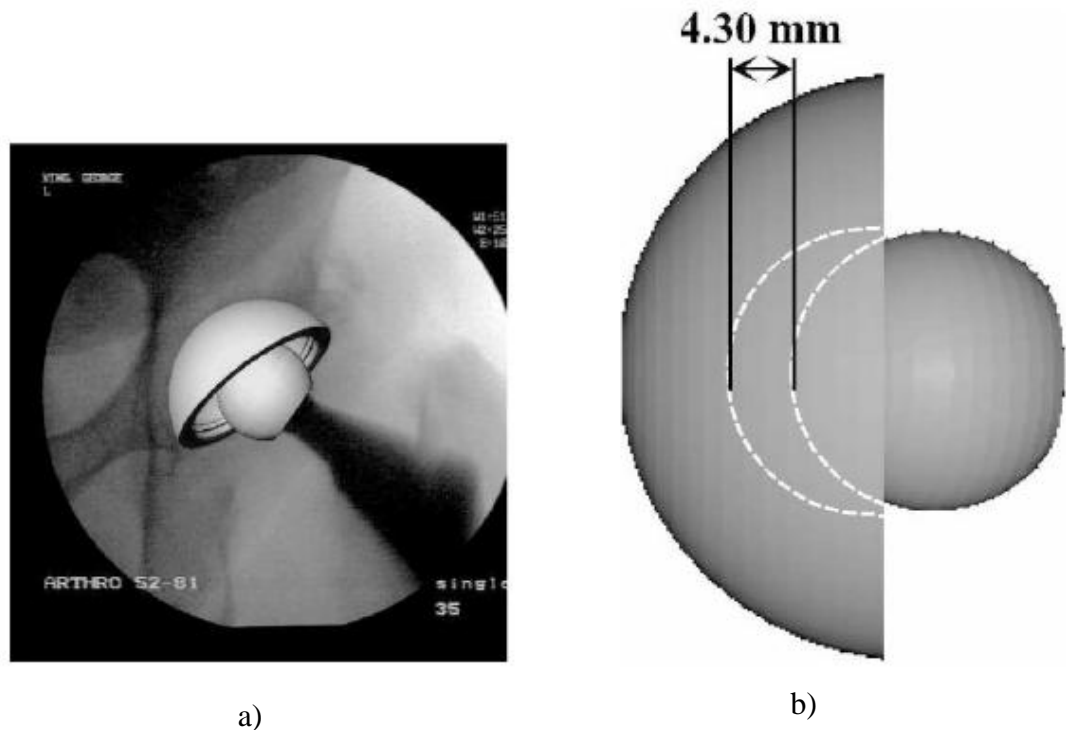


**Figure 3:** a) Radiographic image of an in-vivo hip with a superimposed CAD model in the position of the bearing couple; b) Schematic showing micro-separation of 4.3 mm [27]

Separate research work has incorporated this understanding of prosthetic hip kinematics in laboratory test methods, with the outcome of eliciting more clinically relevant wear patterns on tested hip implants. Traditionally, hip simulator studies used only fully reduced, concentric head-liner articulations, and the resulting bearing wear patterns did not match with in-vivo wear patterns [29]. In a novel experiment, Nevelos et al. implemented a design change to a hip joint simulator, inserting a spring to

impart a medial-lateral spring force that caused supero-lateral subluxation of the femoral head relative to the acetabular liner during the low-load, swing phase of simulated gait [30]. Though the details of how and where the spring force had been applied are not reported in this article, we have adapted a similar mechanism of using a lateral spring force in our study to cause subluxation of the femoral head. The researchers termed the new motion “micro-separation”, and by adding it to the hip simulator motion pattern, they succeeded in replicating clinically relevant in-vitro COC stripe wear [30]. Wear scars generated in-vitro via the addition of micro-separation motion have also been correlated with increases in gravimetrically measured wear [30-32]. Micro-separation is not limited to COC bearings; it is also a concern in hard-PE bearing couples [33].

There are multiple potential causes for the edge loading that leads to stripe wear in-vivo. One explanation is the swing-phase micro-separation is followed by forced edge loading contact between the bearing surfaces upon heel strike [21, 32]. Another explanation is that femoral neck impingement with the rim of the acetabular liner can cause bearing couple separation and edge loading [31]. Although the research in this thesis focuses on edge loading at the beginning of heel strike, it should be noted that edge loading can also occur during other activities, such as standing up from a chair [25].

The term micro-separation was originally described and illustrated as an actual separation of the bearing surfaces [34]. Recently, authors from the same research center have published a more precise term “micro-lateralization,” by which they mean to emphasize that the femoral head maintains contact with the edge of the acetabular liner throughout subluxation and edge loading [35]. Though numerous hip simulator studies have included micro-separation and achieved clinically relevant stripe wear, scientific

understanding of the contact mechanics of prosthetic hip joints undergoing edge loading is still in a preliminary stage and, therefore, is a focus of this research effort.

### **1.3.3 Contact Force between Implants**

Reducing hip implant wear and averting problems such as squeaking require improved understanding of hip joint mechanics, including kinematics, kinetics, and contact mechanics. Edge loading is a forced contact between the ball and head that is not anticipated or safely accommodated by the bearing's design, and it occurs during daily activities such as normal human gait, sitting, stair climbing, walking, etc. [26]. Previous studies show that edge loading occurs with or without subluxation [36]. Edge loading can also occur as a result of steep cup angles associated with malpositioning and instability of the acetabular components [37]. We have used a steep cup angle ( $60^\circ$ ) in our study to represent a worst-case scenario of the cup angle that could cause edge loading. Average hip contact forces, correlated in time with gait patterns of daily activities, were examined in a few patients with prosthetic implants [38]. The average hip contact forces reported in this paper come from a study of a few patients and, hence, there is a possibility that the average could vary drastically if more number of patients were studied. Contact mechanics between COC implants were studied under adverse conditions [34, 39]. In [34], only ideal conditions where the femoral head contacts within the acetabular liner were considered making it a static analysis. In [39], the contact stress distribution between COC bearing surfaces was analyzed using the finite element method, but that study failed to include a physical dynamic event (like the human gait cycle). The contact force between the bearing surfaces was coupled with micro-separation in causing implant wear in several hip simulator studies. A lower swing-phase load coupled with severe

micro-separation yields a higher wear rate when compared to the wear rate caused by a higher swing-phase load with mild micro-separation [32]. However, a contact force between the bearing surfaces has not been quantified in all of the hip simulator studies involving the micro-separation and edge loading modes. Contact stress distributions were studied under static edge loading conditions and different micro-separation values using finite element analysis [34]. The degree of these contact stresses is highly dependent on various parameters such as the value of micro-separation, radial clearance between the bearing members, inclination angle of the acetabular cup, and thickness of the ceramic liner.

Scrutiny of several of these studies reveals that there is presently a gap in scientific understanding about the mechanics of hip prosthesis edge loading, namely that there is little knowledge about the contact forces that accompany edge loading. Researchers who have implemented edge loading in hip simulator tests have done so by imposing a pre-selected micro-separation distance [30, 40]. Only recently has there appeared a published report that analytically determined contact forces in such tests [35]. Weak understanding of edge loading mechanics, both in-vivo and in-vitro, impairs resolution of current problems such as COC hip squeaking. This shortcoming is rectified by the work in this thesis, which gives particular attention to forces associated with micro-separation.

#### **1.4 Motivation**

The observed wear patterns on COC implants are important in two senses. First, they probably cause squeaking and hence the need for revision surgery, which is an acute problem. Moreover, these problems discourage widespread use of bearing materials that would otherwise benefit many patients by being longer lasting and more wear resistant.

To overcome such problems, there is a need for better understanding of the severe, adverse load conditions, such as edge loading, that apparently cause the most severe, clinically observed wear. At present, there is little understanding of the forces that arise between the implants during the severe loading events, and that limits our ability to test designs and materials under worst-case conditions. Though a few research labs have implemented micro-separation conditions in hip simulators, such test methods are not yet widely adopted; for example, the ISO standard for hip simulator wear testing includes no description of or requirement for micro-separation conditions [1]. This lack of transfer from research to widespread practice may be due in part to a lack of understanding or acceptance of the micro-separation conditions, such as the separation distance or separation frequency, that those modified wear simulators impose. The publications about those simulators and their routines do not provide crucial design details, nor do they quantify the forcing functions [30, 35]; more fundamentally, the conditions imposed during these tests have not been demonstrated to be representative of in-vivo hip joint mechanics. Thus, there is a need for better understanding of the basic mechanics and mechanisms involved in severe-condition hip testing, as well as the mechanics of adverse hip joint motions.

The research literature shows that subluxation and consequent edge loading may occur under a wide variety of activities [26]. Each such activity could have its own conditions, and any individual patient could exacerbate those conditions via details such as bodyweight and, frequency of various activities. Yet, no design testing program can consider all possible scenarios, so it is vital that the testing which becomes standardized

be representative of frequent events, such as the subluxation and reduction that happen during routine walking.

One key missing element in our understanding of edge loading associated with micro-separation during walking is the contact force between the bearing surfaces. There is only one known report of an analysis that determines such a contact force, and that comes from a simulation of a test machine, not of a human body activity [35]. Having more information about the contact force during edge loading could result in more relevant test methods, and perhaps more widespread acceptance and use of those methods. Furthermore, it could open doors to innovative, physiologically relevant testing protocols that could accelerate progress in material and design development.

To address the aforementioned gaps in COC implant wear data, we study a commonly occurring event that causes edge loading, to determine the contact force and the contact stress that arise during that event. We design a simple model to represent edge loading in conjunction with swing-phase subluxation and heel-strike reduction. In this model, a femoral head is initially subluxed and contacting the edge of the acetabular cup, as though at the end of swing phase just prior to heel strike. To emulate the conditions of the gap geometry reported from in-vivo fluoroscopy [26], a small initial lateral force is applied to keep the head in contact with the edge of the cup. The head is suddenly relocated into the liner by an axially directed reduction motion, as would occur during the heel-strike event of the gait cycle. This biomechanical model of edge loading was examined using a combination of computational and experimental methods as further described throughout this thesis.

### 1.5 Objectives

- The main objective of this project is to quantify the ensuing contact force between the bearing surfaces of COC hip implants. Further, the resulting contact stress distribution is analyzed.
- Since the contact force cannot be directly measured from a physical laboratory version of the model, it is instead indirectly inferred using a finite-element based version that is validated against data that can be measured. Accordingly, a supporting project objective is to thoroughly validate the finite element model in a laboratory test equipped with sensitive dynamic diagnostics.
- A further objective is to develop computationally cost effective techniques to accurately resolve contact stresses in the vicinity of relatively minute edge-loading contact patches. To this end, the FEA in this thesis employs an aggressive approach to submodeling the region directly surrounding the contact area between the head and the liner.
- A preliminary objective was to acclimate the project's team of engineers to the computational and laboratory techniques for the biomechanical model study. Hence, this thesis also reports an opening project to measure and analyze contact stresses and vibratory responses during the low speed impact of slender rods.

Our hypothesis is that the contact force during the sudden reduction is strongly affected by the dynamics of stress wave propagation in the femur during the period of contact. This hypothesis is supported by observations of transverse and oblique impact of long, slender rods. Studies of such impact have shown that the peak contact forces are

noticeably influenced by stress waves when the duration of contact is similar to the vibration period of the induced bending stress waves [41, 42]. We hypothesize that similar phenomena occur in a femur when a sudden, impulsive load is applied to its proximal end via a COC contact couple. This hypothesis comes in part because the femur is compliant in comparison to the implants, a property that favors relatively long vibration periods. It also comes from the fact that the COC contact couple is very stiff, a property which ensures that the contact displacements will be small and hence the contact duration will be very short.

Since there are currently no methods for direct measurements of contact forces, finite element analysis is the primary means of investigating the validity of the key hypothesis. A simplistic means of estimating the contact forces would be to use a rigid body dynamics approach coupled with Hertzian contact theory. However, to account for dynamic stress waves, a more sophisticated approach is needed; so, a finite element model is analyzed using an explicit solution approach. A rigid body analysis is nevertheless developed to provide a comparison of the simplest relevant mechanical analysis with the results of the more sophisticated FEA approach.

## **1.6 Specific and Novel Contributions**

This thesis contributes to the body of knowledge in the fields of orthopedic implant design and testing, hip joint biomechanics, and COC hip bearing couples. The specific and novel contributions of this thesis include the following:

- An engineering model of a common reduction event by which hip joint prostheses experience edge loading that may be a root cause of the currently observed

problems of stripe wear and ceramic hip squeaking; specifically, the estimation of worst-case contact forces between the bearing surfaces.

- Demonstration of the role played by dynamic stress wave propagation caused by impulsive loading events that affect COC hips and the skeletal members to which they are attached. It was revealed that the stress wave at the contact did not have a predominant effect on the contact force duration, as it was generated by an insufficiently rapid input given to the model.
- A novel and aggressive approach to submodeling in finite element analysis of the stresses arising around very small contact areas during loading of hard-on-hard hip bearings. This approach, which has been demonstrated to be effective in other application areas [43], has not yet been widely practiced in the orthopedic research field. This work illustrated its merits by setting a new standard for the refinement that is both required and readily achievable for contact mechanics analysis in hard-on-hard orthopedic implants. Further improvement of the submodeling strategy is required to better quantify the contact mechanics in such problems involving contact.
- These results will help to better define the mechanical conditions by which hip joint wear studies can mimic worst-case (though common) in-vivo loading, which in turn is anticipated to contribute to improving the longevity of COC hip implants.

## **CHAPTER 2**

### **BIOMECHANICAL REDUCTION (BMR) MODEL**

#### **2.1 Introduction**

This research has developed and used a simple model of a prosthetic hip joint and the immediately connected skeleton to study the mechanics of an edge loading event. The event was an impulsive reduction of a subluxed femoral head from an initial contact position on the edge of an acetabular liner. In its initial configuration, the model simulated conditions existing at the end of the swing phase of gait, just prior to heel strike. The reduction phase of the calculation predicts motion and forces occurring as an immediate reaction to heel strike. A key reason for choosing to model this particular edge-loading scenario is that it is the same scenario represented in micro-separation hip simulator wear tests developed at several different research centers [32, 40]. In research tests at those centers, the edge loading and reduction motions have been implemented for the purpose of studying implant wear under severe but realistic conditions in long term, repetitive motion tribological tests. In contrast, the present study has developed a model of impulsive reduction for the purpose of studying the instantaneous mechanics of the event, i.e. the effects occurring within several milliseconds. The engineering model used to represent this event is herein referred to as the Bio-Mechanical Reduction (BMR) model. This chapter describes and illustrates the BMR model in its abstract sense as a simplified representation of a complete physical entity, the simplification comprising

only those elements that substantially influence the complete entity's response to a specified mechanical stimulus. Later chapters describe methods to implement the model in both experimental and computational contexts.

## **2.2 Components of the BMR Model**

The BMR model is an abstract representation of a human pelvis and a femur that undergo the sudden reduction event. The model consists of two sub-assemblies – a femoral sub-assembly and a pelvic sub-assembly. The femoral sub-assembly consists of a synthetic left femur implanted with a press-fit femoral stem and a femoral head. The pelvic sub-assembly consists of a rigid polyurethane foam test block to represent the pelvis; the block is prepared with a hemispherical hole representing the acetabulum, and the hole is implanted with a press-fit acetabular shell and a corresponding acetabular liner. Further details describing the actual implants employed in this model are given in the chapters describing the experiments. The following sections in this chapter describe the model's inputs and constraints.

Though the muscles and tendons in the human body play the role of keeping the skeleton intact and generating voluntary skeletal movements, an underlying assumption of the BMR model is that the forces and constraints imposed by the soft tissues may be neglected in comparison to the forces between hard components (bone and implant materials) for the purposes of the event under study. There are three key points that support this simplification in the model.

- The reduction event occurs as a reaction to foot-to-ground contact (heel strike); this force gets transferred in a very short span of time from the heel to the hip joint via the tibia, the knee joint and the femur. In that short span, the reaction

- forces acting to change the subluxation state at the hip joint are the forces traveling through the skeletal members and not the forces of voluntary muscle contractions. The BMR model models the skeleton-propagating reaction force and neglects the soft tissue reactions.
- The event under study lasts for a few milliseconds. It is hypothesized that during this short span of time, the contact force will be affected by a few reflected stress waves in the surrounding components. The stress waves in the stiffer components (skeletal members), which travel at higher velocity than those in the soft tissues, will have a dominating effect on the contact force. Moreover, stress wave attenuation caused by viscous dissipation in the soft tissues can be neglected because the duration of the event is considerably smaller than the characteristic response time of the material. In other words, the Deborah number (i.e., the ratio of the material's relaxation time to the event stimulus time) is large thus, justifying an approximation that the soft tissues respond elastically.
  - In an ideal THA, the muscles and ligaments around the hip joint help to keep the femoral head (ball) and the acetabular liner (socket) in a fully reduced articulation. However, some THA surgeries may result in a relatively loose joint due to muscle and ligament weakness or laxity, allowing subluxation of the head from the liner. When the subluxation occurs, the muscles take up the laxity by exerting force on the hip joint (similar to the force exerted by muscles surrounding a normal hip) and cause a contact between the head and the liner's edge. During the heel-strike phase, the contact force generated between the femoral head and the liner's edge rises so high that it cannot be attributed to the

small magnitude voluntary contractions of the muscles surrounding the hip joint [44]; therefore the BMR model does not implement separate actuators for such muscle forces.

### 2.3 BMR Model Configuration

The BMR model, as shown in **Error! Reference source not found.**, was configured to mimic certain conditions specified within an international standard for hip simulator wear tests, ISO 14242-1 [1]. Specifically, that standard describes a cycle of synchronized motions and loads at the hip joint that emulates the kinetics of the hip during normal walking gait. The characteristics of that cycle that were adopted into the BMR model were the relative orientations of the femoral stem and acetabular liner at the beginning of the gait cycle as shown in Figure 5. A macro view of the configuration of the BMR model, with the femoral head fully reduced in the liner, is given in **Error! Reference source not found.** This configuration was achieved by applying a specific sequence of rotations to the pelvic and the femoral sub-assemblies relative to the reference coordinate frame and neutral orientations described by the standard. That sequence is described in brief below and in detail in Appendix A. Furthermore, the 3D BMR model was designed to permit only 2D planar (X-Y) rigid-body motions, with the motion plane being a coronal anatomic plane through the center of the fully reduced head-liner couple. Out-of-plane motions were neglected for simplicity. Section 2.5 provides rationale for these aspects of the model design.

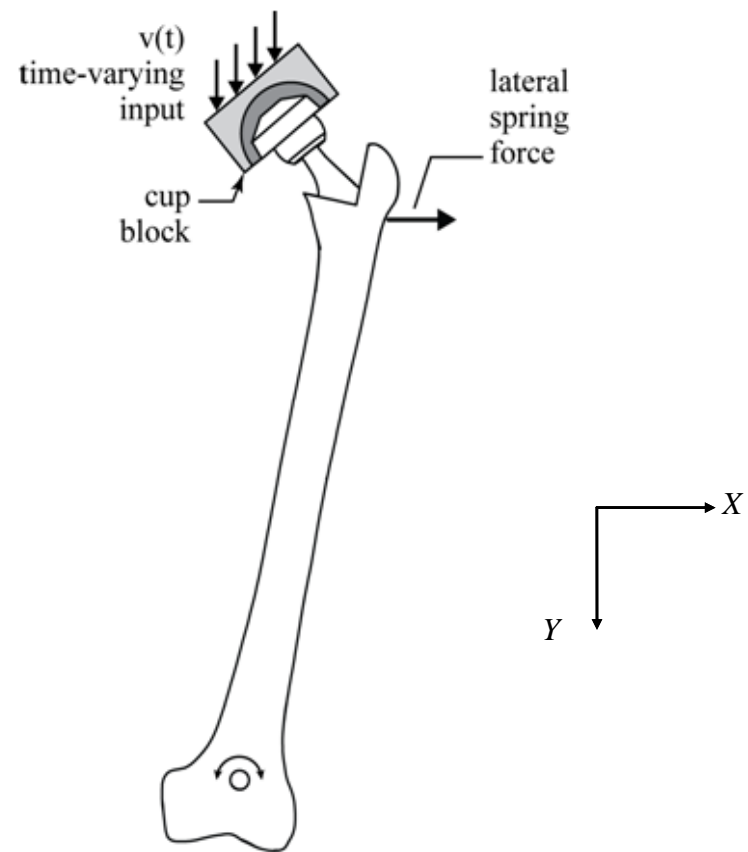


**Figure 4:** Illustration of the BMR model

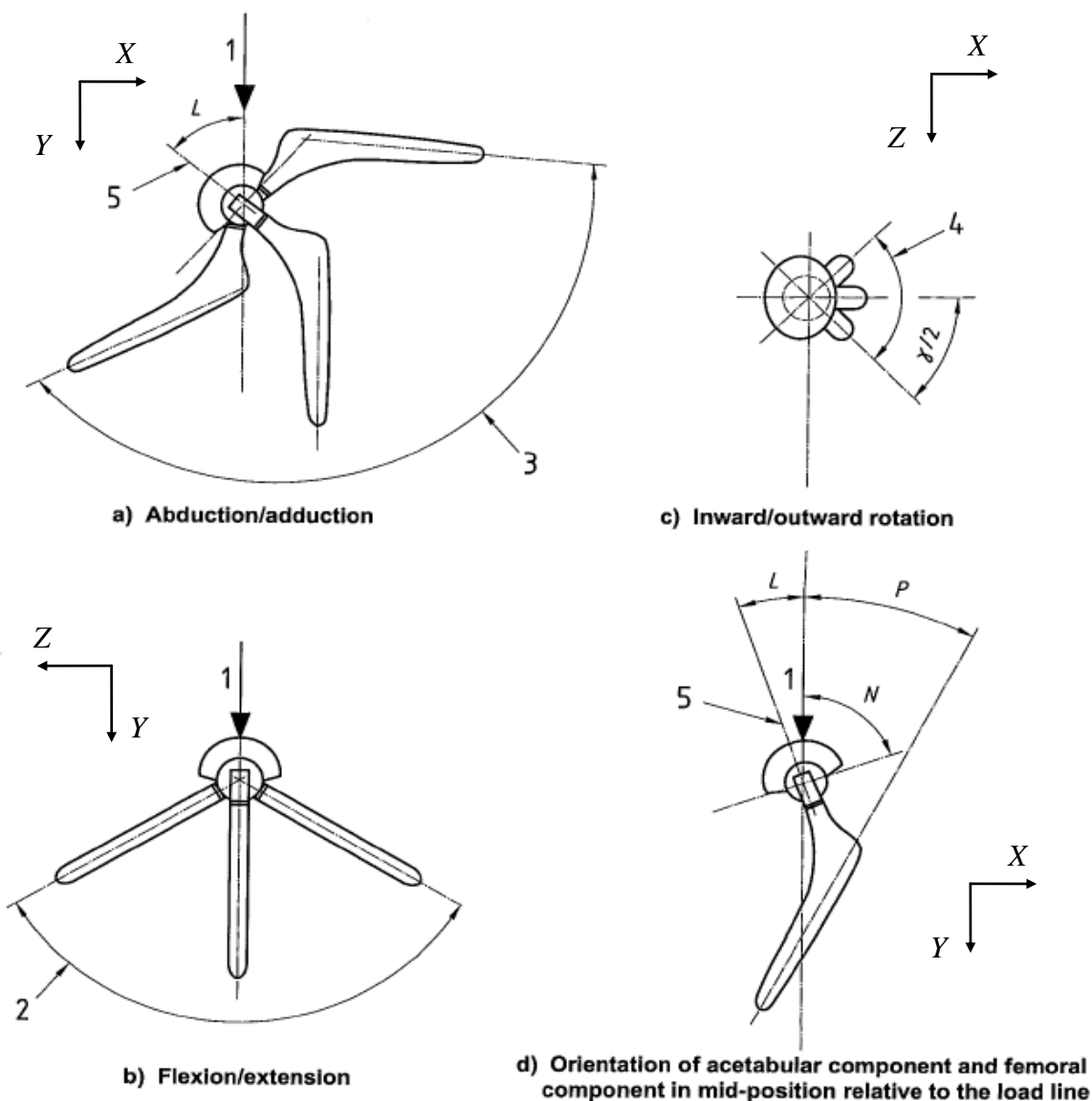


**Figure 5:** ISO 14242-1 standard – followed to orient the BMR model [1]

### 2.3.1 Standard Orientations

This section describes the procedures followed to place the model into the initial configuration that is consistent with the ISO standard, with the exception that the abduction angle was greater than that described by the standard. First, the acetabular liner was rotated to an abduction angle of  $60^\circ$ , which was  $15^\circ$  beyond the conventional  $45^\circ$  angle specified in the standard; the additional  $15^\circ$  was implemented to model a severe but

realistic liner orientation that increases the propensity for subluxation and edge loading. Next, the acetabular liner was rotated by an anteversion angle of  $20^\circ$ . Then, the femur sub-assembly was oriented in the following steps:  $3^\circ$  of adduction, then  $4^\circ$  of net external rotation, and finally  $25^\circ$  of flexion.

### 2.3.2 Feasible Setup Orientations

The procedures described in the previous section produced a configuration in which the load line (represented by the line labeled “L” in Figure 5a) is at a certain angle from the vertical. This section provides the motivation and the procedures to reorient the configuration to best suit the constraints of the testing equipment. The full assembly was rotated such that the load line was vertical, and it was inverted because (1) the test frame is set up such that it applies vertical loads, (2) to be stable under self-weight, the femur is suspended rather than supporting its weight from the bottom and, (3) the actuator is bottom-mounted in the available test frame. These orientations include rotating the full assembly by  $20^\circ$  about a medial-lateral (M/L) axis, followed by orienting the load line to a vertical orientation as illustrated in steps 7 and 8 in Appendix A. Finally, the BMR model assembly was anatomically inverted, because this orientation better suited the configuration of the test machine and the fixtures described in later chapters.

### 2.3.3 Final Configuration

The BMR model as configured for experimental trials, after applying the orientations previously described, is illustrated in **Error! Reference source not found.** The pelvic sub-assembly was angled at  $40^\circ$  with respect to an X-Z plane (a transverse anatomic plane). The required femur orientation of  $8.6^\circ$  was implemented in the experiments using a fixture that provided the 64 mm horizontal offset between the distal

pin axis and the vertical load line. The load line passed through the center of the acetabular liner. This configuration was implemented in the FEA using software inputs of the dimension values.

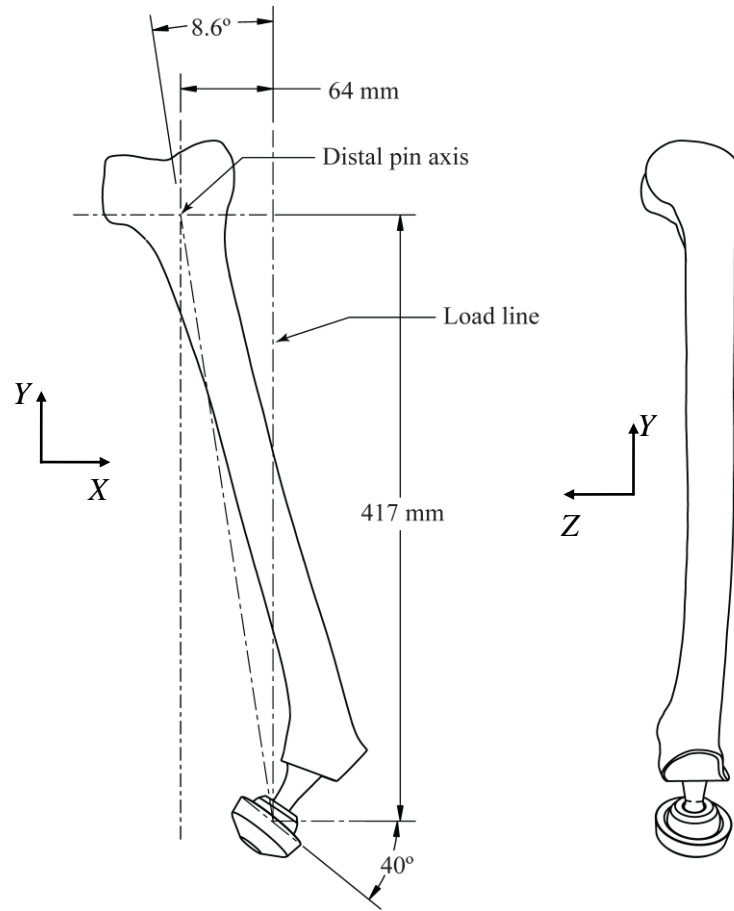


**Figure 6:** Macro view of the BMR Model

## 2.4 Initial Conditions

The polar separation gap (PSG) is the distance between the liner's internal spherical surface (its *ID*) and the head, measured parallel to the liner's axis of symmetry, as shown in Figure 7. The means of implementing the desired PSG dimensions are described in Section 4.8.2 for the experiments and in Section 5.4 for the FEA.

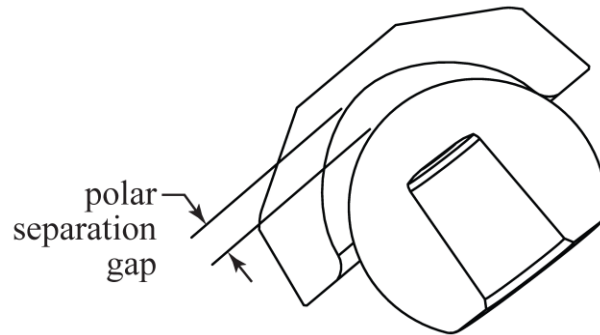


**Figure 7:** The Polar Separation Gap (PSG)

## 2.5 Inputs and Boundary Conditions

The model's inputs and BCs were designed to cause and constrain rapid reduction of a subluxed femoral head. In the human body, the pelvis, the subluxed hip joint, and the knee joint at the distal end of the femur each have six degrees of freedom (DOF) and are acted upon by numerous restraints (e.g. ligaments and opposing joint surfaces) and active elements (various muscle groups). Creating a high-fidelity model representing all such BCs would be a tremendous undertaking beyond the scope and resources of this project. However, because the reduction event involves a short (roughly 2 mm) femoral head trajectory with only small displacements and rotations of the pelvis and femur, it was feasible to faithfully model the reduction motion by implementing limited degrees of freedom in the model's BCs. Furthermore, the sudden femoral head reduction is essentially a reaction to external forces rather than a motion instigated by muscular contractions. It is a reaction to gravity acting vertically on the body and the ground reaction force acting vertically through the femur via the foot and the tibia at the instant of heel strike. Therefore, the BMR model simplified the BCs to act along a single,

vertical axis, and it neglected any input from voluntary muscle contractions. The model's third key BC was a passive element (lateral spring force, **Error! Reference source not found.**) that instigated the initial femoral head subluxation along with a small edge-load contact force. Each of these three key BCs is further described below, and their specific realizations in the experimental and analytical contexts are described in later chapters.

In-vivo, the distal condyles of the femur (Figure 8) are seated on the tibial condyles. During normal gait, when the heel strikes the ground, the reaction emanating from the heel strike gets transferred through the femur to the hip joint and causes the femoral head to relocate into the acetabular liner. During this reduction motion, the femoral head moves only a short distance relative to the pelvis. In the BMR model, this motion is effectively represented by rotation about an axis allowing a single rigid-body DOF of the femoral sub-assembly. Hence, the distal end of the femur is fixed except for rotation about an axis along the anterior-posterior (A/P) direction passing through the distal metaphysis and between the condyles. This *distal pin axis* is shown in Figure 8.

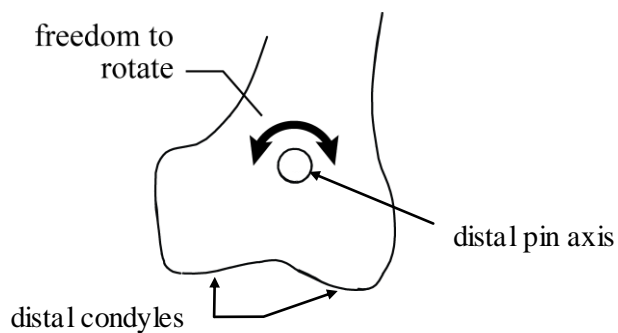


**Figure 8:** A/P axis of rotation in BMR model

The muscles and tendons around the skeleton in-vivo constrain the movement of the skeleton. The soft tissues surrounding the hip help the femoral head in constraining its movement within the acetabular liner. In the BMR model, a lateral force is used to

maintain contact between the femoral head and the liner during subluxation. Specifically, this force is applied horizontally in the frontal plane at an anatomical position below the femur's greater trochanter (Figure 9).

In-vivo, the acetabulum is supported by the pelvis. In the BMR model, the acetabular shell is press-fit into a polyurethane block representing the pelvis (Figure 10). All the components of the pelvic sub-assembly move together, as controlled by a dynamic input provided by an MTS actuator.

During the heel-strike phase, the contact force between the bearing surfaces is a result of the ground reaction force at the heel. The input given to the acetabular sub-assembly in the BMR model causes a forced reduction of the femoral head into the liner, similar to the reduction caused by heel strike in normal human gait.

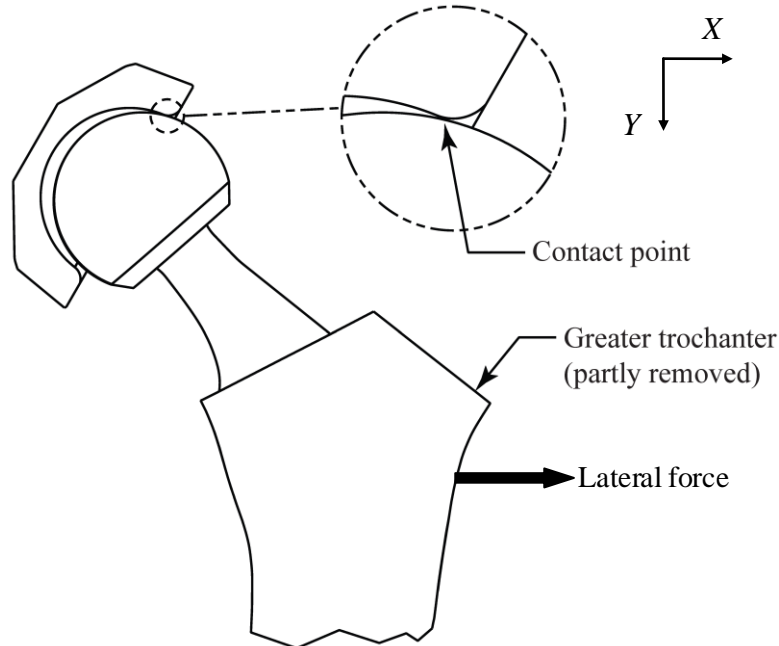


**Figure 9:** Lateral force application to achieve a forced contact between the femoral head and the acetabular liner

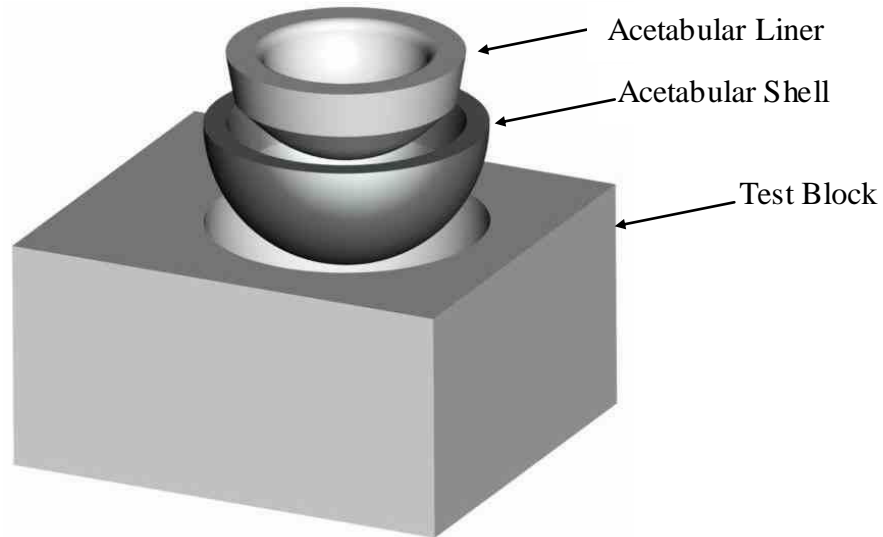


**Figure 10:** The pelvic sub-assembly showing its components – acetabular liner, acetabular shell, and model pelvis (rigid polyurethane test block)

## 2.6 Rigid Body Analysis of BMR Model

Rigid body analysis is a valid and applicable analysis approach when material deformations are insignificant. The BMR model involves biological materials which are compliant in nature, and the material deformations might have a substantial effect on the system response. Nonetheless, a rigid body analysis of the BMR model was performed to provide a low-order estimate of the model's response to the applied forces and moments.

Specifically, the effect of the lateral spring force on the contact force between the bearing members was estimated in this analysis. This analysis showed us that, with the present design of the BMR model, the effect of the spring force on the contact force is greater than the effect of the inertia of the femoral sub-assembly on the contact force.

### 2.6.1 Equations of Motion

Figure 11 shows a free body diagram (FBD) of the BMR model illustrating the applied forces and reaction forces. Table 2 describes the symbols used in the FBD. Since

this analysis is limited to planar rigid body motion, the femoral sub-assembly is considered to be rotating about point ‘ $O$ ’ (the distal pin axis described in Section 2.5). The components of the model other than the directly contacting members (femoral head and acetabular liner) were represented using simple geometries. Accordingly, a line connecting the distal pin axis and the femoral head center represented the femur and the femoral stem geometries. In the actual experiment, the contact force acting on the femoral head was generated by controlling the test machine’s actuator to provide a pre-defined dynamic velocity record.

According to Newton’s Second Law,

$$\sum_i \mathbf{F}_i - m\mathbf{a} = 0 \quad (1)$$

where  $\mathbf{F}_i$  are the applied forces,  $m$  is the mass of the femoral sub-assembly, and  $\mathbf{a}$  is the acceleration of the center of mass of the femoral sub-assembly.

Recognizing that sliding is occurring, Newton’s second law, applied in X and Y directions, gives respectively

$$C_N(\mu \cos \theta - \sin \theta) - R_x + C_S - ma_x = 0 \quad (2)$$

$$C_N(\cos \theta + \mu \sin \theta) - R_y - W - ma_y = 0 \quad (3)$$

According to D’Alembert’s principle, the moments about point  $O$  can be written as

$$\sum M_O - I_O \alpha = 0 \quad (4)$$

where  $\sum M_O$  is the sum of the moments of all the forces (acting on the system) about point  $O$ ,  $I_O$  is the mass moment of inertia about point  $O$ , and  $\alpha$  is the angular acceleration.

For the simple dynamic analysis, Eq. 4 can be written in terms of the forces and the moment arm lengths (labeled in Figure 11) as

$$(\mu t - n) C_N + s C_S - x W - I_O \alpha = 0 \quad (5)$$

Eq. 5 was further analyzed by substituting the appropriate values of the applied forces and the corresponding moment arm lengths to determine the effect of the spring force on the contact force.

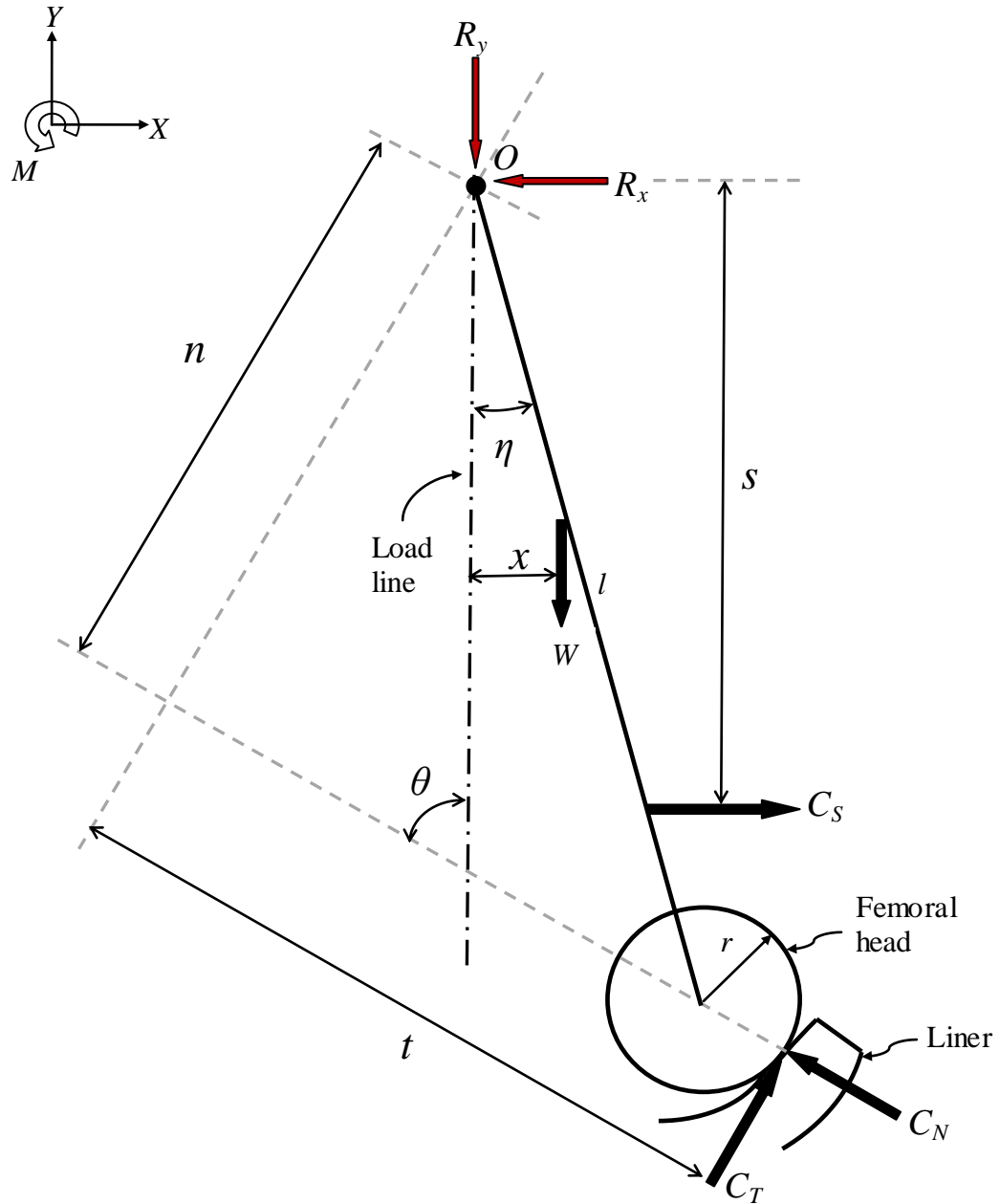


**Figure 11:** Free body diagram of the BMR model (liner partly shown)

**Table 2:** Description of the symbols used in the FBD of the BMR model

Symbol	Description of the symbol
$O$	Distal pin axis
$C_N$	Normal contact force
$C_S$	Tangential contact force (due to friction)
$C_T$	Applied lateral spring force
$I_o$	Inertia of the femoral sub-assembly about point $O$
$M_o$	Moment about the pivot point
$R_x, R_y$	Reaction forces at the pivot point in X and Y directions respectively
$W$	Weight of the femoral sub-assembly
$l$	Length of the liner joining the distal pin axis and the center of the femoral head
$n$	Length of the moment arm of $C_N$
$r$	Radius of the femoral head
$s$	Length of the moment arm of $C_S$
$t$	Length of the moment arm of $C_T$
$x$	Length of the moment arm of $W$
$\mu$	Coefficient of friction
$\eta$	Angle subtended by $C_N$ with the vertical
$\theta$	Angle subtended by the line joining the distal pin axis and the center of the femoral head with the vertical

### 2.6.2 Effect of the Spring Force on the Contact Force

Equation 6, (manipulated version of Eq. 5), was analyzed to estimate the effect of the spring force on the contact force.

$$C_N = \frac{s}{(n-\mu t)} C_S - \frac{x}{(n-\mu t)} W + \frac{I_o}{(n-\mu t)} \alpha \quad (6)$$

The objective of the rigid body analysis was to estimate a contact force value for a given value of the spring force and to further estimate how the contact force varied over a range of spring force values in order to better understand the system response. The spring force ( $C_S$ ) value was treated as a constant, which neglected changes due to extension of the spring (+2 N variation) during the reduction event. The mass properties ( $W$  and  $I_o$ ) of the femoral sub-assembly were determined from its 3D model in SolidWorks (Dassault Systemes, SolidWorks Corp., Waltham, MA). The angular acceleration of the femoral

sub-assembly was computed based on a linear acceleration at the contact point. The linear acceleration value was determined using the derivative of the velocity recorded in an experimental trial with the BMR experiment configuration. The coefficient of friction ( $\mu$ ) was 0.06, a value taken from the literature [45]. These values were substituted in Eq. 6 to estimate the contact force ( $C_N$ ).

The rigid body model was also used to qualitatively analyze the effect of coefficient of friction ( $\mu$ ) on the velocity of the femoral head as described in the Discussion chapter.

Equation 6 was analyzed by substituting the corresponding values of the inputs (on the right hand side of Eq. 6) and a range of spring force values (0 – 200 N). Though the rigid body analysis performed was a simpler version of the actual model and the estimations in this analysis are not comparable to the non-rigid analysis, it was concluded that the BMR model was sensitive to the value of the spring force chosen. As seen in Figure 12 the contact force increased as the spring force increased. Nevelos et al. [30] used a lateral spring force of 400 N (though the details of how and where the spring force actually was applied were not mentioned). The same value of the spring force in the rigid body analysis of the BMR model gave a contact force estimate of about 800 N.

The estimation of contact force using the rigid body analysis provided us the background to design the lateral spring, i.e., the spring force value, used in the BMR model. Micro-separation was achieved using a relatively low value of the spring force, 105 N; this value was about 1/4<sup>th</sup> of a similar lateral spring force used in hip simulators previously [30]. There are no springs in human bodies, but a spring in the BMR model was incorporated to achieve the desired PSG and to maintain a forced contact on the rim

of the liner. Also, even though the femoral head subluxes, the femoral head and the acetabular liner rim are in forced contact (as determined by fluoroscopic imaging [27]) due to the low magnitude forces exerted by the soft tissues. The lateral spring, though not physically present in the human body, represents the net effect of the soft tissue forces in high Deborah number loading, and it maintains a forced contact between the head and the liner during subluxation, to mimic clinically observed prosthetic hip joint kinematics.

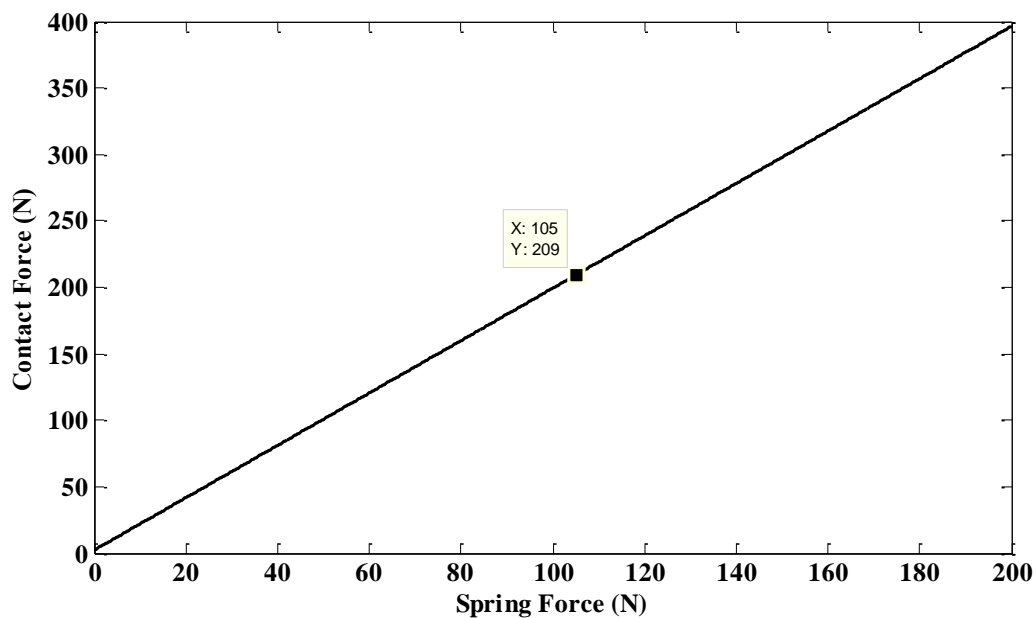


**Figure 12:** Contact force vs. Spring force according to the rigid-body analysis; for reference, the data point on the plot shows the contact force for the spring force value used in the BMR test

The BMR model includes biological components, such as the femur, which are more compliant than the implants. So, we think that the femur's compliance will have a significant effect on the contact mechanics, which is the key hypothesis. Hence, there is a need to include the compliance in the components of the model. So, the BMR model was examined mathematically and experimentally as described in further chapters.

## CHAPTER 3

### ELEMENTARY ANALYSIS AND TESTING<sup>2</sup>

#### 3.1 Introduction

A low-speed structural axial impact test of two slender rods was conducted in a drop tower to validate corresponding models of contact mechanics. Analytical and finite element (FE) models of the contact and vibration were validated by the laboratory testing results. The following describes the purpose, scope, method of testing and some preliminary analyses carried out before the test.

The purpose of this test was to examine the contact-coupled longitudinal impact mechanics between two rods. From the predictions of this simple test and the adaptability of the diagnostics, this test serves the purpose of substantiating instrument calibration and establishing a strong theoretical and laboratory framework for using the same methods in an experimental and computational study of a more complicated biomechanical analysis (detailed in later chapters). It was hypothesized in this elementary testing that the contact duration of the rods would be twice the transit time of the stress wave initiated at the contact. A similar effect was expected in the biomechanical analysis of the femur.

---

<sup>2</sup> Much of the material in this chapter is repeated from [44].

### 3.2 Problem Statement

As illustrated in Figure 13, a first rod, Rod 1, centrally impacts an initially stationary second rod, Rod 2. Both the rods are placed coaxial to each other. Rod 1 is spherical at its impacted end and has a flat distal end. Rod 2 has both ends flat. Dimensional details are given in Table 3 and Table 4. Impact of Rod 1 onto Rod 2 gives rise to a small contact area. Away from the contact area, all surfaces are traction free. To prevent rotation of the rods in the experiment, the distal ends are outfitted with o-rings or tape, which impose negligible lateral stress in comparison to the axial stress. The objectives of this test were to measure (1) the contact area, (2) the wave propagation speed and, (3) the strains at the midpoint of Rod 2.

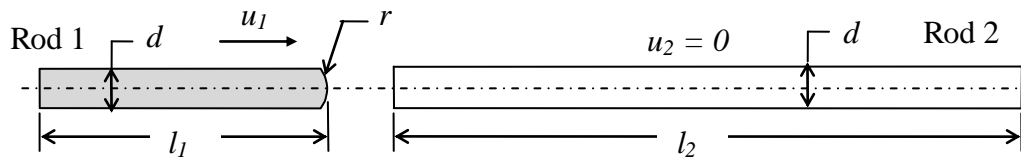


**Figure 13:** Schematic of the impacted rods

**Table 3:** Dimensional details of the rods

	Material	Length (mm)	Diameter (mm)	Tip radius (mm)	Impact speed (m/s)
Rod 1	A2 tool steel, Rc 60	250.99 ( $l_1$ )	12.7 ( $d$ )	35 ( $r$ )	2.197 ( $u_1$ )
Rod 2	A2 tool steel, Rc 60	700.99 ( $l_2$ )	12.7 ( $d$ )	flat	Initially stationary ( $u_2 = 0$ )

**Table 4:** Material properties of the rods

Young's modulus	Poisson's ratio	Density
204.3 GPa	0.3	7803 kg/m <sup>3</sup>

### 3.3 Methods

The problem was solved using finite element analysis (FEA), which was verified against an analytical solution and was validated against laboratory testing.

#### 3.3.1 Laboratory testing

A schematic of the experimental setup is shown in Figure 14. A total of four rods (three of Rod 1 and one of Rod 2) were used to carry out the test with repeated trials. Both rods were made of precision ground A2 tool steel, hardened and tempered to Rc 60, from a single lot. The isotropic elastic material properties of the rods were determined from testing the rods by the impulse excitation method, ASTM E 1876, using a Grindosonic MK5 instrument (Lemmens, Lueven, BLG).

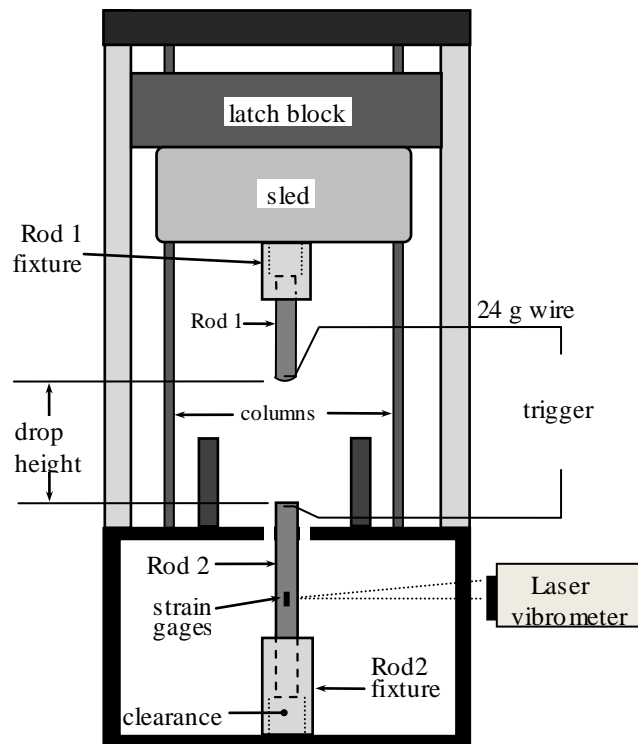


**Figure 14:** Schematic of the two rod impact test

The impact test was conducted in an Instron drop tower apparatus (Model 8250 HV, Instron Corp., Norwood, MA). The apparatus consisted of a motorized latch block from which a sled is suspended. As per the computer command, the sled may be released from the latch block into free fall sliding along two columns. Rod 1 and Rod 2 were suspended in tubular fixtures as shown in Figure 16; these fixtures mounted on the sled and the base of the test apparatus. Both fixtures had o-rings on the inside diameter (shown in detail A of Figure 16) that gripped each rod just tightly enough to hold each static and had sufficient clearance behind the rods' distal ends for the rods to travel freely after the impact. The weight of Rod 1 was suspended by a thin strip of tape wound around its distal end to prevent it from sliding out of the fixture; otherwise, Rod 1 was distally unconstrained. Rod 2 was distally placed on a plastic plug press-fit into the tube. Upon impact, the friction holding the rods in place by the o-rings was overcome, and the rods each displaced axially. The two rods used in the experiment are shown in Figure 15.

The quantities measured in the laboratory testing were the contact area on Rod 1 and the wave propagation speed and the strain in Rod 2. The measurement techniques are described below.



**Figure 15:** Rod 1 (shorter) and Rod 2 (longer) used in the impact test; a US quarter is shown for reference to set scale

A 3D laser Doppler vibrometer (CLV-3D, Polytec, Germany) was used to measure the velocity by focusing the laser tip on the mid-point of Rod 2, as shown in Figure 17a. Two foil strain gauges installed at the midpoint of Rod 2 (as shown in Figure 17b) were used to measure the strain. A strain gauge signal conditioner (Model 2310B Vishay Measurements Group) amplified the strain values obtained in the test. A data acquisition system (DAQ, USB 1604HS, Measurement Computing, Norwood, MA) interfaced with LabVIEW (National Instruments, Austin, TX) was used to acquire data. The rods were wired with 24g wire into a 3V electrical circuit that was also wired into one channel on the DAQ. Rod impact completed the circuit and triggered the start of data collection.

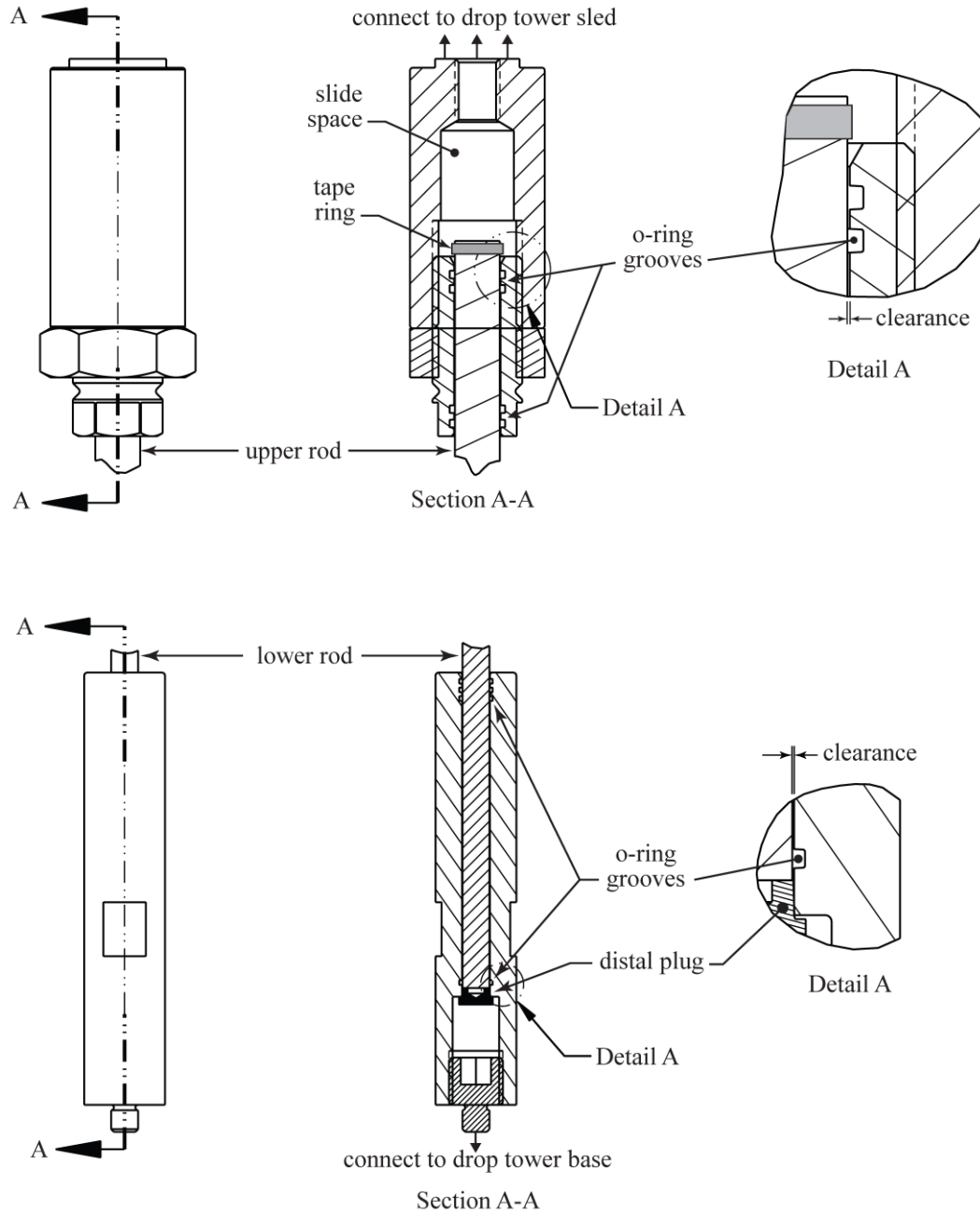


**Figure 16:** Fixtures to hold Rod 1(top) and Rod 2 (bottom)

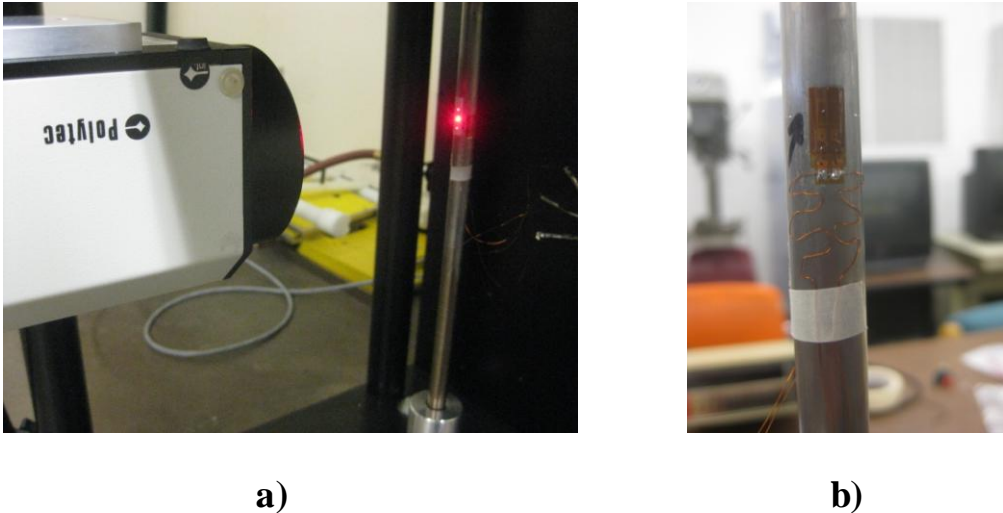


**Figure 17:** a) Laser focused at the midpoint of Rod 2; b) Strain gage installed at the midpoint of Rod 2; second strain gage installed on the opposite side of the first one

### 3.3.2 Axisymmetric Finite Element Modeling

A 2D axisymmetric model of the rods and the 2D meshes was generated using LS-Prepost (Livermore Software Technology Corp., Livermore, CA) and consisted of 2D 4-node solid elements. Contact between the rods was modeled as a 2D surface-to-surface contact. The FEA had three mesh refinements of Rod 2 to examine convergence. The element aspect ratios were approximately 1:1, and the meshes were refined by serially halving the average length: from 0.42 mm (coarse), to 0.21 mm (medium), to 0.105 mm (fine). The finite element code LS-Dyna (Livermore Software Technology Corp., Livermore, CA) was used to solve the axisymmetric model and its refinements. Post-processing was done using LS-Prepost.

### 3.3.3 3D Finite Element Analysis<sup>3</sup>

To establish confidence in the methods used to analyze the 3D femur, the two-rod impact test was also analyzed using a 3D model [46]. This model used hexahedral elements, penalty contact algorithm and explicit time integration. A submodel taken from the vicinity of the contact region in the initial global model was used to further refine the analysis. Three mesh refinements of the submodel were used to assess convergence. This model also was verified using an analytical model and validated using the above mentioned experiment. The accuracy of the results in this simple analysis using the submodeling technique established confidence that a similar technique could be used in the computational study of the complicated impact mechanics of artificial hip joints.

### 3.4 Results: Comparison of Analytical, Experimental and Axisymmetric FEA

The results compared are (1) speed at the midpoint of Rod 2, (2) strain at the midpoint of Rod 2 and, (3) contact area on the rounded surface of Rod 1. Results from two experimental trials each of Rod 1 specimen are summarized in [46]. The experimental results provided here are those of Rod 1, Specimen 1, Trial # 3.

The contact area on the rounded surface of Rod 1 in the experiment, shown in Figure 18 a and b, was recorded by a fingerprinting technique [46]. In the axisymmetric model, the distance between two extreme nodes of the line of maximum stress at the contact was measured using LS-Prepost. The contact area on Rod 1 is from a single mesh generated fine enough such that three elements of the slave (Rod 2) are in contact within an element of the master (Rod 1). Table 5 compares the contact radius and contact area measured by the three methods. The speed and the strain data both recorded at the midpoint of Rod 2

---

<sup>3</sup> Performed by Exponent, Inc., under our direction.

are overlaid on the analytical [46] and axisymmetric FEA results, as shown in Figure 19 and Figure 20 respectively.

Convergence was studied on the 2D axisymmetric model for the recorded speed and strain. The errors in the computational and the experimental methods were determined against the analytical solution by taking a root mean square (RMS) difference of the quantities over time, with results tabulated in Table 6. The values show a decrease in the RMS error with mesh refinement. The difference in the RMS errors for the strain is not uniform through the mesh refinement because limitations of the software's data output capability required interpolating the FEA time histories.

**Table 5:** Contact radius and area from the axisymmetric fine model in comparison to the analytical and experimental results

	Analytical	FEA	Experimental	$\Delta$ , Analytical vs. FEA / Experimental
<b>Contact radius (mm)</b>	1.09	1.1	1.109	-0.9% / -1.7%
<b>Contact area (mm<sup>2</sup>)</b>	3.73	3.799	3.86	-1.8% / -3.5%

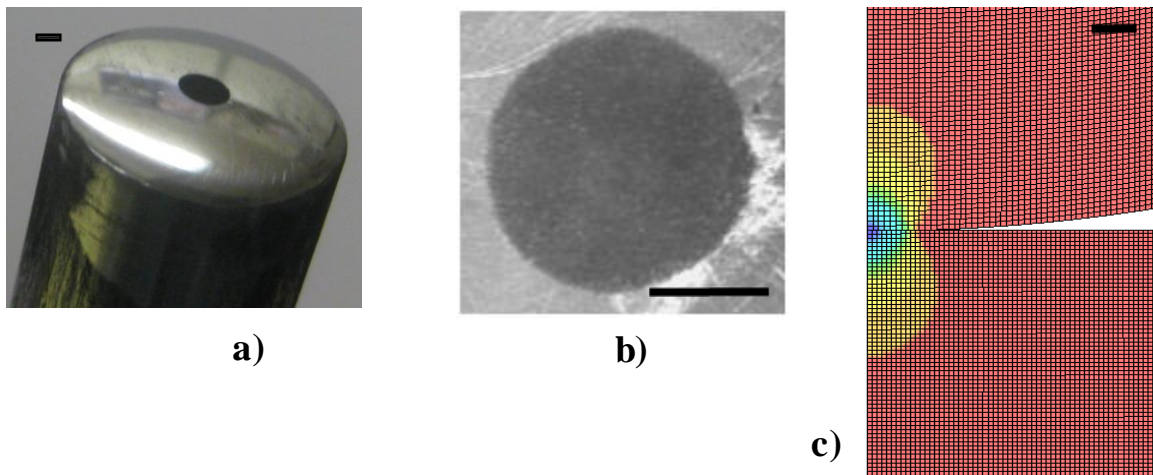


**Figure 18:** Contact patch area on the round surface of Rod 1 during the impact, recorded a) from a hand-held digital camera, b) from optical CMM; c) Stress contour plot from which the contact radius was measured is shown for the fine mesh of 2D axisymmetric model of Rod 1 and Rod 2 with their axes pointing downward (full length of the mesh not shown); Black horizontal lines on a corner of each figure shows scale to 1 mm.

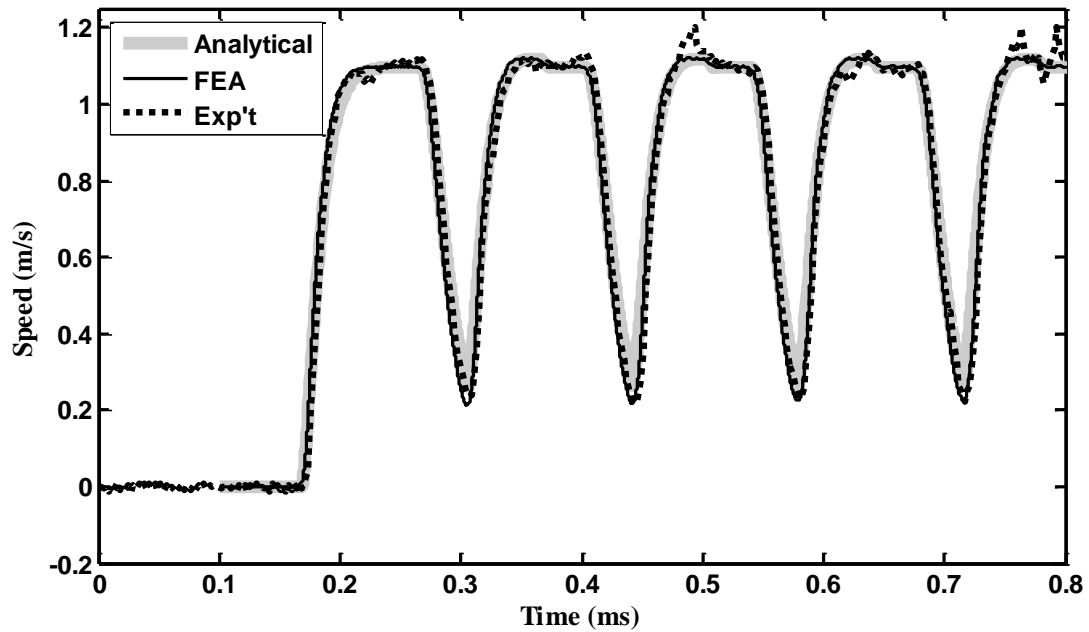


**Figure 19:** Axisymmetric fine mesh results of speed measured at the midpoint of Rod 2 overlaid with analytical and experimental data

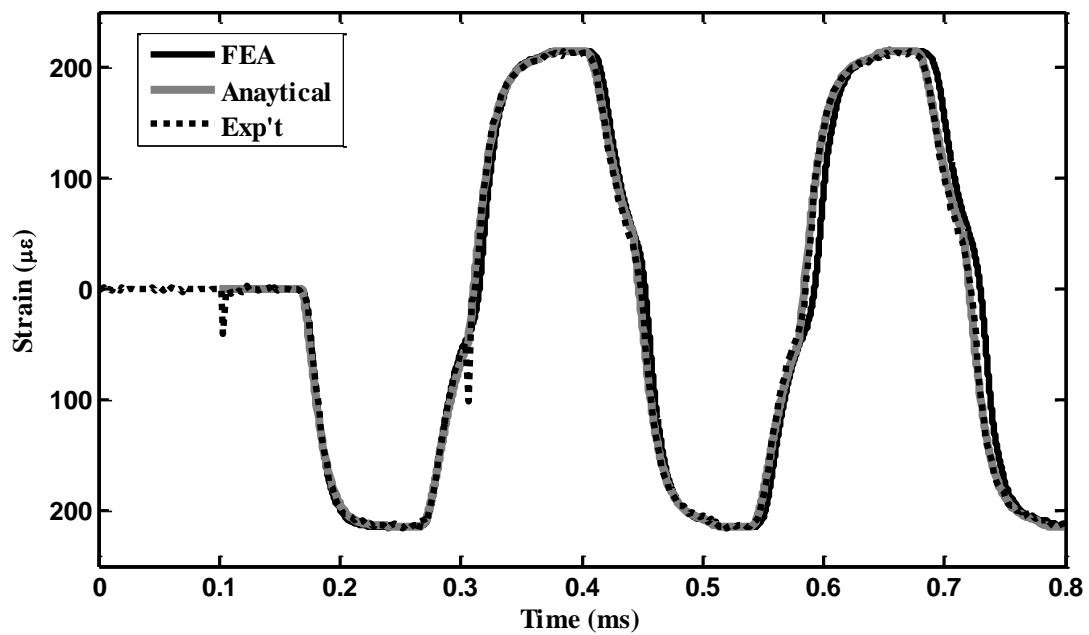


**Figure 20:** Axisymmetric fine mesh results of strain measured at the midpoint of Rod 2 overlaid with analytical and experimental data

**Table 6:** RMS errors of speed and strain of the axisymmetric FE model (error analysis performed against the analytical solution)

<b>Axisymmetric FE model</b>	<b>RMS <math>\Delta</math> speed (m/s)</b>	<b>RMS <math>\Delta</math> strain (<math>\mu\epsilon</math>)</b>
<b>Coarse</b>	0.3	78.68
<b>Medium</b>	0.285	78.12
<b>Fine</b>	0.27	60.82

### 3.5 Conclusion

The results of the longitudinal impact of slender rods analyzed using the three methods (analytical, experimental, and FE) gave high reliability to our methods for analyzing and measuring the dynamic structural response of a simple system. This test performed in the laboratory served as a major platform to faithfully apply the same laboratory techniques in studying the transient dynamics of prosthetic hip joints. For FEA involving intricate shapes like biological components (for example, the femur), solving a 3D dynamic problem involving millions of elements and nodes might be computationally inefficient. Also, in contact problems, contact mechanics cannot be directly measured. For example, contact force cannot be directly measured experimentally. As in [46], the submodeling FE approach taken to solve this simple problem of two-rod impact – with computational efficiency – may be followed in solving complex problems such as those involving artificial hip joints.

## **CHAPTER 4**

### **LABORATORY TESTING OF BMR MODEL**

#### **4.1 Introduction**

A physical rendition of the BMR model was tested dynamically in the laboratory to measure its response to sudden femoral head reduction. Three separate response parameters were measured: (1) the velocity of the femoral head, (2) the strain on the femoral neck, and (3) the strain on the femoral shaft. The experimental setup is shown in Figure 21. The model was tested using a servohydraulic test frame (MTS, Eden Prairie, MN). Strain gages measured the two strain parameters, and a laser Doppler vibrometer measured the femoral head velocity. Trials were performed for three different PSG values: 2, 3, and 4 mm. The measured response parameters would later serve to validate a finite element simulation of the BMR model undergoing the same sudden reduction event.

#### **4.2 The Femur Construct**

Researchers have substituted composite femurs for cadaveric ones because the composite femur's consistent properties and shape are conducive to repeatable biomechanical testing and analyses [47, 48]. Fourth generation composite femurs (4GCFs, the most recent design) are commercially available (Pacific Research Labs, Inc., Vashon, WA) both as physical models and as 3D CAD (computer aided design) models. Researchers prefer composite femurs over cadaveric femurs due to various reasons –

(1) composite femurs have very little inter-specimen variability, especially compared with natural femurs, which vary greatly from person to person, (2) composite femurs are easily available and, (3) composite femurs are easy to store. Since the introduction of composite femurs in 1987, research scientists have improved the composite femurs from the 1<sup>st</sup> generation to the 4<sup>th</sup> generation. The cortex of the 4GCF is made up of short glass fiber reinforced epoxy. The material properties such as stiffness, tensile strength, and fracture toughness of the 4GCF cortex were tested and reported to be close to human femur cortex material [49]. One such commercially available 4GCF was used throughout this project.

A femur construct (femoral sub-assembly) was prepared by implanting the composite femur (Model 3406 large left) with prosthetic hip implants. The femur was prepared using mock surgical techniques following the directions of the femoral stem manufacturer. The femoral head was removed with an oscillating saw, the distal intramedullary canal was cylindrically reamed, and the proximal metaphysis was broached with successively larger broaches. The proximal portion of the greater trochanter was removed to provide a line of sight to the laser used for femoral head velocity measurements. The trochanter is not normally resected in THA; however, its removal was a reasonable modification of typical surgical technique, because the trochanter lies outside of the load-bearing path when the femur is axially compressed. A proximally porous coated, titanium femoral stem (Encompass<sup>TM</sup>, Ortho Development, Draper, UT) was press-fit into the surgically prepared femur. The particular size of femoral stem was chosen based on the sizes of the final distal reamer and final broach used in the surgical preparation. A Ø36 mm Al<sub>2</sub>O<sub>3</sub> femoral head (BioloX Forte, Ceramtec,

Germany) was mated with the femoral stem trunnion. The proximal end of the femur construct is shown in Figure 22. A dowel pin press-fit into the distal end of the femur between the condyles served as the distal pin axis described in Section 2.5.

The material properties of the synthetic femur, the prosthetic hip implants, and the test block used to hold the acetabular components are summarized in Table 7. Note that the femoral cortex properties listed in Table 7 are manufacturer-provided values that were not used in the FEA analyses; more accurate values were determined by a calibration process described in Chapter 5, Section 5.3.

**Table 7:** Material properties of the components of the BMR model

Component		Material	Density (kg/m <sup>3</sup> )	Elastic Modulus (GPa)	Poisson's ratio
<b>Femur</b> <sup>1</sup>	Cortical shell	Short fiber filled epoxy	1640	13.7	0.42
	Cancellous bone	Polyurethane foam	270	0.155	0.35
<b>Implants</b>	Femoral Head <sup>2</sup>	Al <sub>2</sub> O <sub>3</sub>	3960	380	0.26
	Acetabular Liner <sup>2</sup>	Al <sub>2</sub> O <sub>3</sub>	3960	380	0.26
	Acetabular Shell <sup>3</sup>	Ti-6Al-4V	4430	113.8	0.342
	Femoral Stem <sup>3</sup>	Ti-6Al-4V	4430	113.8	0.342
<b>Model pelvis</b> <sup>1</sup>	Test block	Polyurethane foam	480	0.462	0.3

<sup>1</sup> Pacific Research Labs, Inc., Vashon, WA

<sup>2</sup> [34]

<sup>3</sup> www.matweb.com as viewed on Oct 6, 2010

### 4.3 Fixtures and Initial Alignment

Custom-made fixtures suspended the femur construct by its distal end from the test frame's load cell (refer to labels in Figure 21). The adapter plate provided the 64 mm horizontal offset, labeled in Figure 21, needed to configure the femur per the ISO standard initial conditions. The U-bracket held the femur by means of the press-fit dowel

pin shown in Figure 23. The adapter plate and u-bracket were squared and tightened to each other prior to assembly in the test frame. They were tightened to the load cell after first rotating the entire femur and fixture sub-assembly to align the femoral stem's coronal plane with that of the acetabular liner, as visually judged. Spherically tipped set screws were threaded through the arms of the U-bracket and mated with the ends of the femur's distal pin, providing greased joints and forming the femur's rotation axis.

At the bottom of the entire assembly, a thick aluminum base plate was attached to the top of the load frame's actuator. A sine plate was clamped to the base plate using strap clamps. The sine plate was angled at  $40^\circ$  to set the required acetabular abduction angle. Furthermore, the sine plate was aligned on the base plate such that the centerline of the actuator passed through the center of the acetabular liner. This alignment was established using known dimensions of the base plate and precision gauge blocks that were contacted against a femoral head sitting in the liner. To set the anterior-posterior (A/P) position of the liner relative to the femur, the pelvic sub-assembly was positioned on the sine plate, pushing it with a micro-threaded adjustment screw (attached to the sine plate) until a trial edge contact, between the femoral head and the liner's edge, was observed to occur on the lowest part of the edge. This alignment was judged visually from the liner's lateral side and was aided by illuminating the interior of the liner with a strong pen light from the medial side of the femoral head. This careful alignment was necessary to ensure that the femoral head was centered with respect to the liner and would slide along the liner's coronal plane during the reduction tests, as it would in the finite element simulation. Once this alignment was achieved, the pelvic sub-assembly was fixed to the sine plate

using strap clamps, which were added to remove visible slipping that was (without them) evident when using only the locking mechanism of the sine plate itself.

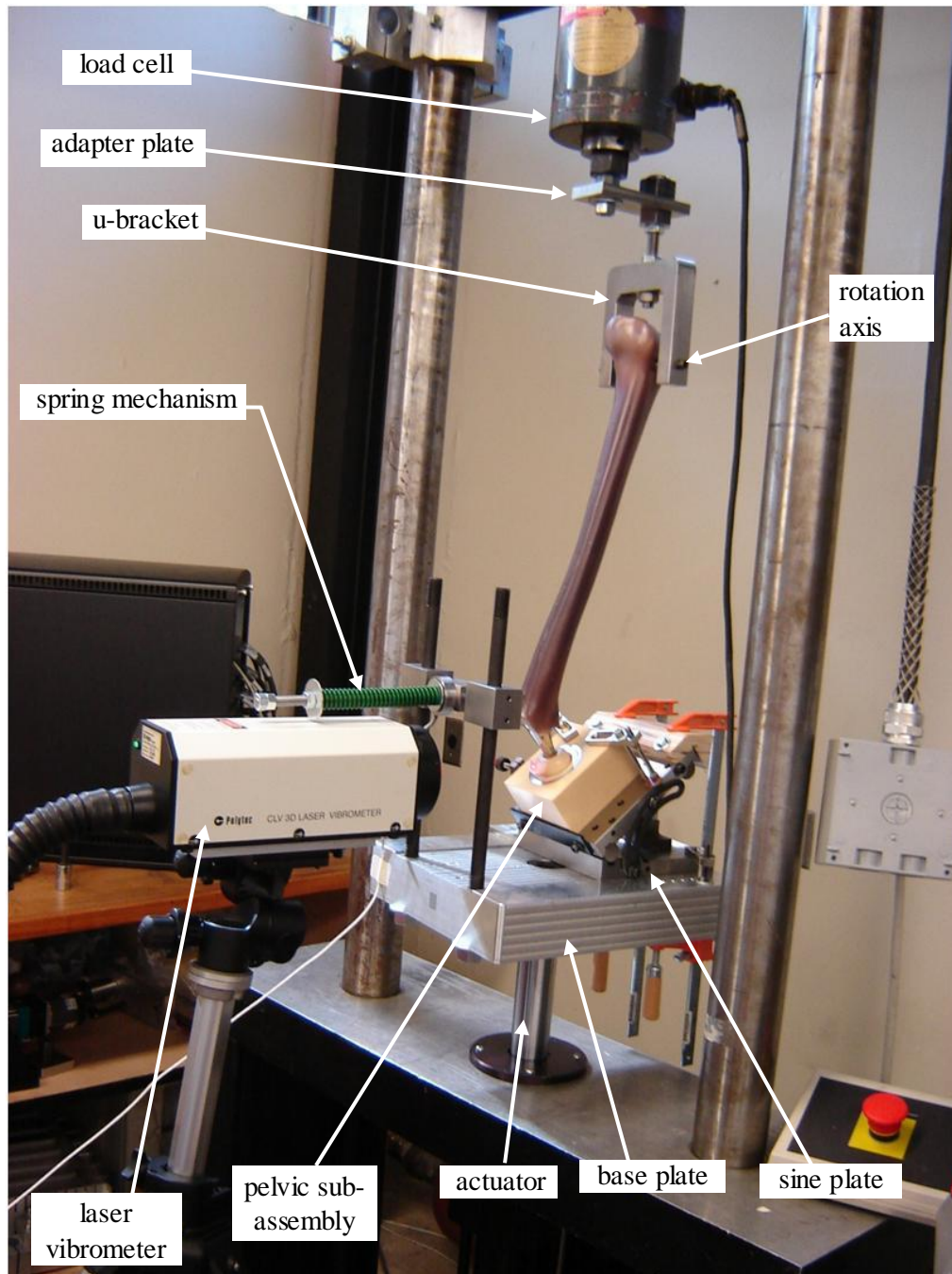


**Figure 21:** Experimental setup of the BMR model



**Figure 22:** Proximal end of the femur construct; assembly of synthetic femur and implants – femoral stem and femoral head; the femur’s greater trochanter was resected to provide a line of sight for the laser velocity measurement described in Section 4.5



**Figure 23:** Distal end of the femur construct with a press-fit dowel pin between the condyles

The fixtures’ stiffness was determined in a separate static test. The BMR model was entirely assembled as if for an actual trial. The test frame was rigged with a dial indicator (resolution 0.0001 in.) on an articulating arm. The indicator was posed horizontally and

its tip was placed in contact with the femur's distal pin axis (i.e., one set screw protruding from an arm of the U-bracket). The actuator was displaced until the load cell registered a compressive load approximately equal to that observed in an actual reduction trial, and the deflection of the pin axis was measured from the dial indicator. A static free-body-diagram analysis of the fixtures revealed the horizontal force on the pin, and this value, divided by the measured horizontal pin deflection, gave an effective horizontal stiffness of the fixtures. A similar procedure yielded the fixtures' effective vertical stiffness. These values were later implemented to effect a realistic compliance at the distal pin axis in the FEA of the BMR model.

#### **4.4 Spring mechanism**

A spring mechanism (refer to labels in Figure 21) was used to establish a lightly loaded contact between the femoral head and the edge of the liner, as illustrated in Figure 9. The connecting rod (Figure 24) ran through the inside of the compression spring, and the end of the rod was hooked together with the hook that was screwed into the lateral side of the proximal femur. The compression spring was squeezed between the adjustment nut and the rotation block (labeled in Figure 24a) through which the connecting rod passed, and this mechanism applied a laterally directed force to the femur, thus pulling the head into contact with the liner's rim. The mechanism permitted the connecting rod to slide in the rotation block, and the rotation block could rotate about a fixed axis. Thus, the connecting rod could slide and rotate to follow the movement of the proximal femur without constraining the femur's movement, other than via the spring force. The mechanism included a donut load cell (LC8150-500, Omega, Stamford, CT) to measure the force, along with an amplifier and a voltmeter to register the load cell's

output. The initial spring force – established in the subluxed, edge-loaded condition – was 105 N in all trials.

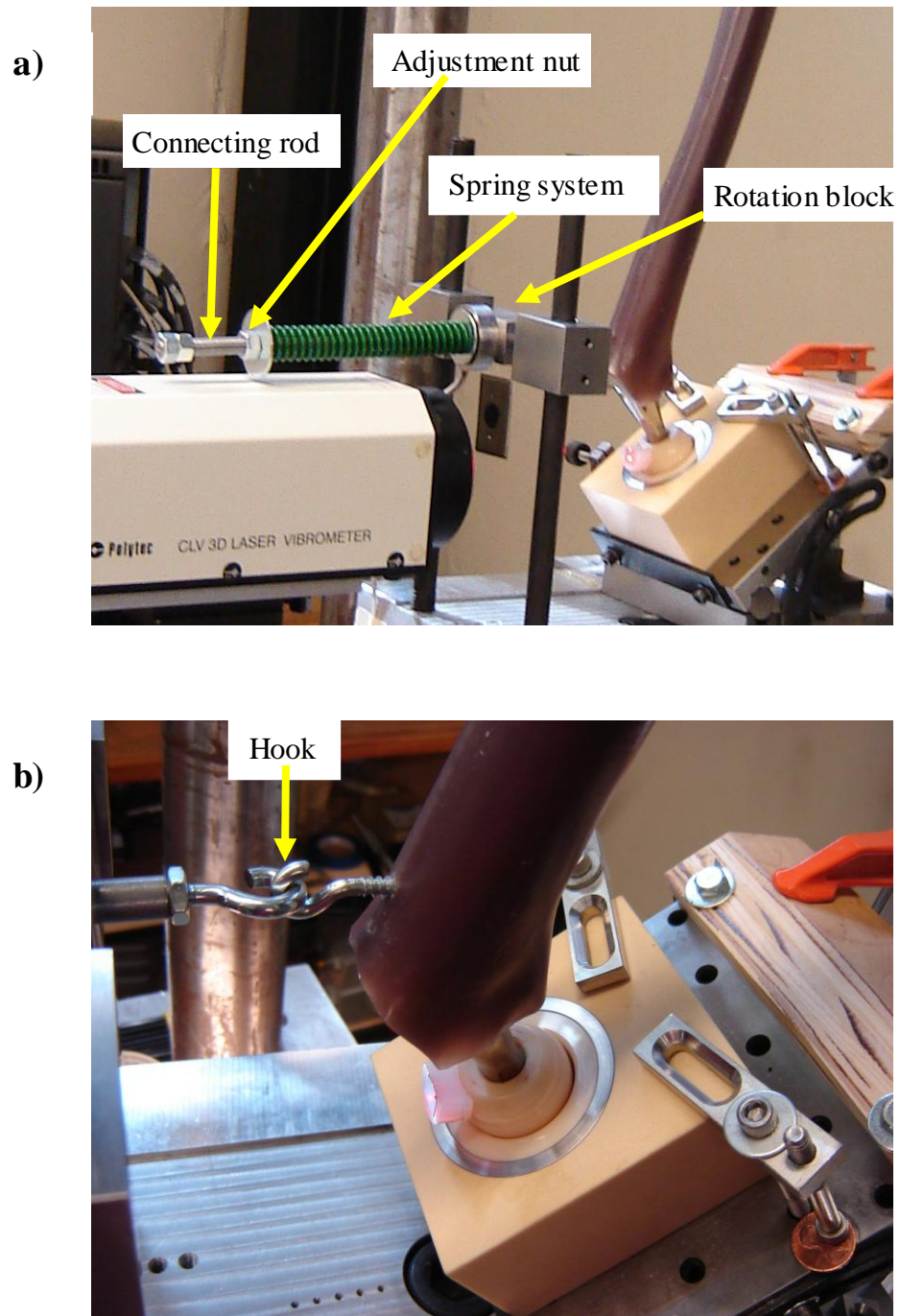


**Figure 24:** a) Compression spring system connected to the femur by means of a b) hook

#### 4.5 Laser Vibrometer

The velocity of the femoral head during reduction into the acetabular liner was measured using a laser Doppler vibrometer (CLV-3D, Polytec, Germany). The laser head of the vibrometer was supported on a tripod equipped with a 3D rotation head. The laser was focused on a small piece of retro-reflective tape stuck on the femoral head as shown in Figure 25. The focus was adjusted by manually moving the tripod until the vibrometer's three lasers converged at a single spot, approximately  $\text{Ø}0.5$  mm. Although the vibrometer could measure three orthogonal components of velocity at the focus point, only the component parallel to the laser head (the Z component per the vibrometer's terminology), was recorded, since that component was by far the greatest, as effected by the experimental design. The vibrometer provided a dynamic voltage output that was later scaled to a velocity signal using the system's calibration factor.

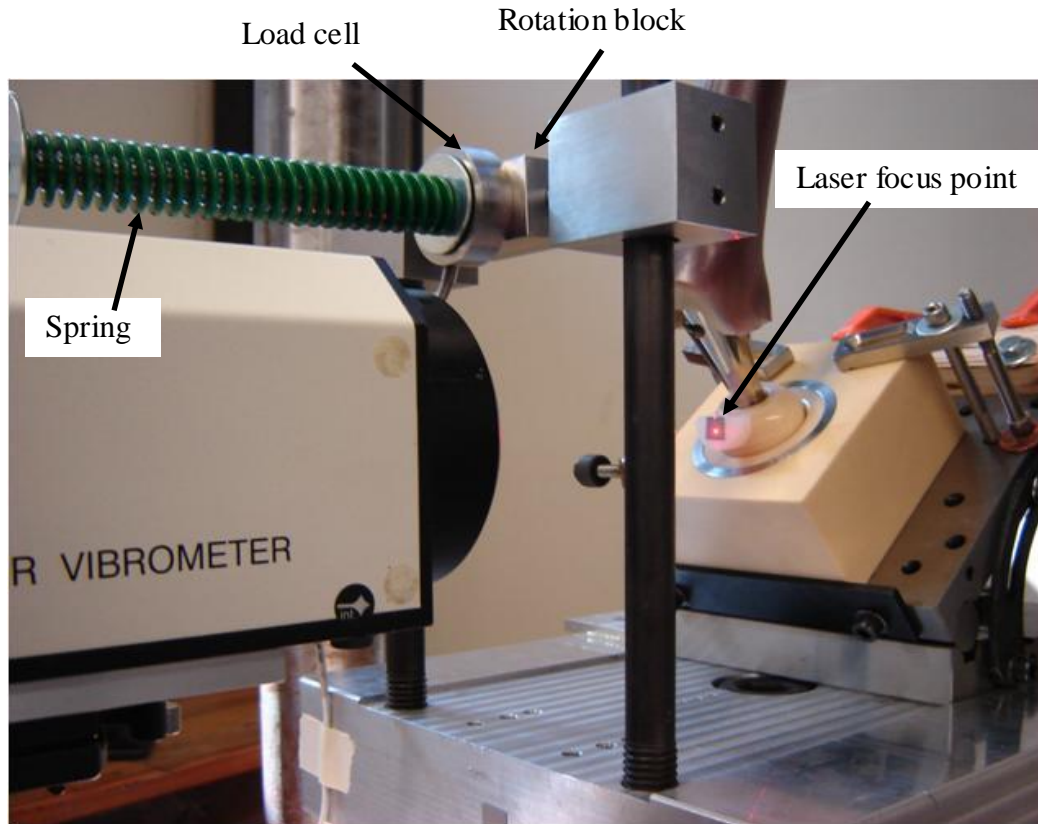
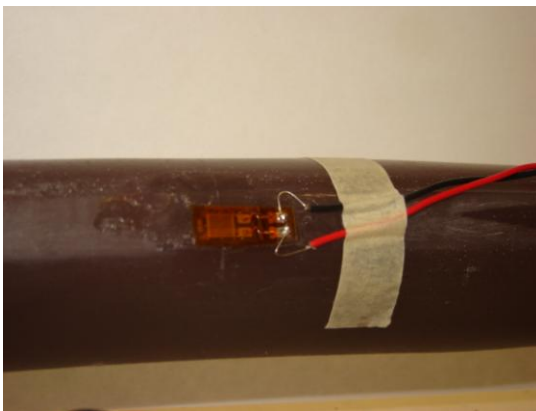
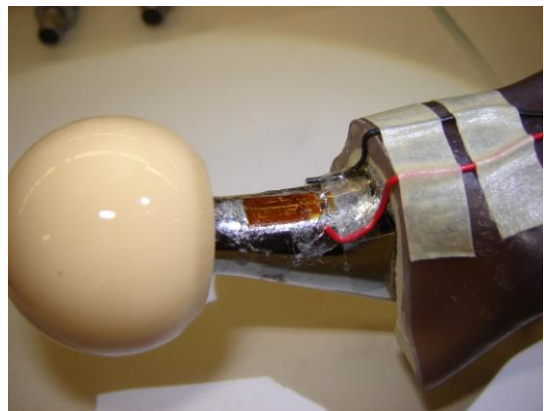


**Figure 25:** Components of the spring system (spring in green, load cell and rotation block) and laser focus point (red spot) from the vibrometer focused on the femoral head to measure the velocity



**a)**



**b)**

**Figure 26:** Strain gages installed on a) the femur and b) the femoral neck

## 4.6 Strain Gaging

Two foil strain gages were used to measure dynamic strain response in the femur construct during the sudden reduction tests. One was installed on the medial femoral diaphysis; this location was selected for maximal signal strength, since the location would experience maximal strains from combined compressive axial and bending loads. The other gage was installed on the medial side of the femoral neck; this location would also experience combined axial and bending loads, though lower strain magnitudes due to the stiffer substrate (titanium stem). The installed strain gages are pictured in Figure 26. For each gage, a corresponding dummy gage was installed on a dummy specimen of the same material to compensate for temperature effects when the gages were connected into a Wheatstone bridge circuit. High resistance 1000  $\Omega$  gages were selected since the synthetic femur was a poor heat-sink material. A high bandwidth signal conditioning amplifier (2310B, Vishay Micro-Measurements, Raleigh, NC) completed the bridge circuits. The amplifier was used with relatively low gain settings (e.g. <1000) to maximize the bandwidth and minimize potential attenuation of rapidly changing dynamic strain signals. The amplifier settings were calibrated using on-board shunt calibration. The strain measurements in the two locations were made in separate trials under identical input conditions, since only one such amplifier was available.

## 4.7 Data Acquisition

The strain and velocity signals were acquired and digitized using a high-speed, USB-based data acquisition board (USB 1604HS, Measurement Computing, Norton, MA). The signals were simultaneously sampled at 250 kHz. Sampling was triggered at a specified voltage on the rising slope of the velocity signal, and the board's pre-trigger sampling

capability was used to capture the signals over a short duration preceding the trigger event. The board was programmed using LabVIEW and the ULX<sup>TM</sup> library of virtual instruments (VI's) supplied with the board.

## **4.8 Experimental Procedures**

### **4.8.1 Input velocity**

The input to the model was a step displacement applied by the hydraulic actuator to the base plate and acetabular sub-assembly. However, since no real system can supply an instantaneous displacement, and since it was vital to know the input accurately for subsequent use in the finite element analysis, the actual input was carefully measured. First, the MTS controller was tuned. The system was set to run a displacement square wave of an appropriate magnitude (1 mm), and the displacement signal was monitored with an oscilloscope. The controller's PID settings were then adjusted to maximize the displacement rate without causing overshoot. In this and in the experiments, the MTS actuator's LVDT displacement sensor was scaled into a short range of  $\pm 10$  mm to improve its accuracy in the short displacement scenario of these tests.

After controller tuning, the BMR model was assembled in entirety as if for an actual experiment trial. The experimental procedure (as described below) was performed, but instead of recording femoral head velocity, the velocity of the base plate was measured with the laser vibrometer. A reduction trial was performed with the same displacement used in the actual reduction experiment, and the base-plate velocity was recorded with a digital oscilloscope. The actual loading during heel strike as per ISO standard is downward [1]. As the experimental BMR model is in an anatomically inverted

orientation (as described in Chapter CHAPTER 2), the velocity input in the BMR model used to simulate the loading during heel strike phase is vertically up. This dynamic velocity record was applied subsequently as the input to the finite element simulation of the BMR model, as described in Chapter 5.

#### 4.8.2 Reduction trials

The experiments were designed to have initial polar separation gap (*PSG*, Figure 7) values of 2, 3, and 4 mm in separate trials. Since these PSG dimensions could not be measured directly, the set-up conditions to establish them were determined by a partly trial-and-error, partly deductive process. First, the entire BMR model was set up such that the femoral head was fully reduced in the acetabular liner. This was after lubricating the bearings with a few drops of a bovine serum solution (serum with 30 mg/L protein content from Thermo Fisher Scientific, Logan, UT, diluted 50% with de-ionized water). The horizontal distance ( $x$ ) of the femoral head relative to the edge of the acetabular block was measured using gauge blocks (arrangement shown in Figure 27). Then, the actuator (and entire pelvic sub-assembly) was lowered by an initial trial distance ( $y$ ) such as 0.8 mm, whereupon the femur could rotate slightly to create edge contact (between head and liner), accompanied by a reduction in  $x$ . The trial distance  $y$  is termed as *drop distance* because the actuator was lowered (dropped) by that distance. Then, applying the 105 N lateral spring force reduced  $x$  by a further small amount (e.g. 0.1 mm) due to compliance in the assembly. An accurately dimensioned 2D CAD model of the femoral construct, head, and liner was previously constructed, and from this, it was estimated that certain values of  $x$  would correspond with the desired PSG values. Therefore, the actuator was then lowered further from the trial distance  $y$  until the measured distance  $x$  (again

measured with gauge blocks) diminished to the value obtained from the CAD model. The result was called the “*actuator drop distance*”, and this set-up parameter was used to position the femoral head relative to the acetabular liner in the reduction trials. This procedure was repeated for each PSG value.

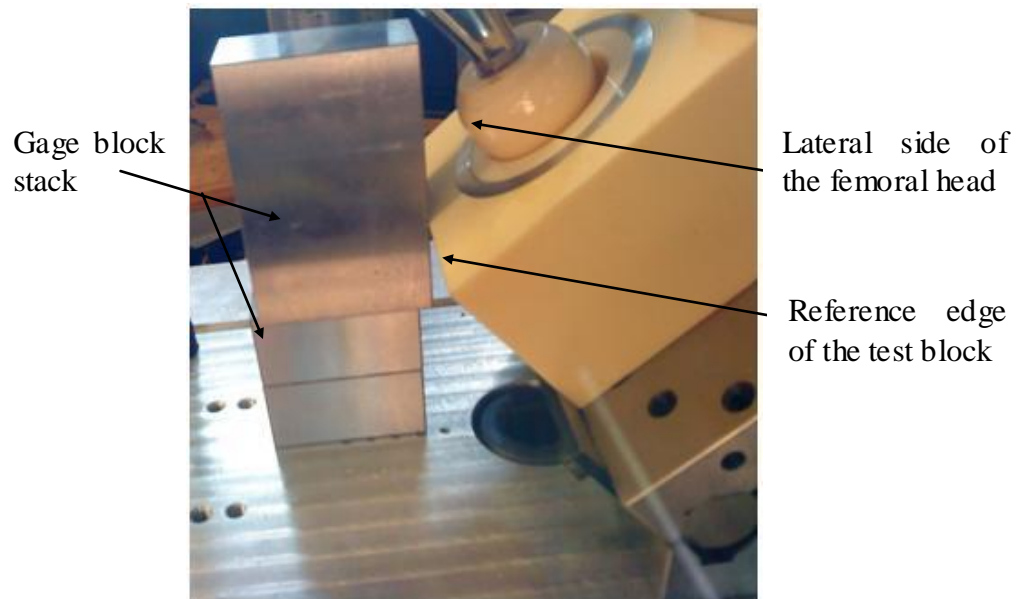


**Figure 27:** Arrangement of gage blocks to measure the horizontal displacement of the femoral head

To set up a reduction trial, the femoral and pelvic sub-assemblies were lubricated with the serum solution and positioned with the head fully reduced. Then, the actuator was lowered by the required drop distance. One of the strain gages was connected with the amplifier, and the bridge output was zeroed. Then, the 105N lateral spring force was applied. The laser head of the vibrometer was moved into position, leveled, and focused onto the retro-reflective tape on the femoral head. Then, the trial was performed by delivering a step displacement with the MTS actuator. The magnitude of the step displacement was slightly less (by 0.05 mm) than the drop distance; this was a precaution to avoid a potentially destructive crash between the femoral head and acetabular liner. At

least three trials were performed for each PSG value. Trials were then repeated to acquire measurements from the other strain gage.

## CHAPTER 5

### FINITE ELEMENT ANALYSIS OF BMR MODEL<sup>4</sup>

#### 5.1 Introduction

This chapter describes the finite-element analysis (FEA) of the BMR model and an aggressive submodeling technique used to quantify the contact force and stresses in the COC hip implants during sudden reduction. Using the Abaqus finite-element code [50], the solution strategy was divided into two key steps. First, the entire model was analyzed under inputs matching those recorded in one reduction trial; this step was called the *global model* analysis. Second, the model was partitioned to remove the majority of its geometry, other than small portions of the head and liner immediately surrounding the edge-loading contact point, and then this smaller model was analyzed with a refined mesh; this step was called the *submodel* analysis. The experimentally measured response parameters (femoral head velocity and femur strains) were used to validate the global model. The submodel analysis provided key required outputs, namely contact force and contact stresses that could not be measured directly in the experiment.

Although the experimental BMR model was tested in an inverted anatomic orientation (with the pelvic sub-assembly beneath the femoral sub-assembly), the FEA was performed on a BMR model oriented in an anatomically upright orientation. This

---

<sup>4</sup> The Abaqus analyses described in this chapter were performed by contractor Exponent, Inc., under our supervision.

approach facilitated model and results interpretation and communication. The orientation and anatomic descriptions in this chapter are in accordance with the upright orientation.

## 5.2 Three Dimensional Solid Model and Mesh Generation

Three dimensional CAD solid models of each component of the BMR assembly provided the geometry needed for the FEA. A CAD model of the 4GCF was acquired from its manufacturer. According to the manufacturer, the CAD model was based on data obtained from computerized tomography (CT) scans of a sample 4GCF. The femoral stem's CAD model was obtained from the manufacturer. The femoral head CAD model was built in SolidWorks using dimensions from its manufacturing drawings. The acetabular liner CAD model was built in Pro/Engineer (Pro/E) using dimensions from two sources. The contour of the spherical bearing surface (the *ID*) and the adjacent edge were digitized in 0.1 mm increments using a scanning touch probe CMM (Contoura, Zeiss, Germany). The 2D coordinate data points were merged in Pro/E with 2D sketch entities representing the liner's face and all its exterior features, and the resulting sketch was revolved to form an axisymmetric 3D model. We used measured ID and edge dimensions rather than nominal manufacturing drawing dimensions, because prior observations showed that actual dimensions, particularly near to the edge, could vary substantially from the nominal ones. Moreover, the edge contour would expectedly play a significant role in the edge-load forces and stresses during sudden reduction; so, accurate CAD model dimensions were vital. The acetabular shell was a simple Ø62 mm hemispherical shell with an internal Morse taper exactly matching that of the liner; its CAD model was created in Pro/E. The test block's CAD model was also built in Pro/E, and its Ø62 mm hemispherical bore was sized to exactly match the shell's outer diameter.

To create the virtual BMR model assembly, the CAD models were imported into Hypermesh (Altair Engineering, Troy, MI) and assembled as dictated by their mating surfaces, except that positioning the stem relative to the femur required extra steps. An initial measurement of the experimental femur construct provided data for a trial position in the Hypermesh assembly. This measurement was performed using a CMM, and it provided two data sets needed for the virtual assembly: (1) the position and the orientation of the distal pin relative to the femur and the CMM's reference frame, and (2) the position of the head relative to the pin and the reference frame. A detailed description of the CMM measurement scheme is given in Appendix B. The CMM measurement results were replicated in the virtual Hypermesh assembly of femur and stem. However, the initial virtual assembly showed that the stem interfered slightly with the femur, so it was judged that the CMM measurements did not position the stem relative to the femur accurately enough. Therefore, A/P and M/L radiographs of the femur construct were obtained. These were then used as visual guides while the stem was adjusted in the assembly to match its appearance (i.e. its position relative to the femur) in the radiographs. Where the stem geometry still interfered with the femur geometry, such as in the femur's intramedullary cancellous bone volume, the femur geometry was eliminated by Boolean subtraction (left side of Figure 30). The femoral and pelvic sub-assemblies were then positioned with respect to each other as described in Chapter 2.

The meshes generated for all the components of the virtual BMR model are shown in Figure 28-32. Each component was individually meshed using Hypermesh. Due to their complicated shapes, the stem and femur were meshed using 10-node linear tetrahedral elements (called C3D10M in Abaqus) generated by Hypermesh's automatic

mesh generator. To represent a press-fit, the interface between the stem and femur meshes was constrained using surface-to-surface constraints, which imposed a restriction that the two components could not slide relative to one another. The surfaces of the femur and the femoral stem were more densely meshed than the inner cores of these components as shown on the right side of Figure 30. This was done to reduce the computation time, and it was judged that this strategy would not affect the principal response parameters such as the strains on the femur construct and the stresses at the edge loading contact. The femoral head and the acetabular liner were meshed mainly with 8-node linear hexahedral elements (called C3D8R in Abaqus) in a rotational sweep. Both of these components had a locally refined mesh with an element edge length of approximately 0.1 mm near the edge load contact point (as shown in Figure 31) and, the largest element size away from the contact point was 2.6 mm for the femoral head and 3.6 mm for the liner. The acetabular shell and the test block were meshed with mainly tetrahedral elements. As with the femur-stem assembly, all of the other press-fit mating interfaces were modeled with surface-to-surface constraints. The head-liner contact interface, on the other hand, allowed friction, as described below. The meshes were exported from Hypermesh and imported into Abaqus for the computational analysis.

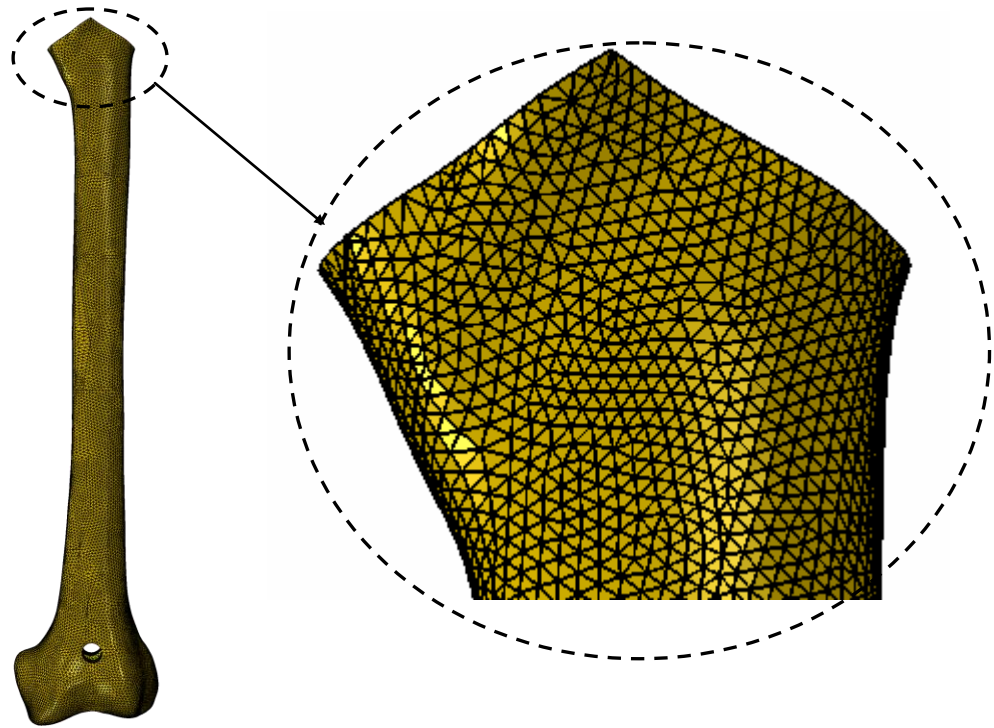


**Figure 28:** Mesh of the femur (left) and zoomed-in view (right) showing the tetrahedral mesh density

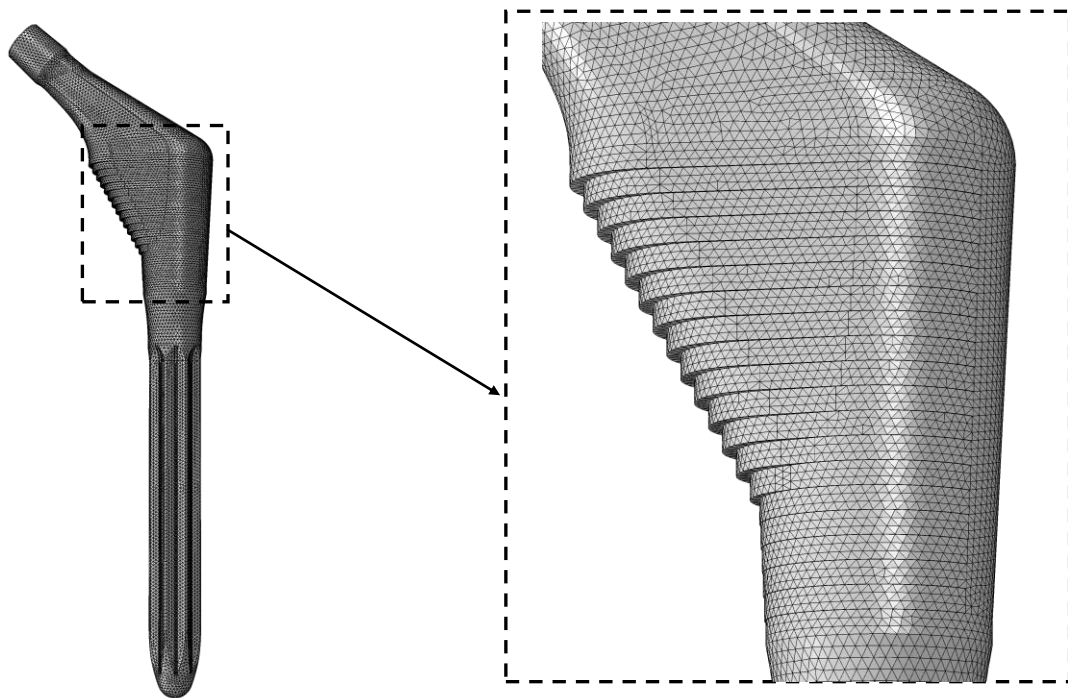


**Figure 29:** Mesh of the femoral stem (left) and zoomed-in view (right) showing the tetrahedral mesh density

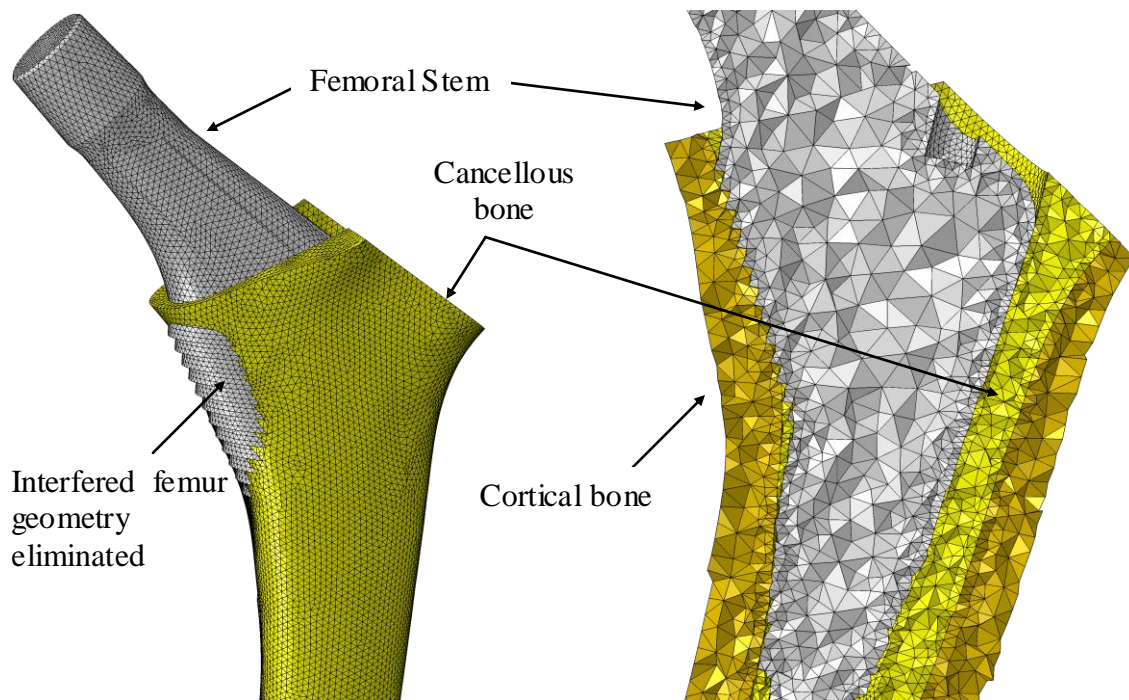


**Figure 30:** Femoral stem and cancellous bone assembly (left) showing the penetration of the stem mesh into the cancellous mesh; (right) Section view of assembly of femoral stem, cancellous and cortical bones showing the inner core mesh density

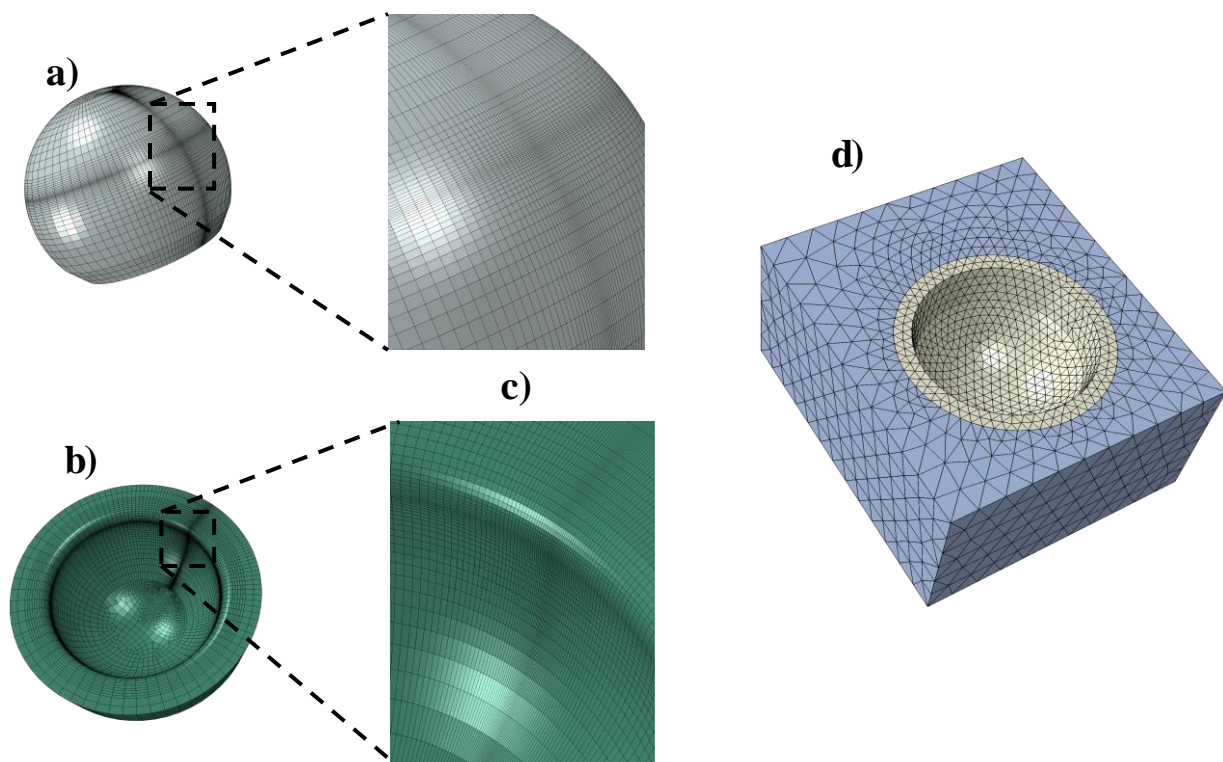


**Figure 31:** Locally refined hexahedral meshes of a) femoral head, b) acetabular liner; c) Zoomed in views of the local refinement; d) Tetrahedral mesh of the acetabular shell and the test block

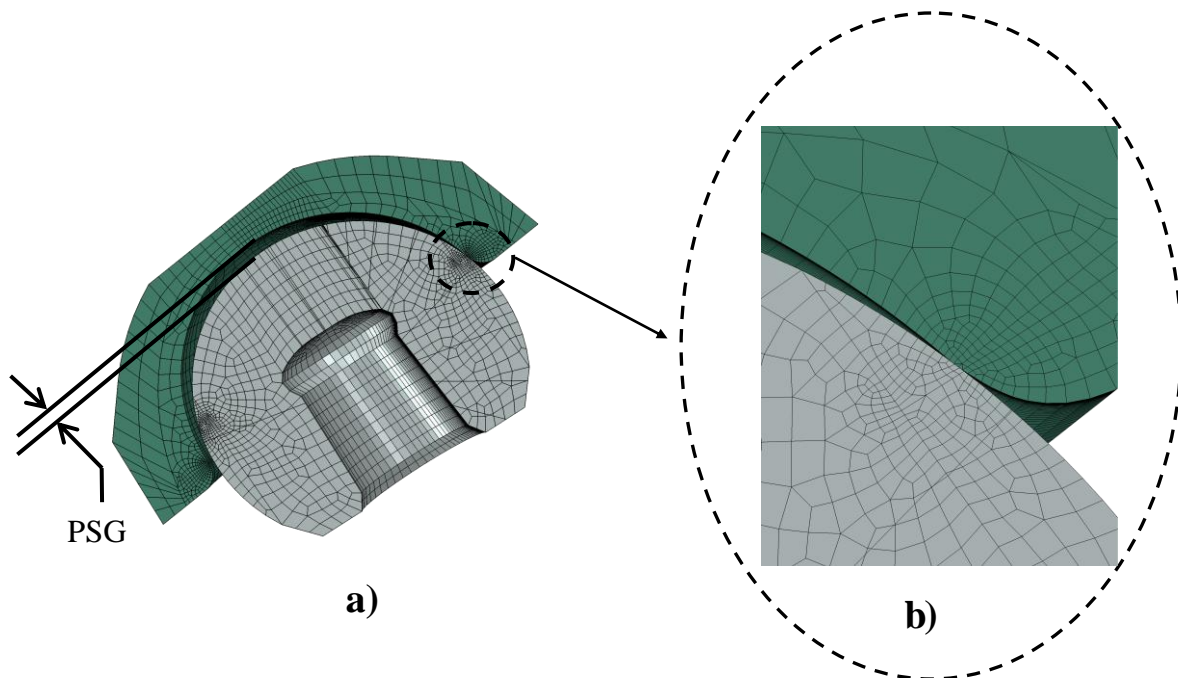


**Figure 32:** a) Section view of femoral head and acetabular liner meshes and the PSG; b) Detail view showing a locally refined mesh at the contact

### 5.3 Material Properties

All of the material properties were modeled as linear elastic, with values per Table 7, except for those of the femoral cortex. The femoral cortex was also modeled as a linear elastic material, but the appearance of error in initial model results (judged by comparison with experimental results), and a review of composite femur property data in relevant scientific literature [51], suggested that the manufacturer-provided properties could be inaccurate. Therefore a separate experimental trial was performed to calibrate the femoral cortex properties. A second strain gage was installed on the femur's medial diaphysis, immediately below the first gage and oriented perpendicular to it (Figure 33). The femur construct was suspended vertically by the U-bracket from the load cell of a separate test frame. The test frame and femur were set up to compress the femur axially, with the femoral head contacting a hardened steel compression platen. The femoral head was positioned underneath and concentric to the load cell. The head was constrained from

sliding by steel blocks clamped to the compression platen, and the platen near the head was greased to minimize friction. Then, the test frame crosshead was lowered at a constant rate of 0.36 in./min. to a total displacement of 0.03 in. while the strain in one gage was recorded simultaneously with the load. A second, identically configured trial was performed to record the strain in the transverse gage, though only after an approximately 45 minute delay, since the femur exhibited viscoelastic relaxation characteristics, as evidenced by a residual, slowly decreasing strain observed in the initially measured gage.

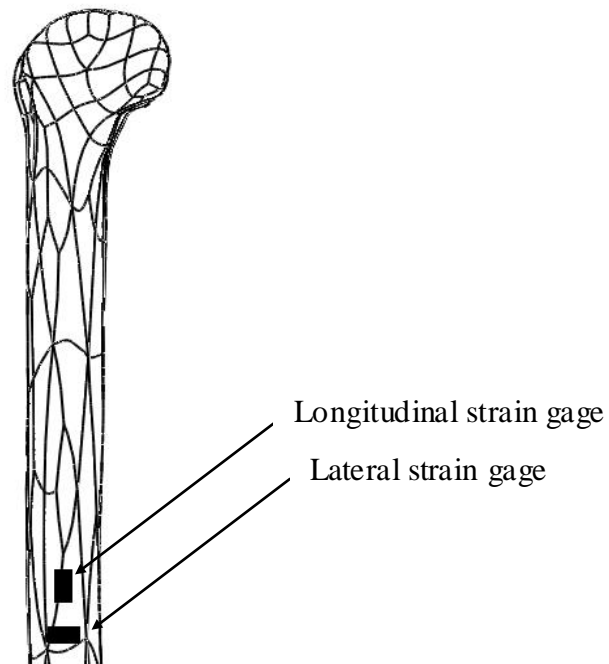


**Figure 33:** Two strain gages installed on the femur's medial diaphysis. One strain gage measured longitudinal strain and the other measured lateral strain

The load measured in this trial was applied as input in a quasi-static finite element analysis of the femoral construct constrained and loaded to mimic the trial. When the model was analyzed using the manufacturer-supplied femoral cortex properties, the strains from the FEA did not match those from the trial, as shown in Figure 34. So, the

model's material properties were scaled and the analysis was re-run. The results from this second analysis showed close agreement between measured and predicted strains (Figure 34), which validated the adjusted values of the femur's elastic properties. The elastic modulus of 13.25 GPa and the Poisson's ratio of 0.41 determined in this calibration process were used in all subsequent BMR model analyses.

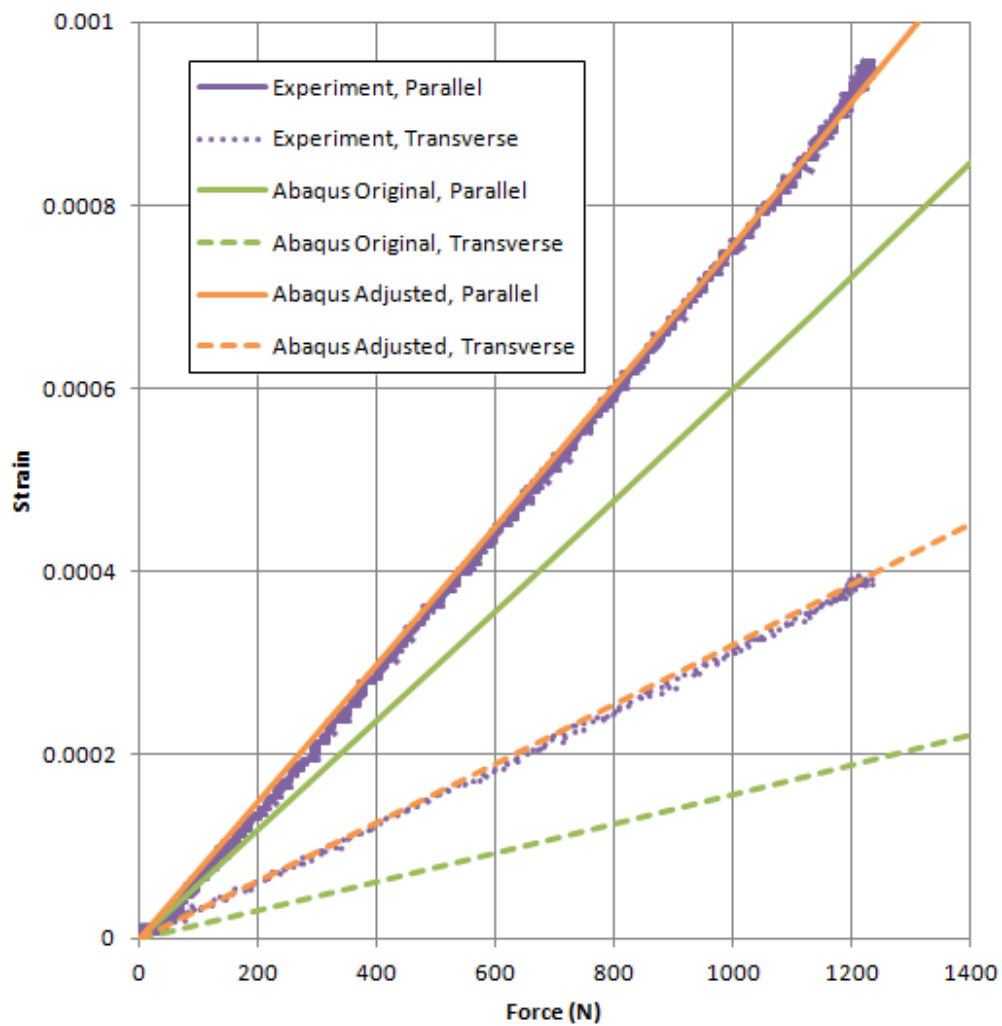


**Figure 34:** Longitudinal (Parallel) strain and Lateral (Transverse) strain vs. force using the original and the adjusted material properties; the strains obtained using adjusted material properties match with the experimentally obtained strains.

The use of a linear-elastic material model for the femoral cortex, despite the viscoelastic behavior observed in this slow-loading trial, was a simplifying assumption. The simplification was initially rationalized on the basis of its common use in prior FEA studies involving composite femurs [51]. As described in further detail in the Discussion chapter, the retrospective justification for using assuming elasticity in the fast-loading study is simply that dynamic loading corresponds to a large Deborah number, for which material response is essentially elastic.

#### **5.4 Loading and Boundary Conditions**

The boundary conditions (BCs) employed in the FEA of the BMR model represented the BCs described in Chapter 2. The femur's distal pin axis was represented by a cylindrical hole passing through the distal femur in the same location as the physical distal pin. The nodes on the surface of this hole were constrained to only rotate about an axis coaxial to the hole. Otherwise, the pin itself was not modeled as a distinct 3D entity in the FE model. Realistic compliance at the pin axis was modeled by implementing horizontal and vertical linear spring elements with spring constants matching the effective fixture stiffness values measured as described in Section 4.3. The proximal surface of the pelvic test block was constrained to translate only in the vertical direction. A tensile spring element with a spring constant of 8.88 N/mm was incorporated into the FEA to represent the experiment's lateral spring. Though the experiment used a compression spring, the spring mechanism transformed its compression into a force that pulled laterally on the femur, thus the use of a tensile spring element in the FEA. The spring constant was determined by direct force-displacement calibration of the

experimental spring, using a separate test machine. The loading and BCs applied in the FE version of the BMR model are illustrated in Figure 35.

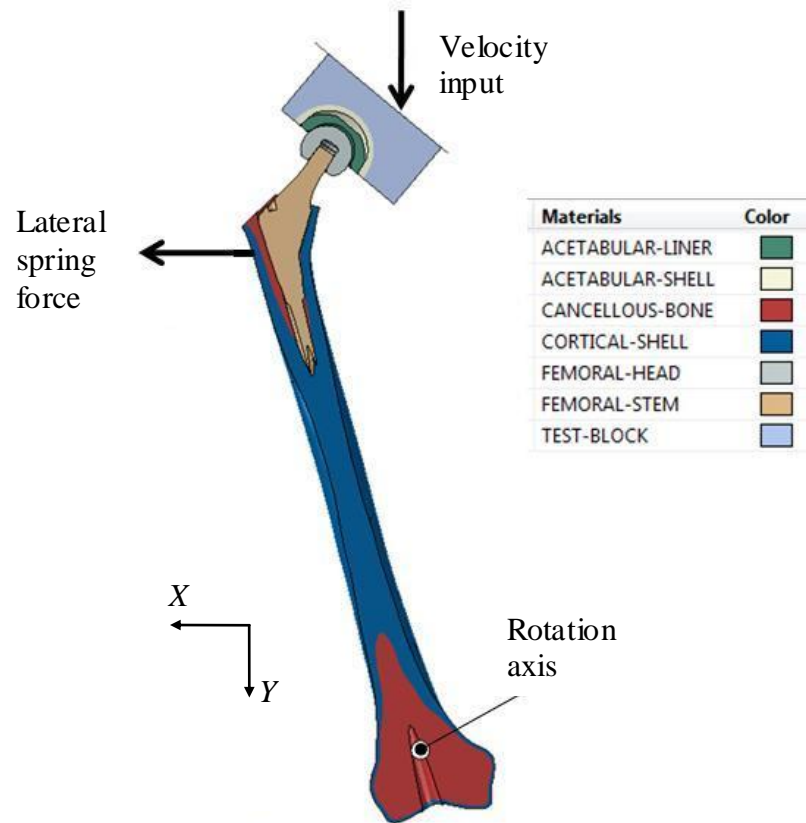


**Figure 35:** Illustration of the loading and the BCs in the FE version of the BMR model (shown in section view)

To commence the global model analysis, the pelvic sub-assembly was raised vertically to mimic the drop distance applied in the experiment. Then, the load inputs were applied in two steps. The first was a static equilibrium step, in which a static pre-load was applied via the lateral spring element; the solution in this step was obtained using Abaqus' implicit solver (Abaqus/Standard). This step produced a small femoral head displacement that was compared against its corresponding value measured in the experiment. The end of the static step represented a condition of edge loading with the femoral head subluxed, at a time just prior to heel strike and subsequent head reduction. The second load step comprised the dynamic analysis of sudden reduction; the solution in

this step was obtained using Abaqus' explicit solver (Abaqus/Explicit). The dynamic base plate velocity recorded in the reduction experiment was applied as an input across the test block's proximal surface. This input forced the femur to rotate and the head to reduce into the liner, thus creating a simulation of the experiment.

### **5.5 Contact Modeling**

For the static step using Abaqus/Standard, a surface-to-surface contact algorithm was used. A pure master-slave relationship was used, with the femoral head as the master and the acetabular liner as the slave. To enforce contact between the femoral head and the acetabular liner, hard pressure-overclosure behavior with a linear penalty method was chosen. Frictional constraints ( $\mu=0.06$ ) were enforced with a penalty method. For the dynamic step using Abaqus/Explicit, a node-to-surface contact algorithm was used with a balanced master-slave relationship, which completely prohibits material interpenetration.

### **5.6 Submodeling of BMR Model**

Attempting to run a fully or a locally refined global model with explicit time integration is a high runtime consumption process as it involves analyzing a full scale model. To overcome this, an aggressive submodeling approach was performed allowing for fine mesh densities and a greatly reduced model volume, which gives accuracy and computational efficiency. The submodeling technique undertaken in this project is aggressive because the volume of the submodel is less than 1/100<sup>th</sup> of that of the global model. The submodel comprises portions of the components immediately surrounding the contact region as described later in this section.

Elkins et al. [52] used submodeling in the field of orthopedics to analyze the stress concentrations on COC hip bearing couple. That submodel was an annulus (portion of the

acetabular liner) with an element size of 0.3 mm whereas the BMR global model was locally refined with an element size of about 0.1 mm. Cormier et al. analyzed a 2D static contact problem of turbine blades using an aggressive submodeling approach [43]. Submodeling analysis of the BMR model extends the submodeling application to a 3D dynamic contact problem. Elkins et al. [52] employed a conservative submodeling approach in the sense that their submodel size was large in comparison to the contact area; an aggressive, carefully executed, submodeling approach using a smaller submodel volume could have reduced computation costs without adversely affecting accuracy. The BMR model analysis included a submodeling technique in which the submodel is much smaller than the submodel in [52]. This section is dedicated to describing this aggressive submodeling approach undertaken to analyze the BMR model.

### **5.6.1 Submodel Generation**

The BMR submodel, as shown in Figure 36b, was a small region surrounding the contact area (where the edge loading occurred). The submodel was partitioned from the global model components that were members in the contact, namely the femoral head and the acetabular liner. The geometries of the two components were partitioned as a sector with included angles of  $80^\circ$  (labeled in Figure 36c) in an inclined transverse plane and  $20^\circ$  in the frontal plane (labeled in Section A-A of Figure 36c). Then, a thickness of 3.5 mm in each of the components was retained, which is the submodel, and the rest of the geometry was removed.

### **5.6.2 Boundary Conditions**

The BCs on this submodel were enforced by interpolating the displacements taken from the global model at those interfaces where the submodel was partitioned (the “Cuts” in Figure 36c) from the global model. The interpolation was done within Abaqus.

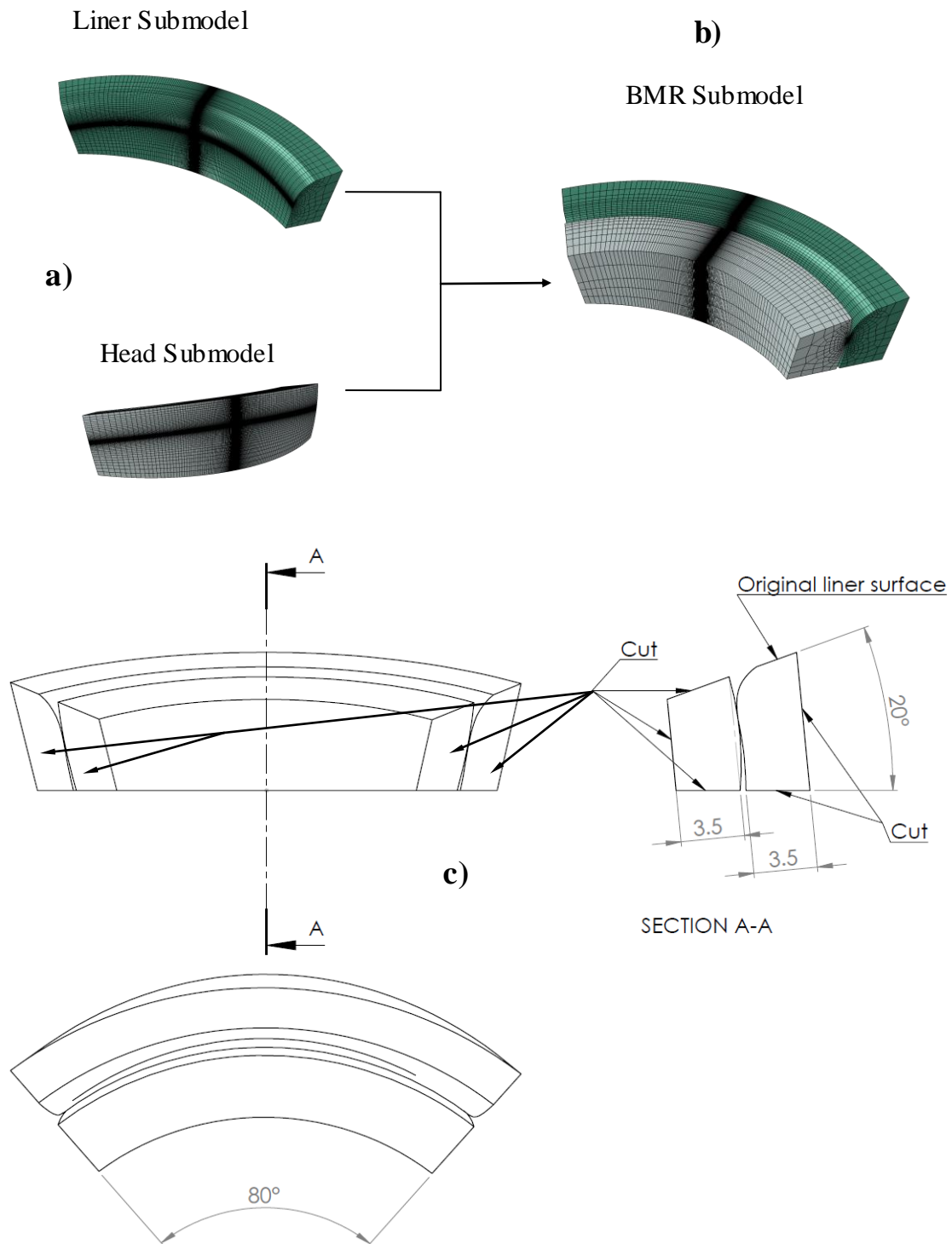


**Figure 36:** a) Meshes of the submodel components, refined at the contact region; b) The BMR submodel; c) Illustration of the submodel generation along with its dimensional details. “Cut” labels indicate where the submodel’s geometry was partitioned from the global model’s geometry (Dimensions are in mm.)

### 5.6.3 Submodeling Analysis Procedure

Submodeling is based on Saint Venant's principle [53], which allows modeling only a portion of an entire structure by applying equivalent loads to the boundary of a sub-body and as long as the BCs on the sub-body roughly approximate the actual tractions on that boundary, the details of the stress fields away from the boundary are modeled accurately. The creation of the BMR submodel geometry (described in Section 5.6.1) is governed by this principle, because an equivalent load system is applied to the submodel geometry as existed in the global model, and the boundary of the submodel is relatively far away from the region of contact. So, the submodel partitions from the global model were made around the contact area at a distance where the stress gradients were negligible. The submodel was meshed with 10-node hexahedral elements, and the mesh was much finer than the global mesh both at the contact and in the region surrounding the contact. The element edge length at the contact was 0.01 mm ( $1/10^{\text{th}}$  of the global mesh element edge length at the contact) for both the femoral head and acetabular liner submodels. The largest element edge length was 1.17 mm in the head portion and 1.15 mm in the liner portion. Then, the displacement BCs were imposed on the submodel and the BMR submodel was solved in Abaqus. Only a single locally refined submodel was analyzed.

This procedure was adapted to analyze the BMR model because (1) it was expected that the contact stresses predicted by the global model analysis would be poorly resolved, since the global model's elements near the contact region were close in size (e.g. 0.1 mm) to the minor dimension (e.g.  $<0.3$  mm) of experimentally observed edge-loading contact patches in COC hip bearings [54] and, (2) the computation time to solve the global model

itself was ~31 hours with a 12-cpu machine (Intel Xeon X5670, 2.93 GHz) with 48 GB memory.

## **CHAPTER 6**

### **RESULTS: TESTING AND ANALYSIS OF BMR MODEL**

The results in this chapter illustrate the rapid structural responses in the femur and the femoral neck and, the contact mechanics of the bearing couples during the sudden femoral head reduction event as analyzed experimentally and computationally.

#### **6.1 Experimental Results**

The experiment was conducted for three PSG values: 2 mm, 3 mm and 4 mm. The following sub-sections give the experimental comparison of different responses of the BMR model for the three PSGs. It was expected that the magnitude of the responses of the model would increase as the PSG increased.

##### **6.1.1 Velocity of the Femoral Head**

The velocity of the femoral head for the 2 mm PSG as measured by a 3D laser vibrometer is given in Figure 37a. The velocity of the femoral head measured for the three PSG values is shown in Figure 37b, which shows that an increase in PSG results in higher magnitude of the peak velocity of (and hence, a higher contact force on) the femoral head. Figure 37b shows a 12 ms time span of data; it encompasses the period of interest, when the head and the liner undergo edge loading.

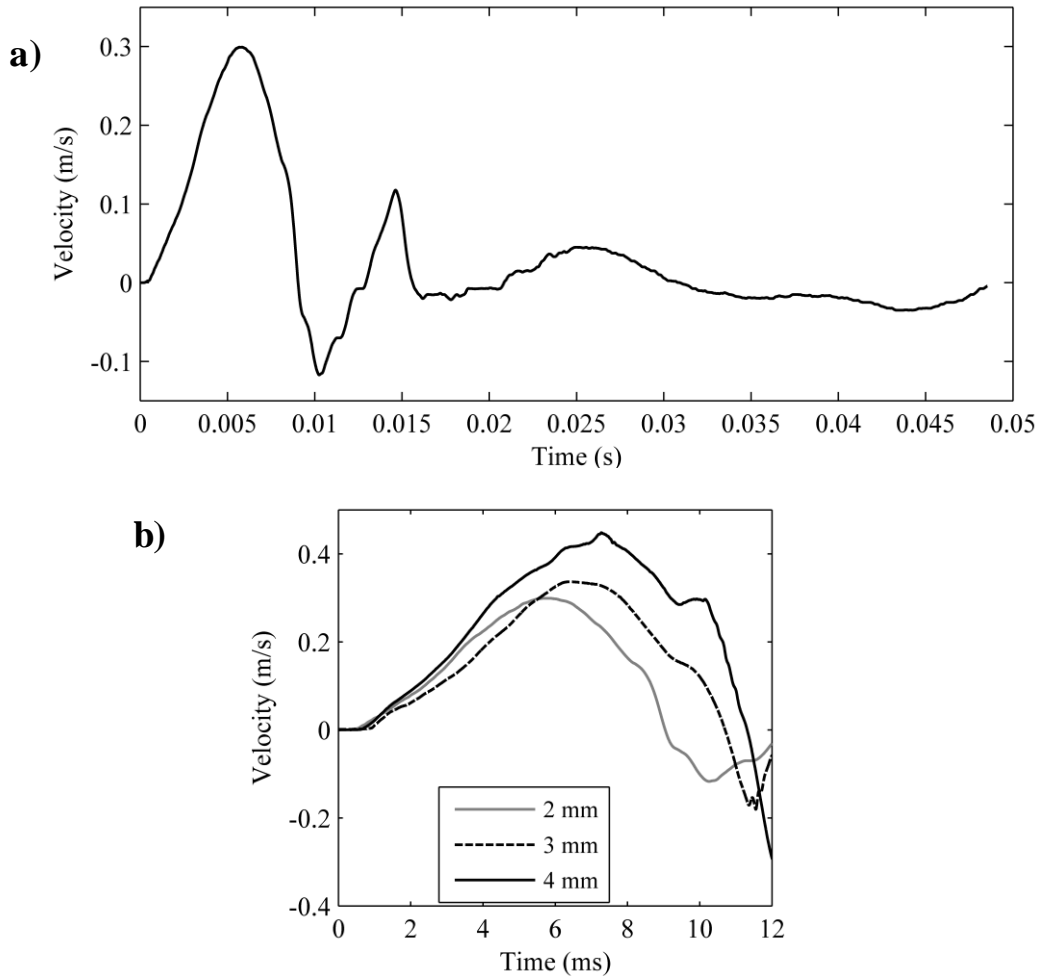


**Figure 37:** a) Velocity response of the femoral head during the 2 mm PSG reduction event;  
 b) Overlay of the velocity of the femoral head for the three PSGs shown for a time span of 12 ms to better show the responses during the reduction event

### 6.1.2 Strain in the Femur and the Femoral Neck

Figure 38 (a and b) shows the measured strain on the compressive side of the components – the medial side of the femur and the medial side of the femoral neck respectively. Figure 38 (c and d) shows a comparison of the strains measured on the femur and the femoral neck respectively, for the three PSGs. The similarity in the initial strain values, for all the PSGs recorded for each of the femur and the femoral neck, results from the use of a consistent spring force value applied in the test's initial static

load phase. As expected, the peak strain became higher as the PSG increased, following the same pattern as for the velocity of the femoral head.

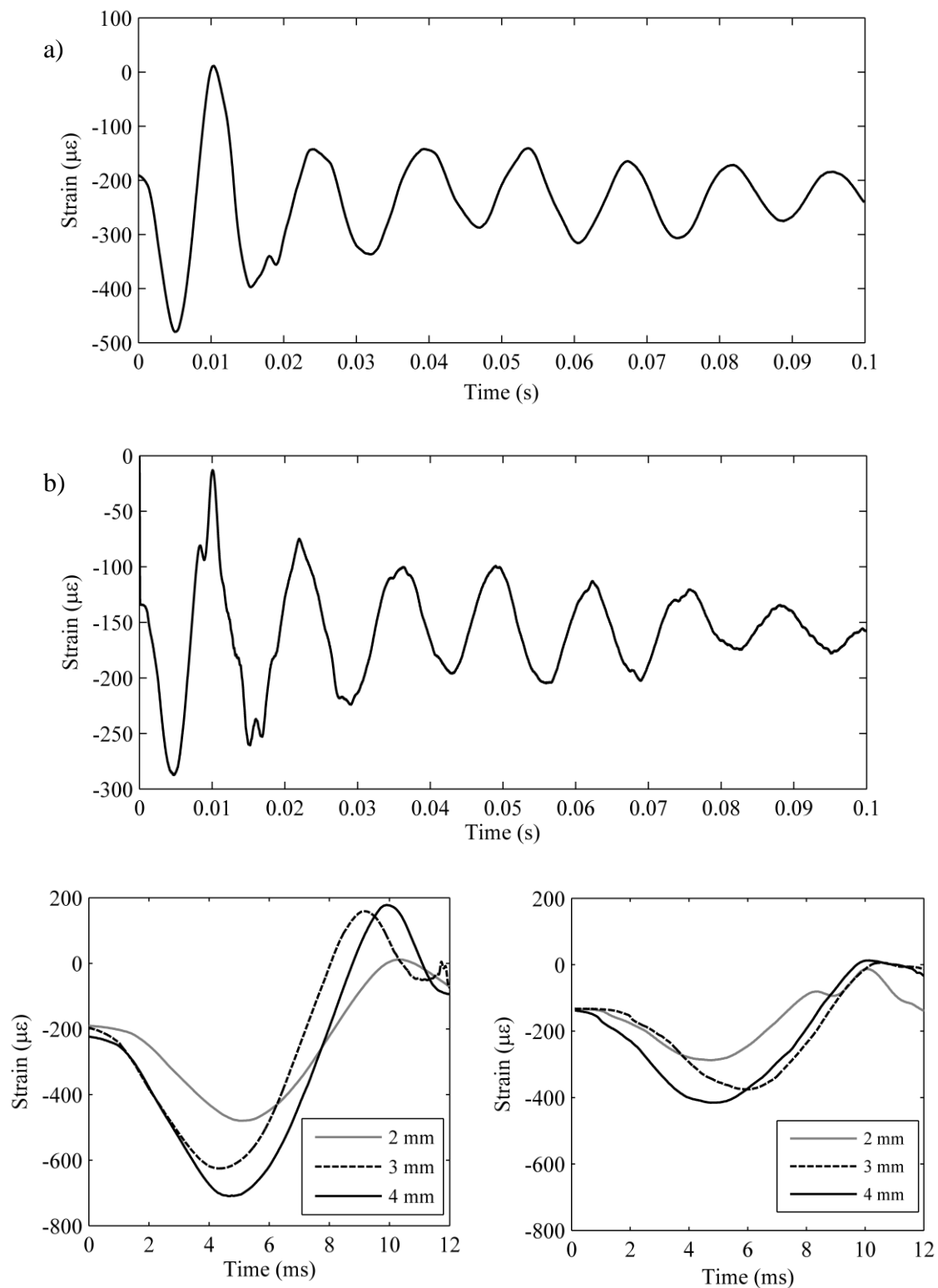


**Figure 38:** Measured strain response for 2 mm PSG in a) the femur, b) the femoral neck over a total span of 0.1s; Overlay of the strain response for the three PSGs in c) the femur and d) the femoral neck over a span of 12ms

## **6.2 Validation of the BMR Model**

The FE version of the BMR model was validated against the experimental version using three response parameters for the 2 mm PSG. The response parameters were (1) velocity of the femoral head during reduction, (2) strain on the femur and, (3) strain on the femoral neck. This section further discusses the validation of the BMR model.

### **6.2.1 Velocity of the Femoral Head**

A time history of velocity was extracted from the FEA simulation at a surface node located on the femoral head in approximately the same location that the laser sensed in the experiment. As shown in Figure 25, the velocity of the femoral head in the experiment was recorded by focusing the laser on approximately the farthest point located on the lateral side of the femoral head after applying the spring force. The FEA data were extracted from the surface node that was on the farthest lateral side of the femoral head at the end of the static load step.

Figure 39a compares the velocity of the femoral head in the FEA and the experiment. The peak velocity of the femoral head in the FEA showed a 25% error when compared against the experimental velocity. Also, the femoral head seemed to be moving at a faster rate during the reduction event when compared to the experiment, resulting in a higher peak velocity. The differences in the peak velocities and the rates at which the femoral head reduced can be attributed to a difference in the friction value at the contact. This is further discussed in the Discussion chapter. Figure 39b shows a focused view of the velocity of the femoral head for a time span of the initial 12 ms. It shows a better view of the velocity for the period of interest i.e., the initial 8 ms during which the femoral head reduction happened. After this time interval, rapid oscillations in the FE

femoral head velocity curve are seen in contrast to the gradual experimental curve. These oscillations can be attributed to the femoral head's bouncing around inside of the liner ID. Also, the FEA did not model the presence of a small amount of lubricant within the liner, which was present in the experiment; that lubricant in the experiment (not modeled in the FEA) might have prevented or damped out such rapid oscillations. In the FEA, it appears that the head collided with the liner ID first at 8 ms into the simulation. In the experiment, no such definitive collision can be discerned, probably because the head actually collided with the fluid within the liner that became pressurized very rapidly, since the clearance of the bearings is very small ( $<60 \mu\text{m}$ ). This explanation is supported by the observation that fluid splashed from the liner onto the components in some experimental trials. Nevertheless, these oscillations are of little concern, since it happens after the period of interest (period of edge-loading) has ended.

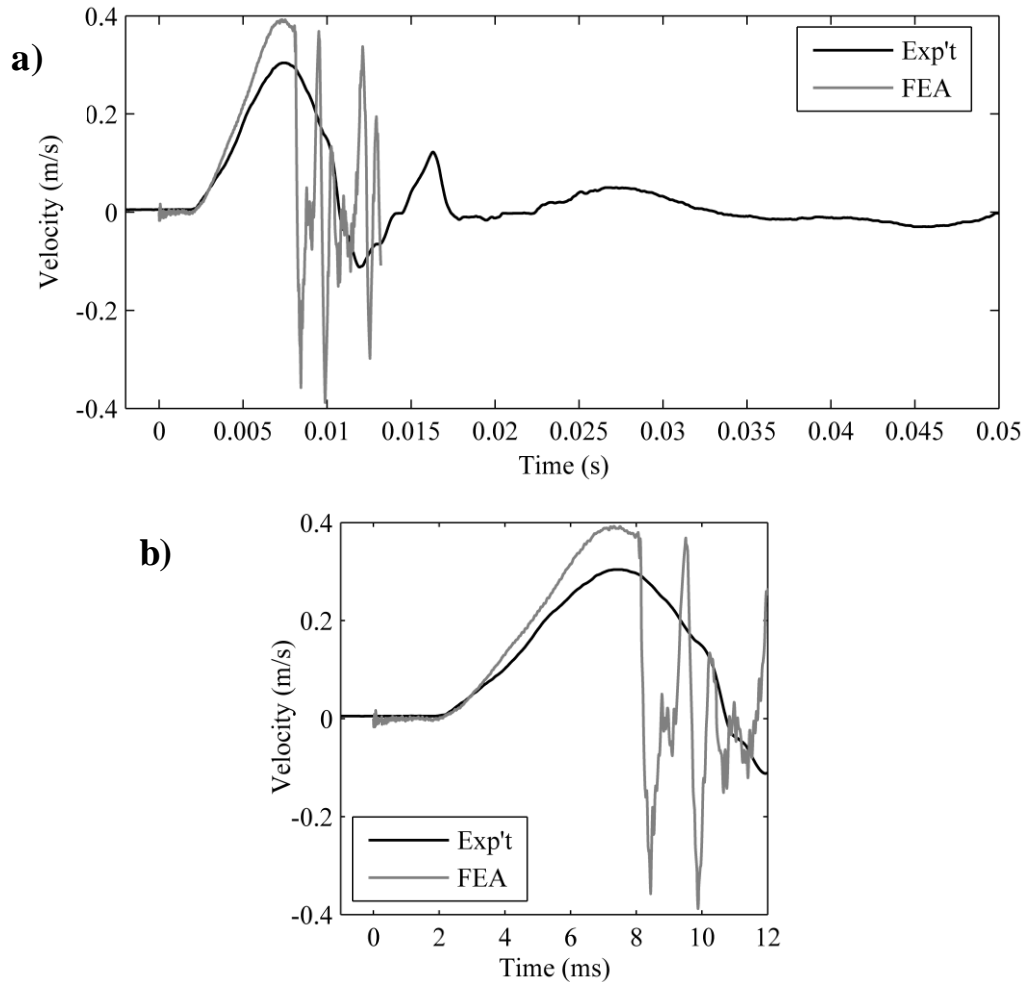


**Figure 39:** Comparison of velocity of the femoral head during the reduction event for 2 mm PSG using FEA and experiment a) for the total time span for which experimental data was collected and, b) focused view for 12 ms

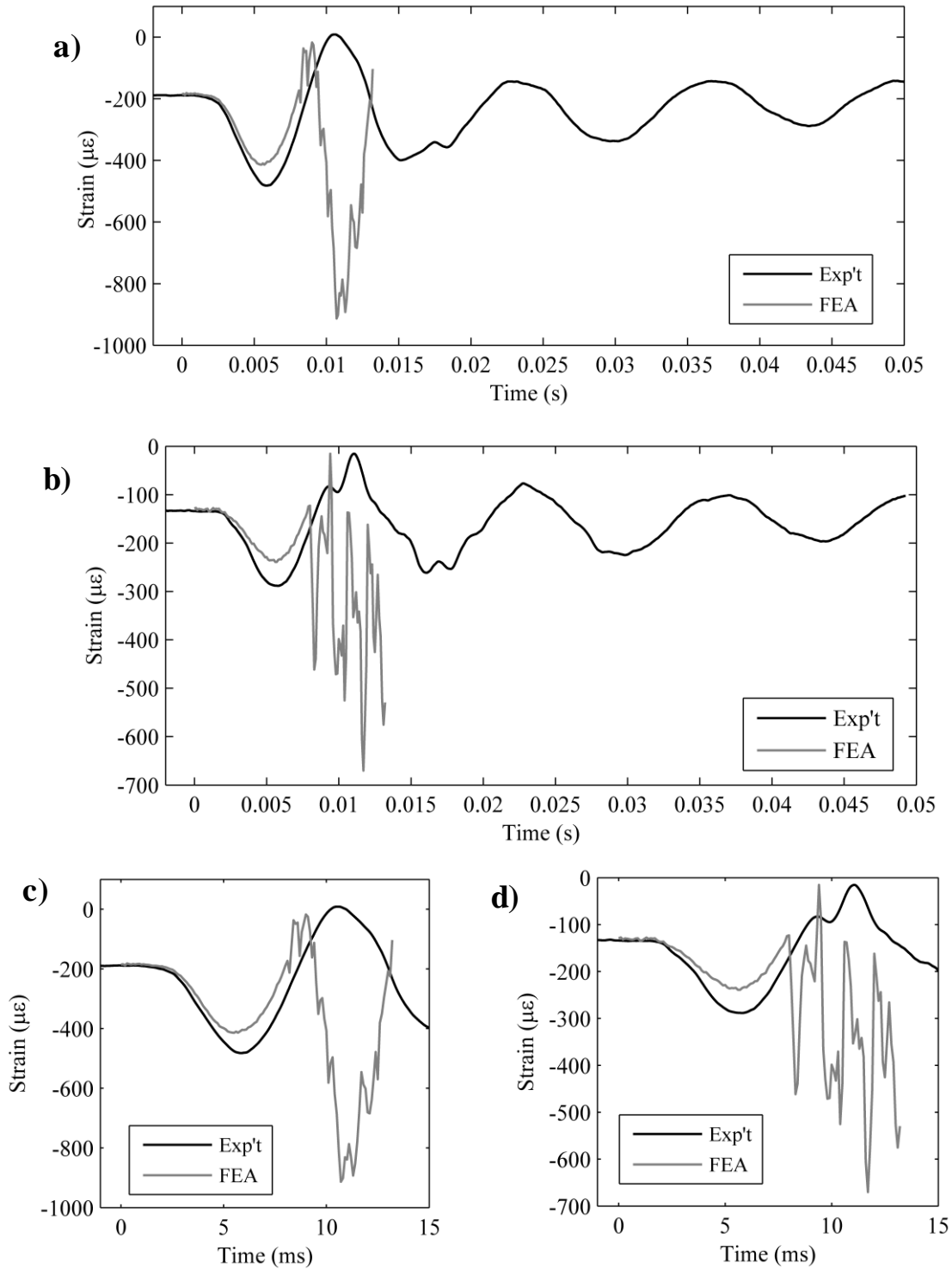
### 6.2.2 Strain in the Femur and the Femoral Neck

Figure 40 (a and b) shows the comparison of the FE and the experimental strains on the femur and the femoral neck, respectively, both for the total time span for which the experimental data were recorded. Initially, the FEA strains show good agreement with the experimental strains though, later during the event, the magnitudes of the FE strain peaks and rates are lower than the magnitudes of experimental peaks and rates, with a 7% error

in the strain on the femur and an 8% error in the strain on the femoral neck. This shows that the femur in the FEA did not bend as far as the femur in the experiment.

Figure 40 (c and d) shows a focused view of the strains of the femur and the femoral neck, respectively, after the initial 8 ms. The curve after ~8 ms has local peaks. These peaks are seen at intervals of the transit time of the stress waves initiated due to an impact of the femoral head on the inside (towards the pole) of the acetabular liner. This interesting phenomenon is further described in the Discussion chapter.

As seen in the velocity plots, similar rapid oscillations are seen for the strain on the femoral neck after the period of interest. Since the period of interest ended before the rapid oscillations occurred, they can be ignored.



**Figure 40:** Comparison of strain for 2 mm PSG from FEA and experiment in a) the femur, b) the femoral neck, both for the total time span for which the experimental data was recorded; focused views of the strain comparison for 12 ms for c) the femur and, d) the femoral neck

### 6.3 Inferred Outputs from Global Model and Submodel Analyses

This section provides the inferred outputs from the FEA of the BMR model (inferred outputs are those which don't have corresponding experimental measurements). FEA was performed for a single PSG (2 mm). Contact force (Figure 41), contact stresses (Figure 42) and, contact areas (Figure 43) for each of the head and the liner are the inferred outputs from the FEA for the 2 mm PSG. Global model and submodel results of these outputs have also been compared against each other and are discussed in brief.

The contact force and the contact area are defined in Abaqus as follows:

*Contact Force:* The contact force is the total normal force due to contact pressure. The Abaqus keyword used to extract the contact force is CFN.

*Contact Area:* The total contact area is defined as the sum of area of all the facets where there is contact force. The Abaqus keyword used here to extract the contact area is CAREA.

The global model and submodel contact force and contact stress plots show a large magnitude of error when compared to each other. Given 25% error in the measured quantities (i.e., velocity and strain as shown in Section 6.2) used to validate the FE model, the global model contact force clearly has considerable uncertainty. Further investigation on the source of error for the velocity of the femoral head has to be done to see the effect of change in velocity on the contact force as described in the Discussion chapter. This error is attributed to using displacement BCs and to simultaneously changing the contact stiffness by altering the mesh density in the submodel. The results might be improved with traction BCs. This source of error is discussed in detail in the Discussion chapter.

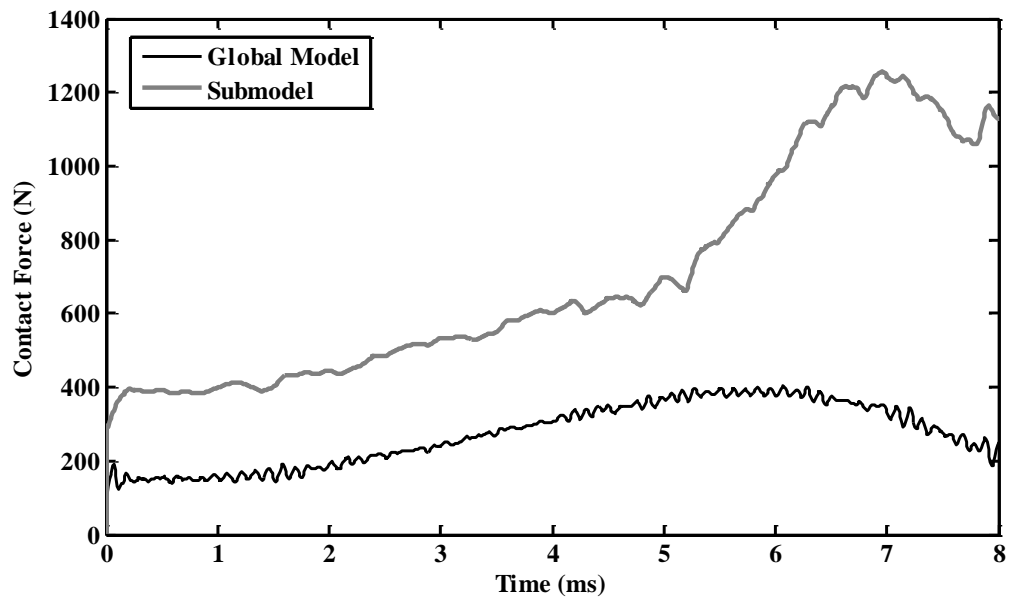


**Figure 41:** Comparison of the global model and the submodel contact force

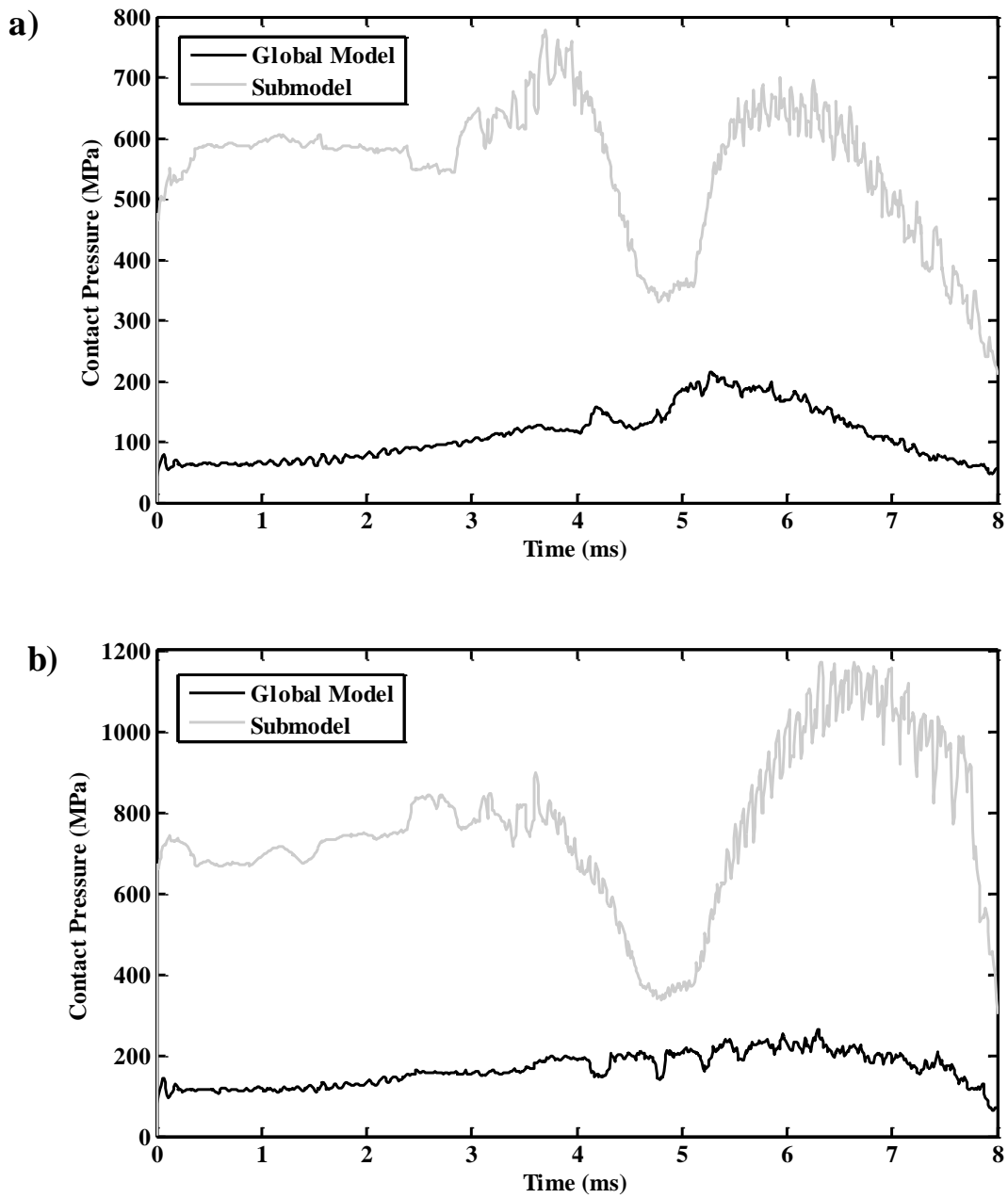


**Figure 42:** Comparison of the global model and the submodel results of contact pressure for a) the femoral head and, b) the acetabular liner

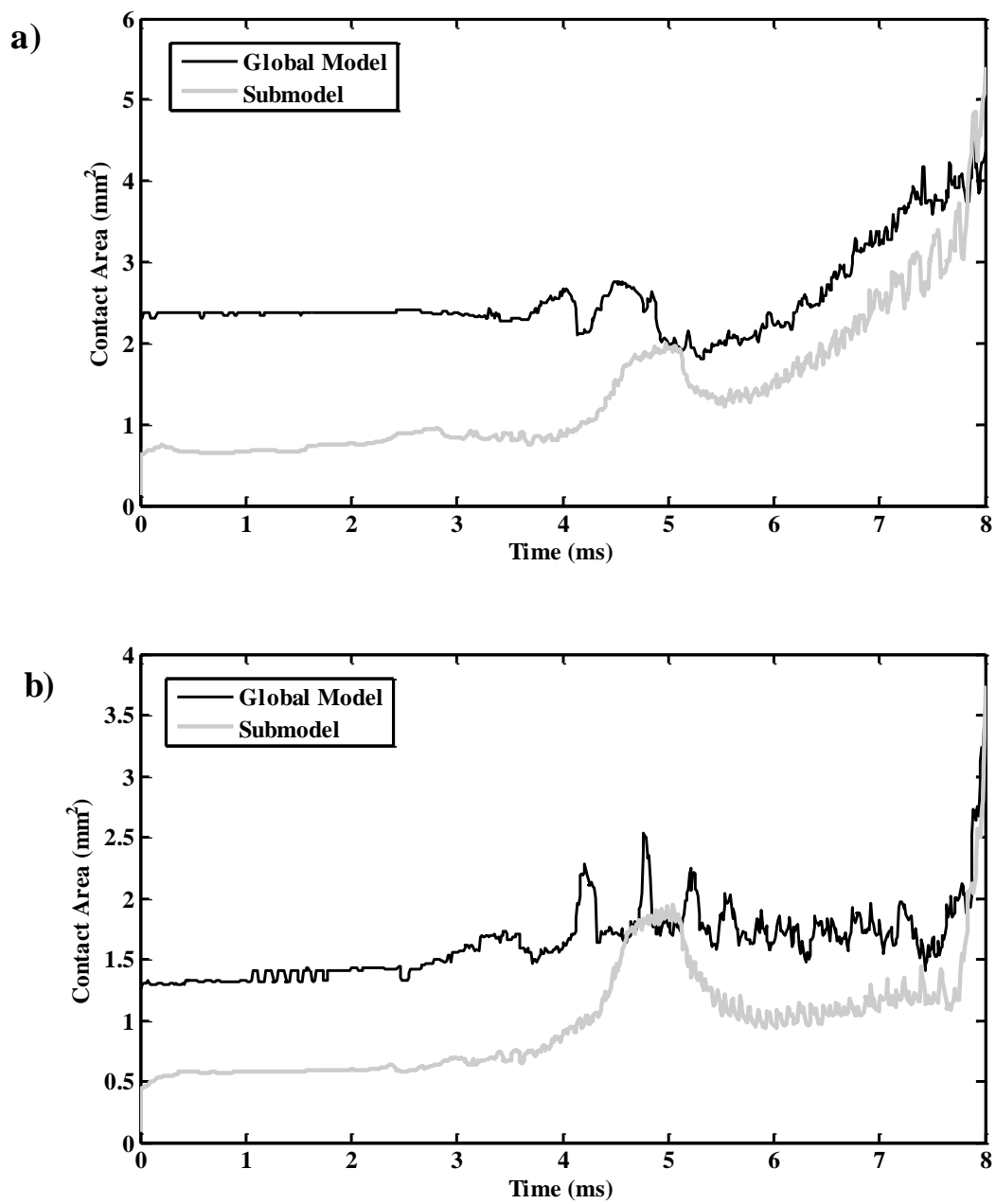
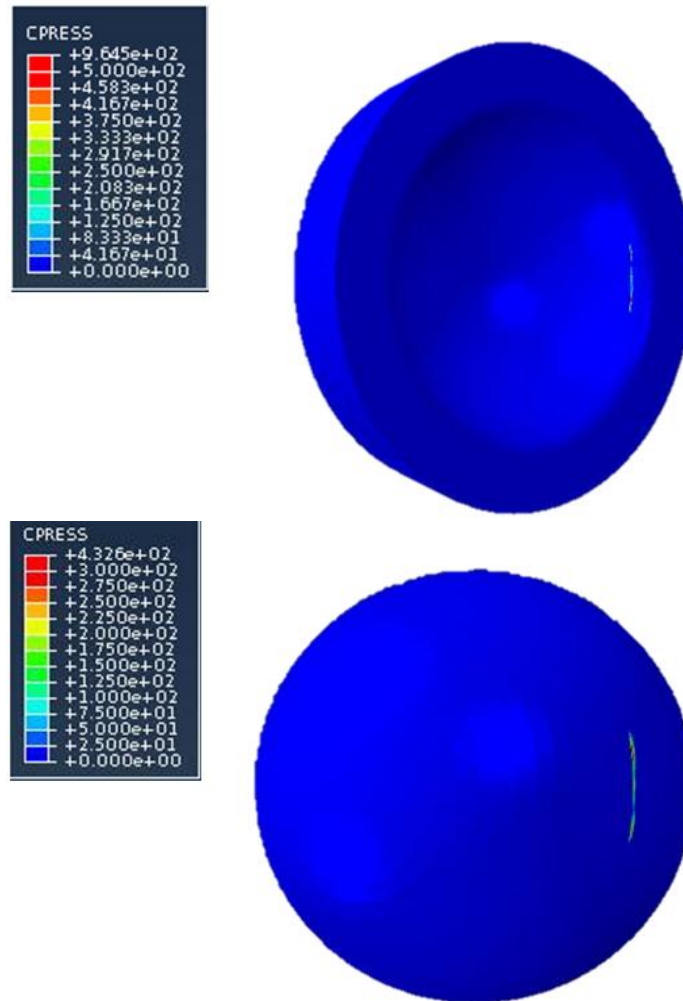


**Figure 43:** Comparison of the global model and the submodel results of contact area for a) the femoral head and, b) the acetabular liner

## 6.4 Contour Plots

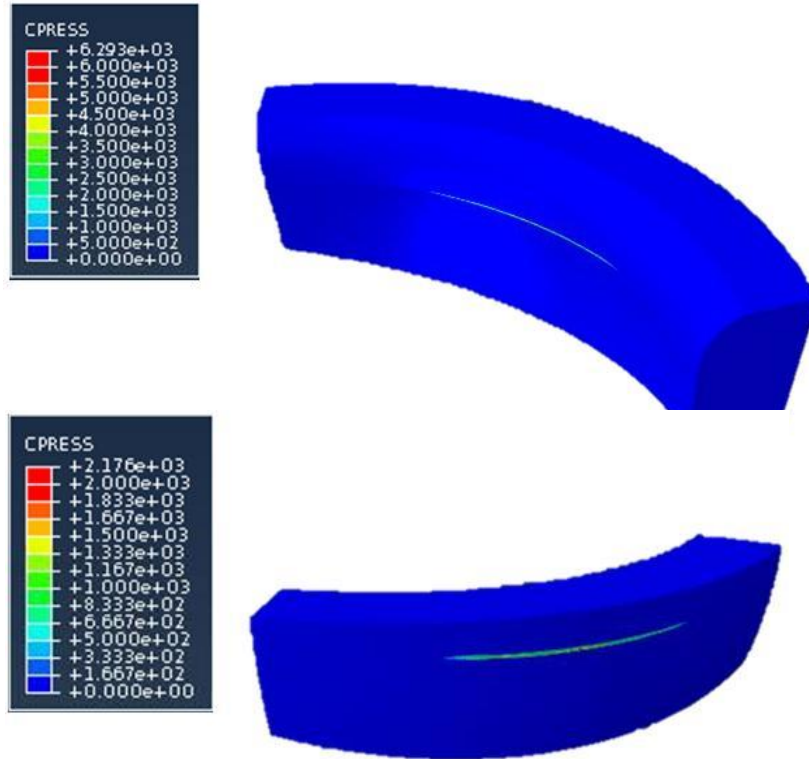
This section shows contour plots of stress at the contact on both the head and the liner in the global and the submodel analyses and the strain contour plots on the femur and the femoral neck. The contour plots shown in this section correspond to a time point of 6.9 ms into the event.

Figure 44 shows the stress distribution at the contact on the acetabular liner and the femoral head respectively, from the global model analysis. These results show the location of the contact area on the rim of the acetabular liner and the femoral head qualitatively. At about 7 ms into the simulation (which is clearly evident in animations of the FE simulation showing the contact stresses), the contact position changes rapidly from being on the crest to a position away from the rim of the liner suggesting the contact stresses increases causing severe wear.



**Figure 44:** Contact stress distribution during the reduction event at 6.9 ms for the liner (top) and, the head (bottom) from the global model analysis

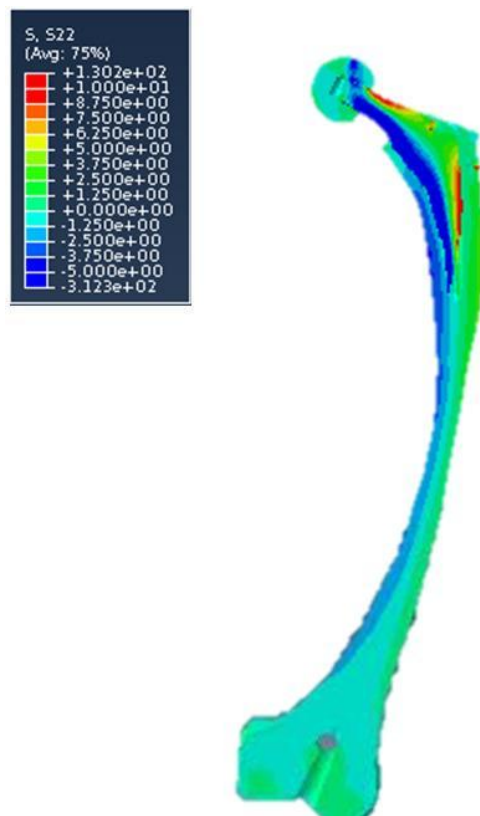
Figure 45 shows the stress distribution on the liner and the head respectively, from the submodel analysis.



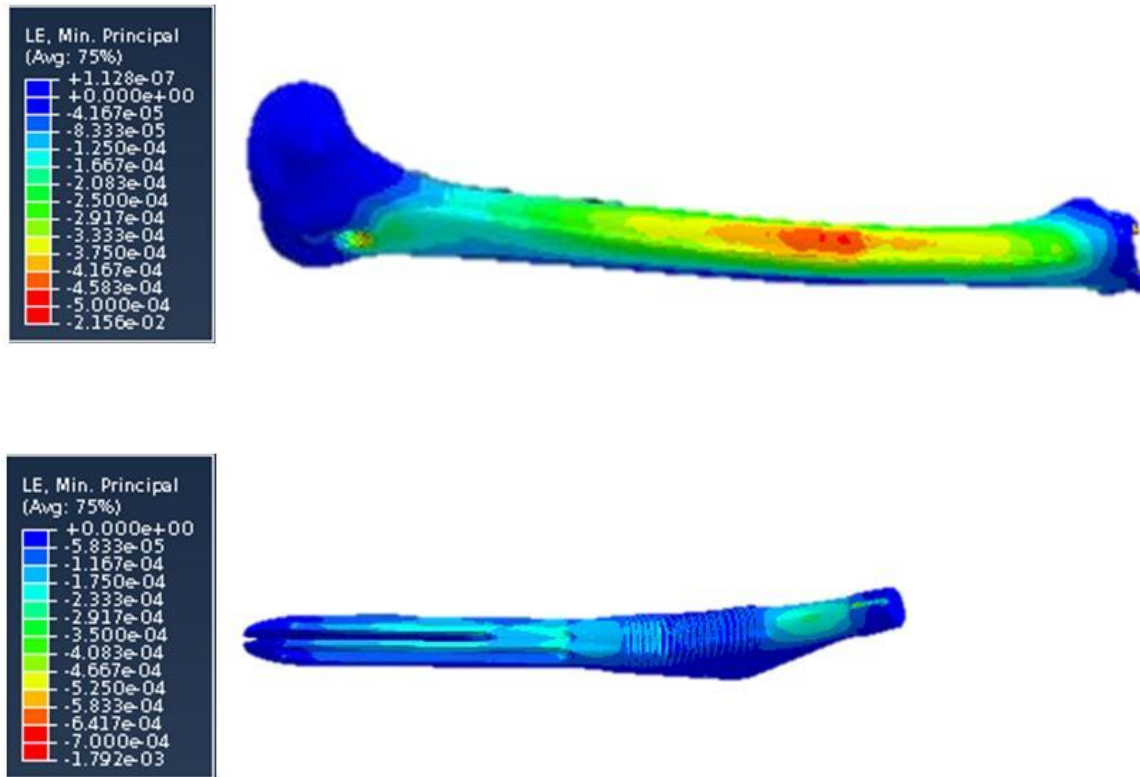
**Figure 45:** Contact stress distribution during the reduction event at 6.9 ms for the liner (top) and, the head (bottom) from the submodel analysis

Figure 46 shows the stress distribution in the femur (section view) at 20 X magnitude. The stress on the compressive side of the femur-femoral stem interface is maximum compared to the stresses in the femur, suggesting that the design of the femoral stem may be revised further to reduce these stresses during the reduction.

Figure 47 shows the contour plots of the minimum principal strain on the medial side of the femur and the femoral neck.



**Figure 46:** Stress distribution in the femoral sub-assembly (section view) at the time of maximum stress at the contact; displacements shown at 20 X magnitude



**Figure 47:** Contour plots of minimum principal strain on a point (where a strain gage was installed to measure the longitudinal strain) on the femur (top) and on the femoral stem (bottom)

## CHAPTER 7

### DISCUSSION

#### 7.1 Validation of the PSG in the FE Model

Validation of the PSG in the BMR model is important because the position of the initial point of head-liner contact is governed by this gap. The inner profile of the liner in the region of the rim has several differently shaped features – including a sharp edge called a *crest*, a straight segment about 1 mm long, and the edge radius. The PSG determines which of these features, the head initially contacts, and the slope at the point of contact strongly affects the moment arm length of the contact force. Since a key objective of the project was to accurately analyze the contact force, it was essential to set up the PSG accurately, both experimentally and computationally.

In the BMR model, the femoral head had three positions: (1) an initial fully reduced position (clearance included), (2) an intermediate position that mimicked the drop distance in the experiment, and (3) a final subluxed position with the desired PSG. The total horizontal displacement covered by the farthest point on the medial side of the femoral head from position (1) to (3) was measured computationally and compared against that measured in the experiment (as described in Section 4.8.2). The horizontal distance between positions (1) and (2) was measured from the 2D model and the FEA was set up initially starting with the position (2). The horizontal displacement between positions (2) and (3) was measured from the FE model (which constitutes the static load

phase). These two distances added together gave the total horizontal displacement in the FE model. For the 2 mm PSG, the horizontal displacement was 1.56 mm measured experimentally and 1.37 mm measured computationally. Hence, the head was more subluxed in the experiment.

Since the separate PSGs examined experimentally were only 1 mm different from each other, the end results from different PSGs may have been confused with one another as to which PSG the end results belong to. Hence, implementation of this deliberate setup procedure is important.

Also, the verification of the PSG is an additional confirmation of the initial state of the femur at the end of the static load phase. As the femur exhibited viscoelastic relaxation characteristics (discussed in detail below), it is important to account for the initial deformation under static loads before applying the dynamic loads. This verification combined with the verification of the initial strain on the femur and the femoral neck confirms the position of the components of the model before applying the dynamic input.

## **7.2 Behavior of the Femoral Cortex Material**

Composite femurs, which behave close to human femurs, have been preferred for biomechanical testing by researchers. In FEA involving composite femurs, researchers have modeled both the cancellous and the cortical materials as linear elastic and isotropic [51]. In contrast, during the axial compressive load test (described in Section 5.3), the femoral cortex exhibited viscoelastic relaxation characteristics. Similar characteristics were observed during the BMR test. The strain recorded on the femur experienced damping over a period of time after the reduction event. As seen in Figure 38a, the

magnitude of the peak strain decreased gradually after the period of interest. Nonetheless, the simplification that the femur can be modeled as linear elastic and isotropic in the FEA of the BMR model is justified, because the time period of interest was 5 ms, during which the femur behaves approximately as a linear elastic and isotropic material.

### **7.3 Effect of Friction**

This section discusses the effect of friction on (1) the PSG, (2) the velocity of the femoral head, and (3) the contact force between the bearing surfaces. Section 7.3.1 describes the effect of different lubricants that changed the coefficient of friction (CoF) at the contact. Sections 7.3.2 and 7.3.3 describe the effect of CoF on the velocity of the femoral head and the contact force respectively, as analyzed from the rigid body analysis.

#### **7.3.1 Effect of Lubrication on the PSG**

Lubrication applied on the contacting surfaces was important in the BMR test because it contributed to the slipping of the femoral head on the rim of the acetabular liner. The slipping effect, affected by the CoF, changes the PSG. The lubrication fluid used in the BMR test was 50% diluted bovine serum, which corresponds to a CoF of 0.06 according to Scholes et al [45]. As reported in the same paper, the coefficient of friction between COC bearing surfaces increased as the % of dilution increased. A similar pattern was observed during the BMR test. The reduction test was performed using (1) 50% diluted and, (2) undiluted bovine serum. The horizontal displacement (described in Section 7.1) measured in both the cases, was found to be less in case (2) than in case (1), showing that the femoral head was sliding out more when the lubricant was less dilute.

The decrease in the slipping effect (affected by the CoF) as the % of dilution increased, can be attributed to the decrease in the protein content due to dilution [45].

### 7.3.2 Effect of Friction on the Velocity of the Femoral Head

The CoF played an important role in affecting both the static and the dynamic responses of the BMR model. Therefore, error in the assumed CoF value for the FEA was regarded as an important potential root cause of the differences between the FEA and the experimental results. This section describes additional analysis to show the effects of friction on the BMR model.

The rigid body (described in Section 2.6) was analyzed to estimate the effect of the CoF on the velocity of the femoral head. Eq. 7, obtained by integrating the acceleration term in Eq. 5, gives the velocity of the femoral head during the reduction event.

$$v = \left( \int_0^t \alpha dt \right) (l + r) = \frac{(n-\mu t)C_N - sC_S + xW}{I_o} (l + r) \quad (7)$$

The time record of the velocity ( $v$ ) plotted for a range of CoFs is shown in Figure 48. As the CoF increased, the velocity of the femoral head decreased. It can also be observed that as the CoF increased, the acceleration of the femoral head decreased. According to this simple analysis, the CoF has a linear effect on the femoral head velocity. As seen in Figure 37, the peak velocity of the femoral head recorded in the experiment was less than that in the FEA. Therefore, we adjusted the CoF value in the FEA, using predictions from this simple analysis. So, the FEA of the BMR global model was rerun with a CoF value of 0.11 (approximately doubling the assumed CoF). Yet the results remained unchanged.

So, the dynamic responses of the BMR model were not significantly affected by altering (doubling) the assumed CoF in the FEA according to the rigid body predictions.

A few more analysis runs would be appropriate to quantify effects of CoF on the dynamic response of the BMR model. This outcome provides an objective and scope for further research needed to improve the contact modeling in similar scenarios.

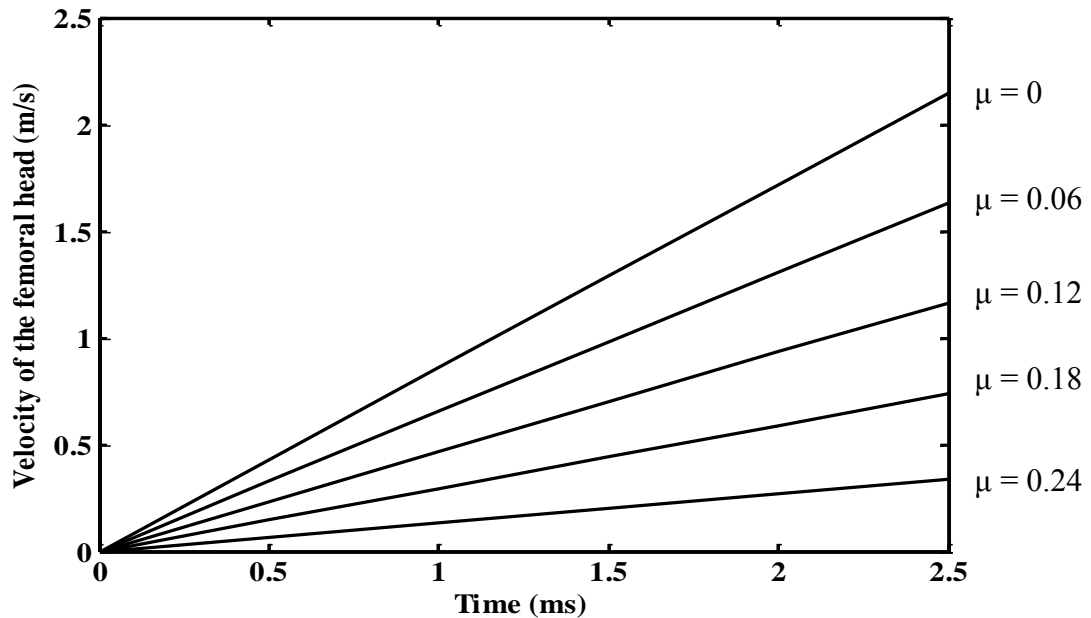


**Figure 48:** Time record of velocity of the femoral head for different CoF ( $\mu$ )

### 7.3.3 Effect of Friction on the Contact Force

The effect of friction (at the contact) on the contact force was analyzed using the rigid body analysis. The denominator on the right hand side of the contact force equation (Eq. 6) has the coefficient of friction term ( $n-\mu t$ ) in it. So, the contact force approaches infinity when this term equals zero. Accordingly,  $C_N \rightarrow \infty$  as  $\mu \rightarrow \frac{n}{t}$ .

This is shown in Figure 49. The moment arm lengths (labeled as  $n$  and  $t$  in Figure 11) change when the angle subtended by the contact force changes. The contact force angle also depends on the spring force applied. In the mechanism incorporated to achieve

the desired PSG in the BMR model, as the spring force is increased, it pulls the femoral sub-assembly more towards the lateral side, which changes the moment arm lengths ( $n$  and  $t$ ). When the ratio  $n/t$  equals the value of  $\mu$ , the force at the contact becomes so high that a locking condition is reached. It is when this locking condition is reached that reduction cannot happen. While performing the BMR test for the 4 mm PSG in the laboratory, the locking condition was reached with a spring force of 400 N (the same value of lateral force applied by Nevelos et al. [30]).

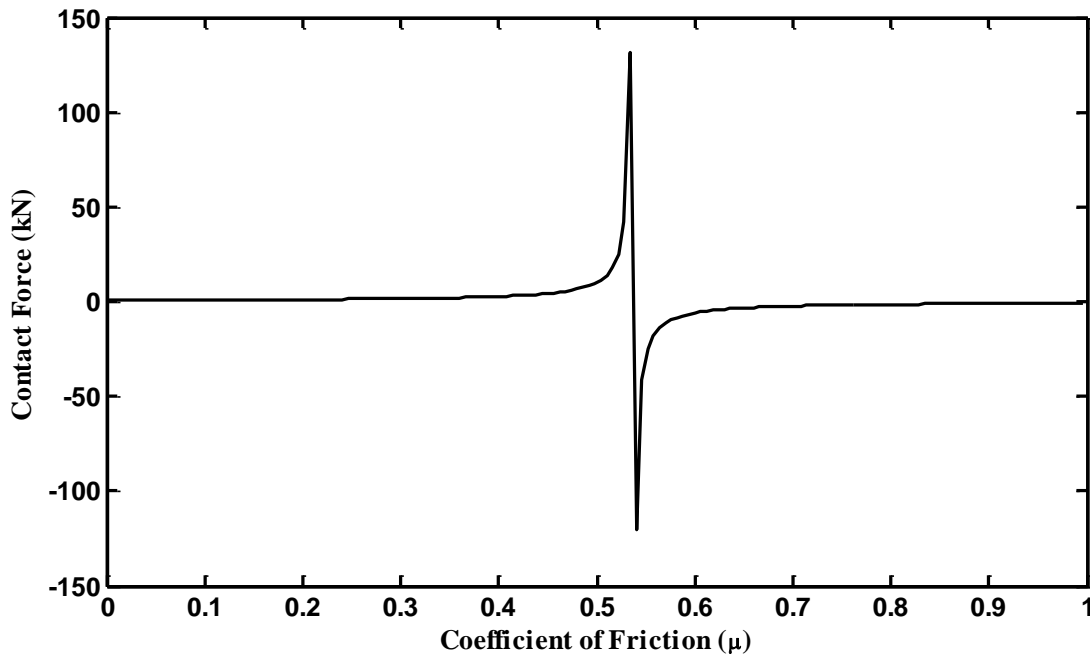


**Figure 49:** Contact force vs. Coefficient of Friction from rigid body analysis; the plot shows an infinite contact force for a particular friction value – this is when the femoral head does not reduce into the acetabular liner

This fundamental analysis revealed the existence of the locking condition in the BMR model in addition to the rigid body analysis described in Chapter 2. Overall, it can be concluded that the dynamic responses of the BMR model are sensitive to the spring force and to the lubricant used.

## 7.4 Key Hypothesis

This section describes an interesting phenomenon observed in the experiment related to the key hypothesis described in Section 1.5. We hypothesized that the contact force duration in the BMR model would be close to the transit time of the stress waves in the femur. But the contact force duration (as seen in Figure 41) was about 5 ms, which was *five times* as long as the measured 1ms transit time of the stress waves in the femur. The following describes the observations (which are clearly evident in animations of the FE simulation of the femur sub-assembly's displacements) that explain this contradiction of the original hypothesis.

As seen in the strain plot of the femur from the FEA (Figure 40a), the strain curve comprises: (1) a curve that damps out over time and (2) local peaks on that curve seen after 8 ms into the simulation time. The strain curve is a superposition of strain waves in the femur due to pure bending and, the strain in the femur due to the propagation of stress waves because of the inner impact of the head at about 8 ms. Prior to 8 ms, the femur is first bending relatively slowly under the increasing displacement of the pelvic sub-assembly. Then, although the pelvic sub-assembly continues to displace in the same direction (tending to increase femur bending), the femoral head begins to slip on the liner's edge (at ~5 ms). Thus, the femur starts to un-bend, which it continues to do until the femoral head impacts with the liner ID. Then, stress waves are generated due to the inner impact, and these are recorded as the local peaks in the FEA strain curve. So, the transit time is to be measured between those local peaks seen after 8 ms into the simulation time. These peaks are shown in Figure 40c. The initial phase of femur bending is due to the gradual velocity dynamic input, and there is no evidence that the contact

force or the duration of contact is strongly influenced by dynamic stress waves during this phase. This contradicts one of the key hypotheses of this research. Nevertheless, the results also demonstrate that this result was influenced by the rate of loading; a much more rapid loading rate may have produced an effect closer to that hypothesized.

As a simple engineering model of the human body, the BMR model does not include fully characterized inputs that actually happen during the heel-strike phase of human gait. Hence, there is a need for combined research by engineers and kinesiologists to better determine the inputs that cause reduction in the hip joint so that the BMR model can be improved.

### **7.5 Submodeling Procedure – Future Scope**

A submodeling approach was undertaken in the literature [43]. It is a step-by-step procedure, which involves three convergence studies. First, the global model stress is studied for convergence. Once the boundaries of the submodel are decided, the displacement BCs (extracted from the refinements of the global model) at those submodel boundaries are studied for convergence. And then the submodel is modeled by applying the displacement BCs extracted from the finest global model (shown to have stresses converged within a chosen tolerance). The submodel is refined further to study stress convergence at the site of interest. Though this rigorous procedure yields accurate results in submodeling, it is a very time-consuming process. The number of convergence checks and mesh refinement steps required by this approach was deemed to require more model manipulation (thus, human labor) and analysis runs than allowed by the project budget. Therefore, we employed a strategy that used a very fine mesh in the global model (to

avoid the risk of non-convergence), that was further strategically refined local to the point of interest (the head-liner contact region). This strategy took advantage of tremendous computational resources (available at Exponent, Inc.) to minimize the human labor that would be necessary if we had started with a coarse global model. In this strategy, the criterion for ensuring that the global model results were sufficiently accurate for transference to the submodel was not global model stress convergence. Rather, it was consistency of the contact force induced at the head-liner contact interface. As shown in Figure 41 and Figure 42, the contact forces exhibited poor consistency between the global model and the submodel (<100% difference). The following sections describe potential reasons for the inconsistency and offer suggestions for future work that might resolve the problem.

### **7.5.1 Contact Stiffness – Boundary Conditions**

When the submodel was refined, the contact interface changed unpredictably. As the submodel was finer than the global model at the contact, more elements interacted in the former, which changed the contact stiffness at the interface when compared to the latter. The materials (ceramics) in contact are very stiff. The number of elements contacting each other at the contact changes the stiffness of the contact interface rapidly, in turn, changing the contact force. This change is seen in Figure 41, in which the contact force in the submodel is considerably higher than that in the global model.

The aggressive approach taken here might give us fruitful results if *traction* BCs were applied to the submodel. That approach would guarantee that the contact force would remain the same in the submodel as it was in the global model. But, traction BCs could not be applied because of the software's limitation, as only displacement BCs can

be applied in the Abaqus/Explicit solver. Thus, an ability to apply traction BCs (or, even better, Robin BCs) is a natural avenue to continued research in the FE community.

### **7.5.2 Successive Submodeling Approach to Improve Consistency and Convergence**

Convergence analysis of global model BCs on the submodel boundaries may be performed to ensure that BCs being applied to the submodel do not cause any discrepancy in the submodel results. But, even if the global model was converged on the submodel boundary to within a tolerance, e.g. 1%, the same problem could arise, because even converged displacement BCs could cause a change in the contact force when the contact stiffness simultaneously undergoes changes due to the mesh refinement around the contact point. Moreover, even very small changes in contact stiffness can have a great effect on contact force under the displacement BCs, because the materials are very stiff.

Overall, the error in the submodel contact force may be because of (1) the use of displacement BCs where a traction or Robin BC might have been more appropriate or (2) lack of global model convergence. Solving the BMR model, a 3D dynamic problem, with a global mesh with 861,881 nodes and 571,572 elements took ~31 hours. And, though a convergence study could and should be performed for the global model and submodels separately, convergence of these individual problems might not avoid inconsistency in their predictions of the traction at the submodel boundary. So, we recommend that the following procedure be followed to arrive at more accurate submodel results with displacement BCs.

- First, solve the global model with a locally refined mesh. Output the dynamic responses of the global model and the inferred outputs i.e., the contact force and the contact stress.

- Then, create a first submodel (geometry) by partitioning the global model at the femoral neck (from the femoral sub-assembly) and by retaining the acetabular liner geometry (by removing the geometries of the acetabular shell and the test block from the pelvic sub-assembly), as shown in Figure 50.

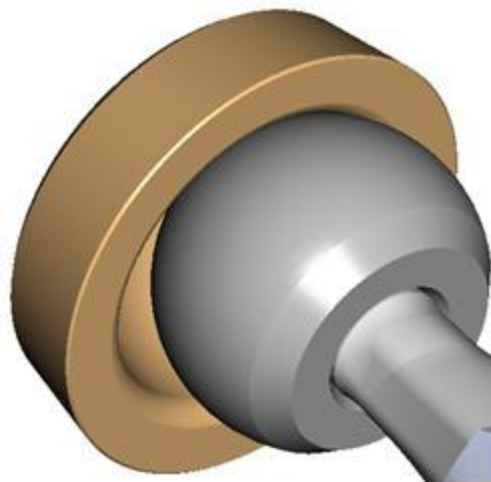


**Figure 50:** Proposed first submodel partitioned at the femoral neck (from the femoral sub-assembly) and the acetabular liner (from the pelvic sub-assembly)

- Mesh the first submodel finer than the global mesh with local refinement at the contact region. The BCs on the partitions of the first submodel are taken from the single global model.
- Extract the dynamic responses of the first submodel and the inferred outputs and compare them with the global model results.
- If the results (contact force and contact stress) of the first submodel show close conformity with those of the global model, then perform a second submodel (similar to the BMR submodel) analysis. The displacement BCs of the second submodel are extracted from the first submodel.

- Extract and compare the contact force and the contact stress results of the second submodel against the first submodel results. Perform convergence study on the second submodel and output the final results of contact force and contact stress from a fine second submodel.
- If the results of the first coarse submodel i.e., the contact force and the contact stress do not show close conformity with those of the global model, then, perform convergence study for the displacement BCs on the global model at the first submodel boundaries. This will ensure that the displacement BCs that will be applied to the first submodel are converged.
- Then, analyze a second submodel (as described in the previous bullet point) further for the end results of contact force and contact stress.

Solving the BMR model using the above mentioned submodeling approach is strongly recommended as future work.

## **CHAPTER 8**

### **CONCLUSIONS AND FUTURE SCOPE**

This chapter summarizes conclusions drawn from the experimental and FE analyses of contact mechanics between COC hip implants under edge loading and micro-separation modes. Recommendations for future scope of the BMR model are provided.

#### **8.1 Conclusions**

- The contact mechanics of a ceramic-on-ceramic (COC) bearing couple, in particular during edge loading that accompanies sudden reduction following micro-separation, has been analyzed in this study.
- A two-rod impact test was proposed and analyzed to demonstrate the correctness of data analysis and simulation methods used in three contexts: a finite-element (FE) model was verified using an analytical model, and both of these were validated against an experimental model. Similar instrumentation techniques used in analyzing the contact mechanics in this simple problem were used to analyze a contact scenario in the complex BioMechanical Reduction (BMR) model.
- The BMR tests conducted in the laboratory demonstrated that the velocity of the femoral head during the reduction event and the strain in the femur and the femoral neck increase as the micro-separation increases. The increase in the velocity of the femoral head indicates that the contact force increases as the polar separation gap (PSG) increases.

- The FE global BMR model was validated (though with an explainable error) against the experimental model by comparing the dynamic responses of the model to the corresponding laboratory measurements.
- The FE version of the BMR model gave the time history of contact force, contact stress and contact area on both the head and the liner during the reduction for the 2 mm PSG.
- The aggressive submodeling approach refined the analysis with computational efficiency, but showed inconsistency of traction when compared to the global model results (contact force and contact stress).

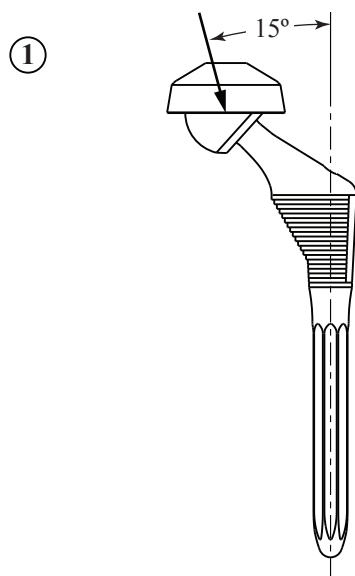
## 8.2 Future Scope

As observed in the presented results of the contact mechanics, the contact forces and the contact stresses predicted by the BMR submodel were higher than those in the global model due to the limitations of the Abaqus software, thus demanding either use of traction BCs or a detailed procedure as described in Section 7.5. Future work involves convergence study of the submodel to accurately determine the contact mechanics of COC hip bearings in the micro-separation mode. Analyzing the BMR submodel with traction BCs could be important to more accurately predicting the contact force and stresses for such contact problems. Contemporary concepts of concurrent multiscale modeling to reduce BC error between the submodel and the global model may also be considered as future work [55]. The FEA of the BMR model should also be further extended to include more micro-separation values, mainly the worst-case loading scenario. The coefficient of friction used in the FEA has to be investigated to quantify its effect on the model's dynamic response.

The material properties of the femoral cortex had to be adjusted in this study by performing a separate test (described in Section 5.3) both experimentally and computationally. So, it is recommended that future research should include investigation of femoral cortex material properties by conducting more experiments to accurately determine its elastic Young's modulus and Poisson's ratio to gain more confidence in the computational studies.

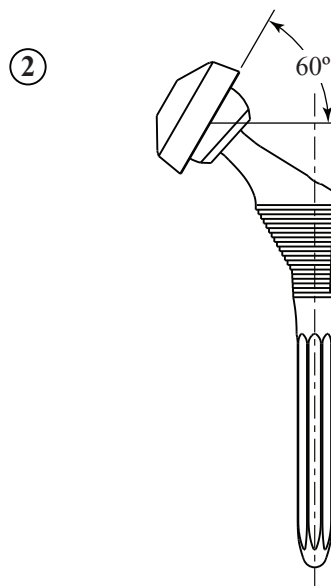
A limitation of this study was the lack of information about the kinematics of the real hips undergoing micro-separation and edge loading. With the benefit of relevant in-vivo data, the approach taken here would be even more useful to orthopedic research if the tests and analyses could be conducted. Bergmann et al [38] reported in-vivo data of contact forces in artificial hips during daily activities. We propose that such research ought to be extended to cases of short duration events, such as edge-loading, to provide further data that will be used in models and tests such as the BMR model.

## **APPENDIX A**

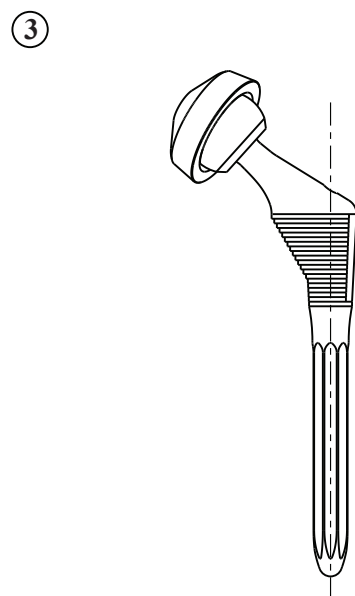


① The setup begins with an A/P view of the patient's left hip, assuming the patient is oriented vertically. This is also termed the Front view.

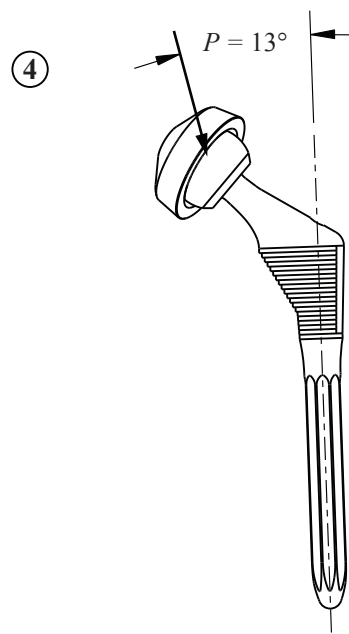
The components are not yet oriented. However, the load line is oriented at  $15^\circ$  from the vertical to represent its orientation at the peak load stage of stance phase.



② Next, the acetabular cup is rotated about an A/P axis through its center to an abduction angle of  $60^\circ$ . This represents a worst case scenario, compared to the typically stated ideal abduction angle of  $45^\circ$ . This is a worst case scenario because at this angle, the cup provides less resistance to dislocation and subluxation. Thus, the potential for edge loading is increased.

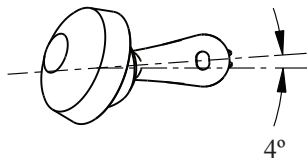


③ Next, the cup's anteversion is established. The cup is rotated about a vertical axis to an anteversion angle of  $20^\circ$ .



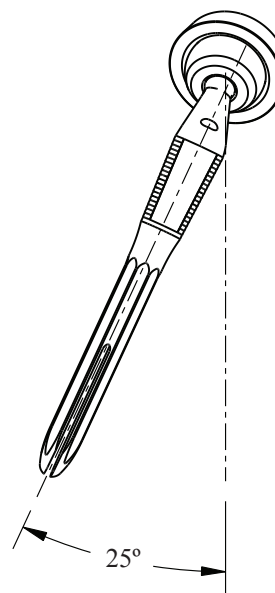
④ Next, the femoral stem's adduction-abduction orientation (angle  $P$  in ISO 14242-1) is established. The stem is rotated to an angle of  $13^\circ$  from the load line. This comes from an initial value,  $10^\circ$ , of  $P$ , to which  $3^\circ$  of adduction is added in accordance with Figure 2 of that standard, which sets the the position at the start of the gait cycle.

⑤



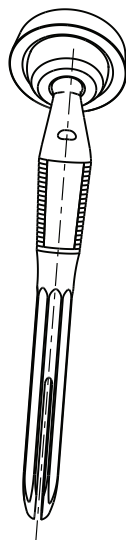
Next, a top view is taken. The internal-external rotation of the femoral component is established by rotating the femoral stem about a vertical axis through the center of the head. The stem is rotated 4° external to the sagittal plane. This comes from an initial position of  $\gamma/2 = 6^\circ$  internal to the sagittal plane, per ISO 14242-1, to which 10° of external rotation is added in accordance with Figure 2 of the standard.

⑥



Next, the flexion-extension orientation of the femur is established by rotating the femoral stem about a M/L axis through the center of the head. The stem is rotated to 25° of flexion from the sagittal plane.

⑦

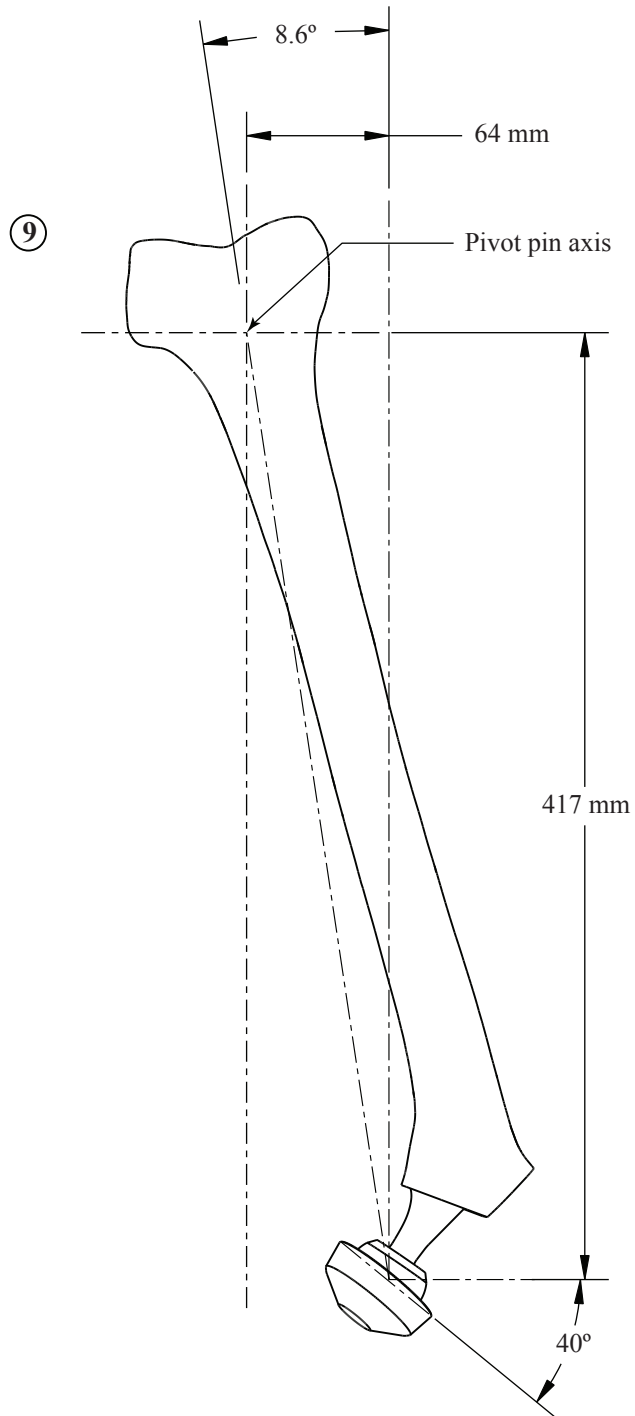


Next, the entire construct is rotated in the right view plane to a more vertical orientation. The construct is rotated to establish a horizontal orientation of the distal rotation pin (not shown) that passes through the distal metaphysis in a roughly A/P direction. As such, the construct is rotated 20° about an M/L axis, creating the orientation shown.

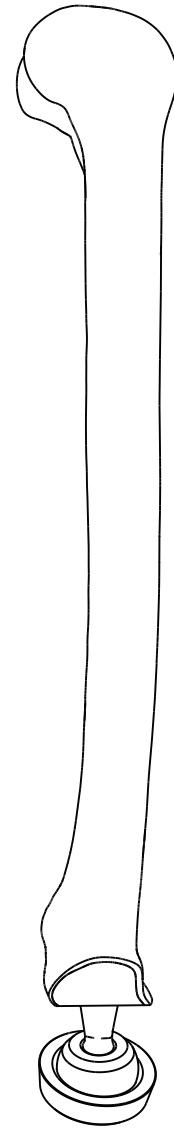
⑧



Next, a front view is taken. The entire construct is rotated again, this time in the front view plane. The construct is rotated to re-orient the 15° load line to a vertical orientation, to suit a typical test frame which has a vertically oriented actuator.



Next, the entire construct is rotated 180° in the view plane. The inverted setup better suits the configuration of the test machine and the fixtures.



Right projection view.

## **APPENDIX B**

## FEMUR – IMPLANT ASSEMBLY AND FEMUR CONSTRUCT MEASUREMENTS

1. **Aim:** The main aim was to construct the assembly of - a femur, a femoral stem and a femoral head, press-fit a dowel pin on the distal end of the femur and *take coordinate measuring machine (CMM) measurements to locate all the components of the assembly with respect to a datum coordinate system.*
2. **Femur – implant assembly:** The femur was initially cut based on a resection guide corresponding to a 23 mm distal diameter of the femur. Various tools were used like the box osteotome, distal reamers and conical reamers starting with a smaller size to initiate the path for the stem. Later, broaching was performed with a proper alignment against the lateral cortex to prevent varus positioning of the stem. The assembly (3 parts – femur, femoral stem and femoral head) is shown below in Figure 1. The femoral stem is a 109-1623 model and the femoral head is of diameter 36 mm specified by 12/14+4 (mm) tapered hole.

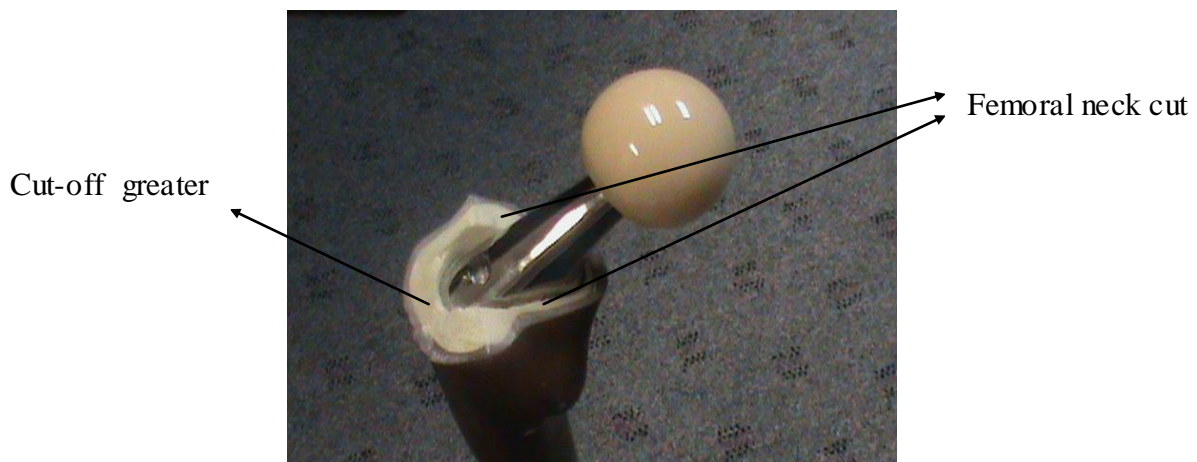


**Figure 51:** Femur – implants (femoral stem and head) assembly

**3. Femur Construct Measurements:** The aim of taking the CMM measurements of the femur – implant assembly was to construct a datum coordinate system and locate the femur with respect to the constructed datum, and then the femoral stem, femoral head and the press-fit dowel pin.

### **3.1. Constraining the femur construct in 3D space**

- The femur construct was constrained in 3D space by considering a datum coordinate system formed by the base plate of the CMM and two mutually perpendicularly placed gauge blocks on the base plate. The datum coordinate axes obey the right hand rule.
- The assembly was first placed on the base plate making 3 contact points (2 on either of the condyles and 1 on the lesser trochanter).
- Then, the farthest points on the condyles were contacted with the gauge block 1
- (2 contact points).
- Moving the femur along these 2 planes contacts the medial epi-condyle with a gauge block 2 (1 contact point).
- This arrangement is as shown in Figure 2.

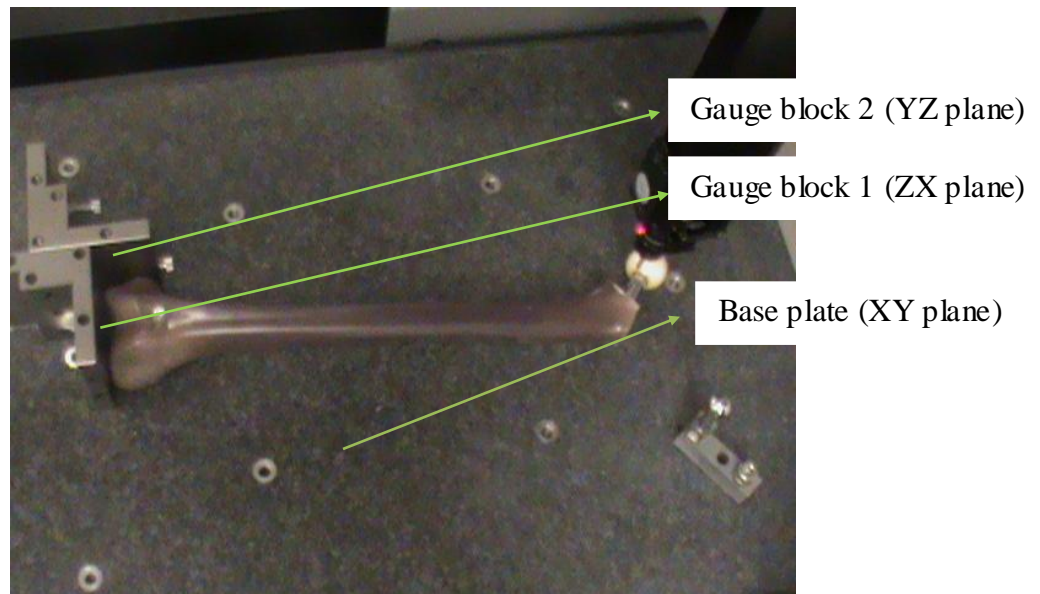


**Figure 52:** Setup of the femur construct on the CMM, showing the datum planes

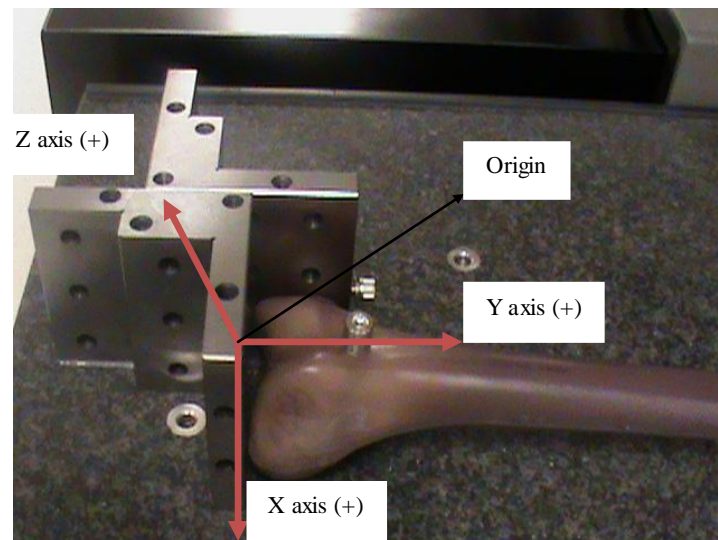


**Figure 53:** Image of the femur's distal end showing the datum coordinate axes and the origin; Z-axis points perpendicular and outward to the granite base plate

### 3.2.CMM Measurements

**3.2.1. Measuring the datum planes with respect to each other by probing all the planes:** The constructed datum planes were measured with respect to each other for perpendicularity. Measurements are tabulated in Table 1.

**Table 8:** Angles of constructed datum planes with respect to each other

Probed plane	$\angle XY$	$\angle YZ$	$\angle ZX$	Flatness
XY	0.001°	90.000° <sup>!</sup>	89.999° <sup>!</sup>	-
ZX	89.962°	89.999°	0.038°	0.00017
YZ	89.982°	0.019°	89.992°	0.00006

**3.2.2. Probing the distal pin cylinder:** The surface of the distal pin cylinder was probed to get the coordinate of the point of the axis intersecting the XY plane and required angles to define its location as shown in Figure 4.

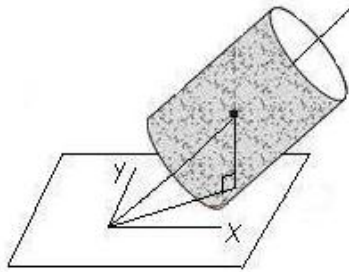


**Figure 54:** Image demonstrating the projection of a cylinder axis onto the XY plane

(X,Y) coordinate\*: X = 1.95962, Y = 1.83864

Angle of the cylinder axis with the XY plane:  $\angle XY = 86.838^\circ$

Angle between the projection of cylinder axis with the X and Y axes:  $\angle X=20.244^\circ$ ,  $\angle Y= 69.756^\circ$

### 3.2.3. Probing the center of the femoral head

Diameter ( $\emptyset$ ) = 1.41651 inches, Circularity = 0.00024

Center of the femoral head (X, Y, Z): X = 1.77527, Y = 18.46420, Z = 1.00382

**3.2.4. Probing the bottom surface of the head:** The flat surface on the bottom of the femoral head was probed (constrained rotation about its center).

Flatness = 0.00019, Perpendicular distance of the flat surface from the origin = 11.69289

Orientation of the plane of the bottom surface of the head with respect to the datum planes

$\angle XY = 89.809^\circ$ ,  $\angle YZ = 46.489^\circ$ ,  $\angle ZX = 43.512^\circ$

**3.2.5. Probing a small flat on the side of the femoral neck (Figure 5)**



Small flat on the side of the femoral neck

**Figure 55:** Image showing the small flat on the side of the femoral neck

**Table 9:** Measurements of the flat on the femoral neck, plane of the femoral neck cut and greater trochanter cut-off plane with respect to the constructed datum planes.

<b>Probed plane</b>	<b>Flatness</b>	<b>Perpendicular distance from origin of datum</b>	<b><math>\angle XY</math></b>	<b><math>\angle YZ</math></b>	<b><math>\angle ZX</math></b>
Flat on the side of femoral neck	0.00057	2.38537	3.626°	89.240°	86.454°
Femoral neck cut	0.00507	14.37837	89.833°	65.091°	24.910°
Greater trochanter cut-off plane	0.00652	16.24513	89.790°	54.458°	35.543°

The plane of the femoral neck cut and the plane of the cut-off greater trochanter (as shown in Figure 1) were also probed and the measurements are tabulated in Table 2 above.

## REFERENCES

- [1] "ISO 14242-1: Implants for Surgery - Wear of total hip-joint prostheses - Part 1: Loading and displacement parameters for wear-testing machines and corresponding environmental conditions for test," vol. 1, ed. Geneva, Switzerland: ISO, 2002.
- [2] R. S. Nizard, *et al.*, "Ten-year survivorship of cemented ceramic-ceramic total hip prosthesis," *Clin Orthop Relat Res*, pp. 53-63, Sep 1992.
- [3] J. A. D'Antonio, *et al.*, "A titanium-encased alumina ceramic bearing for total hip arthroplasty: 3- to 5-year results," *Clin Orthop Relat Res*, vol. 441, pp. 151-8, Dec 2005.
- [4] J. J. Yoo, *et al.*, "Alumina-on-alumina total hip arthroplasty. A five-year minimum follow-up study," *J Bone Joint Surg Am*, vol. 87, pp. 530-5, Mar 2005.
- [5] A. S. Brown, "Hip New World," *Mechanical Engineering*, vol. 2006, pp. 28-32, 2006.
- [6] L. Sedel and A. Raouf, "Engineering aspect of alumina on alumina hip prosthesis," *Proc Inst Mech Eng H*, vol. 221, pp. 21-7, Jan 2007.
- [7] J. Fisher, *et al.*, "An in vitro study of the reduction in wear of metal-on-metal hip prostheses using surface-engineered femoral heads," *Proc Inst Mech Eng H*, vol. 216, pp. 219-30, 2002.
- [8] I. Clarke, "Ultra-low wear rates for rigid-on-rigid bearings in total hip replacements," *Proc Inst Mech Eng H*, vol. 214, pp. 331-47, 2000.
- [9] K. H. Koo, *et al.*, "Isolated fracture of the ceramic head after third-generation alumina-on-alumina total hip arthroplasty," *J Bone Joint Surg Am*, vol. 90, pp. 329-36, Feb 2008.
- [10] C. Piconi, *et al.*, "Zirconia heads in perspective: a survey of zirconia outcomes in total hip replacement," *Hip Int*, vol. 17, pp. 119-30, Jul-Sep 2007.
- [11] G. Maccauro, *et al.*, "Fracture of a Y-TZP ceramic femoral head. Analysis of a fault," *J Bone Joint Surg Br*, vol. 86, pp. 1192-6, Nov 2004.
- [12] R. Heros, Willmann G., "Ceramic in Total Hip Arthroplasty: History, Mechanical Properties, Clinical Results and Current State of the Art," *Seminarts in Arthroplasty*, vol. 9, pp. 114-122, 1998.
- [13] G. Willmann, "Ceramic femoral head retrieval data," *Clin Orthop Relat Res*, vol. 379, pp. 22-28, 2000.
- [14] J. C. Keurentjes, *et al.*, "High incidence of squeaking in THAs with alumina ceramic-on-ceramic bearings," *Clin Orthop Relat Res*, vol. 466, pp. 1438-43, Jun 2008.
- [15] C. Varnum, *et al.*, "Ceramic bearings in total hip arthroplasty: frequency and types of noises," presented at the 9th Congress of the European Federation of National Associations of Orthopaedics and Traumatology, Nice, 2008.
- [16] K. Mai, *et al.*, "Incidence of 'squeaking' after ceramic-on-ceramic total hip arthroplasty," *Clin Orthop Relat Res*, vol. 468, pp. 413-7, Feb 2010.
- [17] W. L. Walter, "A Review of Squeaking Hips," *J Am Acad Orthop Surg*, vol. 18, p. 319, 2010.
- [18] A. Cogan, *et al.*, "Occurrence of noise in alumina-on-alumina total hip arthroplasty. A survey on 284 consecutive hips," *Orthop Traumatol Surg Res*, Mar 7 2011.
- [19] A. S. Ranawat and C. S. Ranawat, "The squeaking hip: a cause for concern-agrees," *Orthopedics*, vol. 30, pp. 738, 743, Sep 2007.
- [20] C. C. Yang, *et al.*, "The squeaking hip: a cause for concern-disagrees," *Orthopedics*, vol. 30, pp. 739-42, Sep 2007.

- [21] S. Taylor, *et al.*, "The role of stripe wear in causing acoustic emissions from alumina ceramic-on-ceramic bearings," *J Arthroplasty*, vol. 22, pp. 47-51, Oct 2007.
- [22] A. Hothan, *et al.*, "The influence of component design, bearing clearance and axial load on the squeaking characteristics of ceramic hip articulations," *J Biomech*, vol. 44, pp. 837-41, Mar 15 2011.
- [23] C. Chevillotte, *et al.*, "The 2009 Frank Stinchfield Award: "Hip squeaking": a biomechanical study of ceramic-on-ceramic bearing surfaces," *Clin Orthop Relat Res*, vol. 468, pp. 345-50, Feb 2010.
- [24] C. Restrepo, *et al.*, "The noisy ceramic hip: is component malpositioning the cause?," *J Arthroplasty*, vol. 23, pp. 643-9, Aug 2008.
- [25] W. L. Walter, *et al.*, "Edge loading in third generation alumina ceramic-on-ceramic bearings: stripe wear," *J Arthroplasty*, vol. 19, pp. 402-13, Jun 2004.
- [26] T. J. Blumenfeld, *et al.*, "In vivo assessment of total hip femoral head separation from the acetabular cup during 4 common daily activities," *Orthopedics*, vol. 34, p. 127, Jun 2011.
- [27] D. A. Dennis, *et al.*, ""In vivo" determination of hip joint separation and the forces generated due to impact loading conditions," *Journal of Biomechanics*, vol. 34, pp. 623-629, 2001.
- [28] A. V. Lombardi, Jr., *et al.*, "An in vivo determination of total hip arthroplasty pistoning during activity," *J Arthroplasty*, vol. 15, pp. 702-9, Sep 2000.
- [29] J. E. Nevelos, "The influence of acetabular cup angle on the wear of "BIOLOX Forte" alumina ceramic bearing couples in a hip joint simulator.," *Journal of Materials Science: Materials in Medicine*, vol. 12, pp. 141-4, 2001.
- [30] J. Nevelos, *et al.*, "Microseparation of the centers of alumina-alumina artificial hip joints during simulator testing produces clinically relevant wear rates and patterns," *J Arthroplasty*, vol. 15, pp. 793-5, Sep 2000.
- [31] T. Shishido, *et al.*, "Clinical and simulator wear study of alumina ceramic THR to 17 years and beyond," *J Biomed Mater Res B Appl Biomater*, vol. 67, pp. 638-47, Oct 15 2003.
- [32] T. Stewart, *et al.*, "Long-term wear of HIPed alumina on alumina bearings for THR under microseparation conditions," *J Mater Sci Mater Med*, vol. 12, pp. 1053-6, Oct-Dec 2001.
- [33] A. V. Lombardi, *et al.*, "An in vivo determination of total hip arthroplasty pistoning during activity," *J Arthroplasty*, vol. 15, pp. 702-709, 2000.
- [34] M. M. Mak and Z. Jin, "Analysis of contact mechanics in ceramic-on-ceramic hip joint replacements," *Journal of Engineering In Medicine*, vol. 216, pp. 231-6, 2002.
- [35] E. Sariali, *et al.*, "Three-dimensional modeling of in vitro hip kinematics under microseparation regime for ceramic on ceramic total hip prosthesis: an analysis of vibration and noise," *J Biomech*, vol. 43, pp. 326-33, Jan 19 2010.
- [36] E. Sariali, *et al.*, "In vitro investigation of friction under edge-loading conditions for ceramic-on-ceramic total hip prosthesis," *J Orthop Res*, vol. 28, pp. 979-85, Aug 2010.
- [37] A. J. Langdown, *et al.*, "Incomplete seating of the liner with the Trident acetabular system: a cause for concern?," *J Bone Joint Surg Br*, vol. 89, pp. 291-5, Mar 2007.
- [38] G. Bergmann, *et al.*, "Hip contact forces and gait patterns from routine activities," *Journal of Biomechanics*, vol. 34, pp. 859-871, 2001.
- [39] M. M. Mak, *et al.*, "Effect of microseparation on contact mechanics in ceramic-on-ceramic hip joint replacements," *Proc Inst Mech Eng H*, vol. 216, pp. 403-8, 2002.

- [40] M. Manaka, *et al.*, "Stripe wear rates in alumina THR--comparison of microseparation simulator study with retrieved implants," *J Biomed Mater Res B Appl Biomater*, vol. 69, pp. 149-57, May 15 2004.
- [41] A. P. Christoforou and A. S. Yigit, "Effect of flexibility on low velocity impact response," *Journal of Sound and Vibration*, vol. 217, pp. 563-78, 1998.
- [42] D. Stoianovici, "A Critical Study of the Applicability of Rigid-Body Collision Theory," *ASME Journal of Applied Mechanics*, vol. 63, pp. 307-316, 1996.
- [43] N. G. Cormier, *et al.*, "Aggressive submodelling of stress concentrations," *International Journal for Numerical Methods in Engineering*, vol. 46, pp. 889-909, 1999.
- [44] F. C. Anderson and M. G. Pandy, "Individual muscle contributions to support in normal walking," *Gait Posture*, vol. 17, pp. 159-69, Apr 2003.
- [45] S. C. Scholes and A. Unsworth, "Comparison of friction and lubrication of different hip prostheses," *Proc Inst Mech Eng [H]*, vol. 214, pp. 49-57, 2000.
- [46] A. Sanders, Tibbitts, I., Deepika, K., "Contact Mechanics of Impacting Slender Rods: Measurement and Analysis," *Proceedings of 2011 SEM Annual Conference and Exposition on Experimental and Applied Mechanics*, 2011.
- [47] M. P. Gardner, *et al.*, "Mechanical evaluation of large-size fourth-generation composite femur and tibia models," *Ann Biomed Eng*, vol. 38, pp. 613-20, Mar 2010.
- [48] L. Cristofolini and M. Viceconti, "Mechanical validation of whole bone composite tibia models," *J Biomech*, vol. 33, pp. 279-88, Mar 2000.
- [49] A. D. Heiner, "Structural properties of fourth-generation composite femurs and tibias," *J Biomech*, vol. 41, pp. 3282-4, Nov 14 2008.
- [50] Hibbitt, *et al.*, "ABAQUS/Standard User's Manual," Hibbitt, Karlsson and Sorensen, Inc.2002.
- [51] M. Papini, *et al.*, "The biomechanics of human femurs in axial and torsional loading: comparison of finite element analysis, human cadaveric femurs, and synthetic femurs," *J Biomech Eng*, vol. 129, pp. 12-9, Feb 2007.
- [52] J. M. Elkins, *et al.*, "Hard-on-hard total hip impingement causes extreme contact stress concentrations," *Clin Orthop Relat Res*, vol. 469, pp. 454-63, Feb 2011.
- [53] R. D. Cook and W. C. Young, *Advanced Mechanics of Materials*.
- [54] A. P. Sanders and R. M. Brannon, "Assessment of the applicability of the Hertzian contact theory to edge-loaded prosthetic hip bearings," *J Biomech*, vol. 44, pp. 2802-8, Nov 10 2011.
- [55] T. Belytschko, Xiao, S. P., "Coupling methods for continuum model with molecular model," *Int J Multiscale Computational Engineering*, vol. 1, pp. 115-126, 2003.